THERMAL CONDUCTIVITY AND CRITICAL CURRENT DENSITY OF VANADIUM BASED ALLOY SUPERCONDUCTORS

By

SABYASACHI PAUL

Enrolment No.: PHYS03201504009

Raja Ramanna Centre for Advanced Technology, Indore

A Thesis Submitted to the

Board of Studies in Physical Sciences

In partial fulfilment of requirements

for the degree of

DOCTOR OF PHILOSOPHY

of

HOMI BHABHA NATIONAL INSTITUTE

July 7, 2021

Homi Bhabha National Institute[1]

Recommendations of the Viva Voce Committee

As members of the Viva Voce Committee, we certify that we have read the dissertation prepared by Mr. Sabyasachi Paul entitled "Thermal conductivity and critical current density of vanadium based alloy superconductors" and recommend that it may be accepted as fulfilling the thesis requirement for the award of Degree of Doctor of Philosophy.

Chairperson– Prof. Aparna Chakrabarti	Aparna Chakrabarti	**Date: June 28, 2021**
Guide/Convener– Dr. M. K. Chattopadhyay		**Date: June 28, 2021**
Examiner - Prof. Tapan Kumar Nath	Tapan Kumar Nath	**Date: June 28, 2021**
Member 1- Prof. Tarun Kumar Sharma		**Date: June 28, 2021**
Member 2- Prof. Anil Kumar Sinha		**Date: June 28, 2021**
Member 3- Prof. Vidya. Sagar Tiwari		**Date: June 28, 2021**

Final approval and acceptance of this thesis is contingent upon the candidate's submission of the final copies of the thesis to HBNI.

I/We hereby certify that I/we have read this thesis prepared under my/our direction and recommend that it may be accepted as fulfilling the thesis requirement.

Date: June 28, 2021
Place: RRCAT, Indore

Signature

Guide: Dr. M. K. Chattopadhyay

[1] This page is to be included only for final submission after successful completion of viva voce.

STATEMENT BY AUTHOR

This dissertation has been submitted in partial fulfillment of requirements for an advanced degree at Homi Bhabha National Institute (HBNI) and is deposited in Library to be made available to borrowers under the rules of the HBNI.

Brief quotations from this dissertation are allowable without special permission, provided that accurate acknowledgement of the source is made. Request for permission for extended quotation from or reproduction of this manuscript in whole or in part may be granted by the Competent Authority of HBNI when in his or her judgement the proposed use of the material is in the interests of scholarship. In all other instances, however, permission must be obtained from the author.

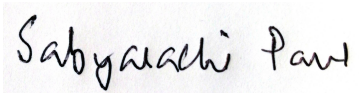

Sabyasachi Paul

DECLARATION

I, hereby declare that the investigation presented in the thesis has been carried out by me. The work is original and has not been submitted earlier as a whole or in part for a degree/ diploma at this or any other Institution/ University.

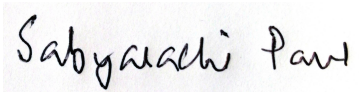

Sabyasachi Paul

List of Publications arising from the thesis

Journal Publications

Published

1. "Renormalization of electron-phonon coupling in the Mott-Ioffe-Regel limit due to point defects in the $V_{1-x}Ti_x$ alloy superconductors", **Sabyasachi Paul**, L. S. Sharath Chandra, and M. K. Chattopadhyay, J. Phys.: Condens. Matter, **2019** 31, 475801-475808.

2. "Structural and magnetic properties of the as-cast $V_{1-x}Zr_x$ alloy superconductors", L. S. Sharath Chandra, **Sabyasachi Paul**, Ashish Khandelwal, Vinay Kaushik, Archna Sagdeo, R. Venkatesh, Kranti Kumar, A. Banerjee, and M. K. Chattopadhyay, J. Appl. Phys., **2019**, 126, 183905-183914.

3. "Two channel heat conduction in the superconducting state of the as-cast $V_{1-x}Zr_x$ alloys", **Sabyasachi Paul**, L. S. Sharath Chandra, and M. K. Chattopadhyay, Physica B, **2020**, 577, 411763-411766.

4. "Grain refinement and enhancement of critical current density in the $V_{0.60}Ti_{0.40}$ alloy superconductors with Gd addition", **Sabyasachi Paul**, SK Ramjan, R. Venkatesh, L. S. Sharath Chandra, and M. K. Chattopadhyay, IEEE Trans. Appl. Supercond., **2021**, 31 (5), 8000104.

Communicated

1. "Coexisting superconductivity and ferromagnetism in the ($V_{0.60}Ti_{0.40}$)-Gd alloys", **Sabyasachi Paul**, SK. Ramjan, L. S. Sharath Chandra, and M. K. Chattopadhyay

Conferences

1. “Crossover from electronic to lattice thermal transport in Ti-V alloys”, **Sabyasachi Paul**, L. S. Sharath Chandra, and M. K. Chattopadhyay.

Annual meeting on physics of strongly correlated electron systems, April 02-04, 2018, IIT Mandi.

(Poster presented).

2. “Thermal conductivity of vanadium: Effect of disorder and inter-band scattering”, **Sabyasachi Paul**, L. S. Sharath Chandra, and M. K. Chattopadhyay.

63rd DAE-Solid State Physics Symposium, December 18-22, 2018, Guru Jambheswar University of Sci. & Tech., Hisar, Haryana, India.

AIP Conference Proceedings, **2019**, 2115, 030434-030437.

3. “Grain refinement and enhancement of critical current density in the $V_{0.60}Ti_{0.40}$ alloy superconductors with Gd addition”, **Sabyasachi Paul**, SK Ramjan, R. Venkatesh, L. S. Sharath Chandra, and M. K. Chattopadhyay

Applied Superconductivity Conference 2020, (Virtual conference) October 24 – November 07, 2020.

(Poster presented).

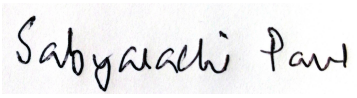

Sabyasachi Paul

Dedicated to all my well wishers

ACKNOWLEDGEMENTS

Looking back to august 2015, when I joined Ph.D, the completion of this work seemed to be a distant dream. The constant support of many people from different backgrounds, such as fellow students, researchers, technicians, administrative personal, security officers and many others led to the successful completion of this thesis in a presentable form. Naming each and every one of them is an impossible task, however I will always remember and remain grateful for their contribution to make my stay at RRCAT so wonderful. I would like to take this opportunity to express my gratitude towards them.

First of all, I would like to thank my thesis supervisor, Dr. M. K. Chattopadhyay for his guidance, constant support, encouragement and patience throughout the course. His enthusiasm to plan the measurements, analysis and interpretation of the experimental data and help in writing the manuscripts has been invaluable to the completion of the thesis. It has been a pleasant privilege and a memorable experience to work under him.

It has been a great pleasure to work with Dr. L. S. Sharath Chandra. I am sincerely grateful for his help in every step of the thesis. His eagerness to learn and understand new subjects helped me to have better understanding of physics. I have no words to describe his positive attitude towards everything and am very thankful to him for believing in my abilities even when I myself had doubt.

I sincerely thank my doctoral committee members: Dr. Aparna Chakrabarti, Dr. Rama Chari, Dr. A. K. Sinha, Dr. S. M. Gupta, Dr. T. Ganguli, Dr. T. K. Sharma, Dr. M. H. Modi, and Dr. V. S. Tiwari for their valuable time to evaluate my research progress. Their suggestions helped me to improve my research work.

I am thankful to Dr. K. K. Pant and other members of the FUS for maintaining a lively scientific environment. I am especially thankful to Mr. SK Ramjan for experimental support and scientific discussions. I thank Dr. Asish Khandelwal, Dr. M. A. Manekar, Dr. Shilpam Sharma, Shri Jagdish Chandra, Shri R. K. Meena, Shri Anil Chouhan and Shri Ashim Chakraborty for their help at various stages of this work.

I thank Dr. Archna Sagdeo for the XRD measurements, Dr. R. Kaul and Dr. P. Ganesh for optical metallography imaging, Dr. R. Venkatesh of UGC-DAE-CSR for the SEM and EDS measurements, Dr. Alok Banerjee and Mr. Kranti Kumar of UGC-DAE-CSR for the high field magnetization measurements, Dr. V. Ganesan and Mr. Vinay Kaushik of UGC-DAE-CSR for the high field resistivity and heat capacity measurements. A special thanks to the members of the Cryo-engineering and Cryo-module Development Section for providing the liquid helium and liquid nitrogen without which the present work would not have been possible. The Electrical Engineering Section is also thanked for providing uninterrupted power supply and for giving priority to our measurements. A special gratitude goes to HBNI-RRCAT for providing me the financial assistance. I am also thankful to Dr. Arup Banerjee, Dean Academic and Dr. C.P. Paul, Dean Student Affairs for their help in the academic and administrative fonts.

It is, of course not possible to thank every friend individually for their direct or indirect help, support and encouragement. I thank my batchmates, Azam, Dhanshree, Preeti, Sabina, Abyay, Avdhesh for making my life more comfortable here. I thank Durga, Shantanu, Kiranjot for being there whenever I needed them. I also got extensive help from many of my seniors and juniors, naming each of them will make this list really long. I would like to thank them all for their help.

Above all, I would like to thank my family members for their love, care and sacrifices without which it would have been impossible for me to come this far in life.

Contents

List of Figures

List of Tables

Chapter 8

Summary, conclusions and future outlook

8.1 Summary and Conclusions

In this thesis, we have presented experimental studies on the thermal conductivity κ and critical current density J_c of the $V_{1-x}Ti_x$ (x = 0, 0.1, 0.3, 0.5, 0.6 and 0.7), $V_{0.60-x}Ti_{0.40}Gd_x$ (x = 0, 0.005, 0.01 and 0.02) and $V_{1-x}Zr_x$ (x = 0, 0.05, 0.10, 0.20, 0.29, 0.33 and 0.40) alloys. The study was focused towards understanding how the presence of various disorders affect the κ and J_c of these alloys. The information on the structural phases present in the samples were obtained from XRD measurements. Optical metallography, SEM and EDS were performed to acquire metallurgical information to complement the XRD studies. The temperature dependence of electrical resistivity $\rho(T)$ and heat capacity $C(T)$ were also studied to analyze the $\kappa(T)$ results of these alloys in the normal and superconducting states. In the previous chapters, we have presented our studies in detail. Here we present an overall summary and conclusions of the work, along with the scope for future research in the relevant fields.

We started our work with the analysis of the $\kappa(T)$ of the $V_{1-x}Ti_x$ alloys. The $\rho(T)$ of these alloys reveal that the TCR of these alloys goes from positive for the $x = 0.6$ alloy to negative for $x = 0.7$ as the l_e goes below the inter-atomic distance (d_a), leading the system

to the Mott-Ioffe-Regal limit [101]. The signature of strong electron-phonon coupling in these alloys was observed in the temperature dependence of heat capacity. The $\kappa(T)$ of some of the $V_{1-x}Ti_x$ alloys was observed to be rising with decreasing temperature in the superconducting state. This indicates that the phonons carry the majority of the heat in the superconducting state of these alloys, whereas our analysis shows that the electrons carry the majority of the heat in the normal state. We have shown that this contrasting behaviour is related to the fact that the $l_e \sim d_a$, and the grain size is very large ($\sim$ few hundred μm to a few mm) in these alloys. It is important to note that this rise of the $\kappa_s(T)$ actually provides an opportunity to increase the J_c of these alloys by introducing additional defects. To proceed in this direction, we have added Gd in the $V_{0.60}Ti_{0.40}$ alloy.

The metallography results of the $V_{0.60-x}Ti_{0.40}Gd_x$ alloys show that the addition of Gd in the $V_{0.60}Ti_{0.40}$ alloy reduces the grain size, and that Gd precipitates in clusters along the grain boundaries. This reduction in the grain size increases the grain boundary density in the alloys, and thus the pinning of the flux lines at the grain boundaries, which in turn leads to the enhancement of J_c. The maximum J_c was observed for the $x = 0.01$ alloy. At 4 K, the J_c of the $x = 0.01$ alloy is enhanced by more than 20 times in comparison with the parent $V_{0.60}Ti_{0.40}$ alloy, in all fields up to the H_{irr}. Apart from the enhancement of J_c, a paramagnetic to ferromagnetic transition at 295 K and slight enhancement of the T_{sc} is also observed for the alloys containing Gd.

In order to understand the origin of the ferromagnetic transition at T_{mc} = 295 K and the enhancement of the T_{sc}, we have analyzed the $M(T)$, $\rho(T)$ and $\kappa(T)$ of the $V_{0.60-x}Ti_{0.40}Gd_x$ alloys. The Arrott plots (M^2 vs. H/M plots) [153] reveal the presence of a small spontaneous magnetization of 0.04 μ_B/f.u. and 0.13 μ_B/f.u. in the x = 0.01 and 0.02 alloys respectively at T = 10 K ($T > T_{sc}$). These alloys show a ferromagnetic transition at 295 K and are superconducting at low temperatures. Various superconducting properties like J_c, T_{sc} in fact are enhanced with the addition of Gd. This indicates that ferromagnetism and superconductivity coexist in these alloys. The increased disorder generated by the addition

of Gd leads to a significant suppression of the κ_l. On the other hand, the κ_e remains almost unaffected as the decrease of l_e due to increased scattering of electrons from disorder is compensated by the increase in l_e due to the suppression of itinerant spin fluctuations by the polarization of the conduction electrons by the magnetic moments of Gd. This leads to a crossover from phonon dominated heat conduction to electron dominated heat conduction in the superconducting state in the presence of an 8 T magnetic field. Moreover, as Gd is distributed only along the grain boundaries, the conduction electrons deep inside the grains only feel the average internal field generated by magnetic ordering along and around the grain boundaries below the T_{mc}. Thus the spin fluctuations are suppressed partially deep inside the grains resulting, in the enhancement of the T_{sc} in the Gd containing alloys.

Continuing our work on the J_c and κ of V-based alloy superconductors as an alternative to the Nb derived materials, we have also studied the structural, electrical and magnetic properties of the as-cast $V_{1-x}Zr_x$ alloys. The XRD analysis of the $V_{1-x}Zr_x$ revealed the presence of five different metallurgical phases, namely, a *bcc* β-V phase, two *fcc* ZrV_2 phases with slightly different composition (γ and γ'), a *hcp* α-Zr phase and a β-Zr phases. A lamellar microstructure is observed in the metallography images of the alloys with $x \geq 0.20$, which indicates that the alloys with $x \geq 0.20$ go through successive peritectic and eutectic type reactions. We have obtained an explanation for this multi-phase structure in terms of the rapid cooling of the melt. The percolation threshold for bulk superconductivity due to the ZrV_2 phase in the $V_{1-x}Zr_x$ alloys is observed to be less than $x = 0.10$. The J_c of the alloys with $x \geq 0.29$ is observed to be quite high and the J_c for the alloy with $x = 0.40$ is comparable with that of the modern Nb-Ti wires [179]. The huge number of grain boundaries formed during the eutectic like reaction are the dominant pinning centres for the flux lines in the low field regime. The nanometer sized β-Zr precipitates act as point defects and pin the flux lines for magnetic fields closer to the H_{irr}.

To understand how the presence of multiple superconducting and normal phases affect the $\kappa(T)$, we have studied the same in the normal and superconducting states of the $V_{1-x}Zr_x$

alloys. We inferred the presence of three superconducting phases with transition temperatures T_{sc1} = 5.2 K for β-V, T_{sc2} = 8.2 K for γ-ZrV_2 and T_{sc3} = 8.5 K for γ'-ZrV_2 respectively from three distinct jumps observed in the $C(T)$. The electronic thermal conductivity in the normal state κ_{en} is limited by the scattering of electrons from disorder and phonons. On the other hand, the phononic thermal conductivity in the normal state κ_{ln} is limited by scattering of phonons from the grain boundaries and point defects. Since, the κ_{ln} is not limited by the scattering of phonons from electrons, κ_l does not change when the alloy becomes superconducting. We have estimated the $\kappa_{es}(T)$ using the Bardeen-Rickayzen-Tewordt (BRT) theory [63, 68, 69] and found that to be lower than the experimental $\kappa_{es}(T)$. We have explained this anomaly by introducing a two-channel parallel conduction model in the superconducting state. The β-V phase is superconducting below 5.2 K. Hence, this phase remains normal in the temperature range 5.2 K to 8.5 K. Apart from the β-V, the α-Zr and β-Zr phases are also normal down to 2 K. This leads to the formation of a normal channel of heat conduction in parallel with the superconducting channel even when the bulk of the sample remains superconducting. This configuration makes these alloys more efficient in removing the heat than what is expected theoretically for a bulk superconductor and we have observed that below T_{sc3} (8.5 K) more than 80 % of heat is carried by the normal state conduction channel.

In the present thesis we have observed that while the J_c of the $V_{0.60}Ti_{0.40}$ alloys is enhanced significantly by the addition of Gd, it is still an order less than that of the commercial Nb-Ti alloys. However, since the grain size of the Gd-added $V_{0.60}Ti_{0.40}$ alloys is still in the tens of microns, further grain refinement may be possible in future to bring down the grain size to $\sim$ 100 nm so as to produce still higher J_c. In terms of the thermal conductivity, however, the $V_{1-x}Ti_x$ alloys seem to be better than the Nb-Ti alloys [75, 131, 182]. While the normal state thermal conductivity of the $V_{1-x}Ti_x$ alloys is similar to that of the Nb-Ti alloys, the superconducting state thermal conductivity of the $V_{1-x}Ti_x$ alloys is at least an order of magnitude higher than that of the Nb-Ti alloys. Addition of Gd in $V_{0.60}Ti_{0.40}$ does not suppress the thermal conductivity very significantly. However, it is important to keep

track of the thermal conductivity when further grain refinement is attempted in future. The thermal conductivity of the $V_{1-x}Zr_x$ alloys, on the other hand, are similar to or somewhat better than those of the $V_{1-x}Ti_x$ alloys in the normal state. The $V_{1-x}Zr_x$ are promising in terms of J_c as well. However, these alloys are very brittle when the amount of γ and γ'-ZrV_2 phases increase significantly, and circumventing this problem remains a challenging task.

8.2 Future outlook

Our studies on the V-based superconductors provide several directions for future research. The ρ_0 of some of the Nb-Ti alloys are also very high, similar to the $V_{1-x}Ti_x$ alloys [113]. Therefore, some of the Nb-Ti superconductors might also be near the Mott-Ioffe-Regel limit and it is important to study the thermal conductivity of these alloys. The J_c of the Nb-Ti alloys are reported to be enhanced by the introduction of dislocations [183]. Efforts may be made to further enhance the J_c of the RE-added $V_{1-x}Ti_x$ alloys in a similar manner. Moreover, due to the presence of the magnetic moments of Gd, the $V_{0.60-x}Ti_{0.40}Gd_x$ alloys show the coexistence of superconductivity and ferromagnetism in the alloys containing Gd. The survival of the robust superconductivity in this environment needs further investigation using magnetic force microscopy (MFM), muon-spin-resonance (μSR) spectroscopy etc. The addition of Nb with the ZrV_2 has been reported to enhance the mechanical property [176, 184, 185]. Therefore, research focusing on the enhancement of the mechanical properties of the $V_{1-x}Zr_x$ alloys by chemical substitution or addition of other elements may be taken up in future.

SUMMARY

In this present work, we study the thermal conductivity κ and critical current density J_c of the technologically promising $V_{1-x}Ti_x$, $V_{0.60-x}Ti_{0.40}Gd_x$ and $V_{1-x}Zr_x$ alloys as alternate to the Nb-derived superconductors and present the same as a thesis.

The $\kappa(T)$ of the $V_{1-x}Ti_x$ alloys starts to rise as the temperature decreases below the superconducting transition temperature T_{sc}. This shows that the phonons carry the majority of heat in the superconducting state of these alloys, whereas the electrons carry majority of the heat in the normal state. This contrasting behaviour is related to the facts that (i) very large number of point defects present in these alloys reduce the electron mean free path (l_e) down to the order of the inter atomic distances, and (ii) the grain size is very large ($\sim$ few hundred μm to few mm) in these alloys. This rise of the $\kappa_s(T)$ actually provides an opportunity to increase the J_c of these alloys by introducing additional defects. To proceed in this direction, we have added Gd in the $V_{0.60}Ti_{0.40}$ alloy.

We observe that the J_c of the $V_{0.60}Ti_{0.40}$ alloy is enhanced by more than 20 times at 4 K up to the irreversibility field H_{irr} when a small amount of Gd (1 at.%) is added. The H_{irr} also increases with the addition of Gd. This enhancement of J_c is due to the reduction in the grain size as a result of precipitation of Gd in clusters along the grain boundaries. The addition of Gd also introduces a transition similar to a paramagnetic to ferromagnetic transition at 295 K and slightly enhances the T_{sc} at the same time. In order to understand the origin of the paramagnetic to ferromagnetic transition at 295 K and the enhancement of the T_{sc} at the same time, we have analyzed the magnetization (M) and κ of the $V_{0.60-x}Ti_{0.40}Gd_x$ alloys in detail. Our analysis of the $M(T)$ and $M(H)$ confirmed that ferromagnetism and superconductivity coexist in these alloys. The addition of Gd in the $V_{0.60}Ti_{0.40}$ alloy suppresses the phononic part of the thermal conductivity κ_l significantly, whereas the electronic part κ_e hardly changes. This leads to a crossover from phonon dominated heat conduction to electron dominated heat conduction in the superconducting state in the presence of 8 T magnetic field. On the other hand, the partial suppression of spin fluctuations due to the polarization

of conduction electrons by the magnetic moments of Gd leads to the slight enhancement of the T_{sc} in the Gd containing alloys.

Continuing the work, we have then studied the structural, electrical and magnetic properties of the as-cast $V_{1-x}Zr_x$ alloys. The very high J_c of the $V_{1-x}Zr_x$ alloys is observed to be due to the presence of very large number of grain boundaries generated during the eutectic reaction. Our analysis shows that choosing a proper heat treatment and composition to drive these alloys to undergo eutectic reaction is important in enhancing their critical current density. The $V_{1-x}Zr_x$ alloys form with five different metallurgical phases. The β-V phase becomes superconducting below 5.2 K, whereas the α and β-Zr phases remain normal down to 2 K. This led to the formation of a normal channel of heat conduction in parallel to the superconducting channel even when the bulk of the sample remains superconducting. This configuration makes these alloys more efficient in removing the heat than what is expected theoretically for a bulk superconductor.

In the present thesis we have observed that the J_c of the $V_{0.60}Ti_{0.40}$ alloys is enhanced significantly by the addition of Gd. However, this enhanced J_c is still an order less than that of the commercial Nb-Ti alloys. In terms of the thermal conductivity, however, the $V_{1-x}Ti_x$ alloys seem to be better than the Nb-Ti alloys. While the normal state thermal conductivity of the $V_{1-x}Ti_x$ alloys is similar to that of the Nb-Ti alloys, the superconducting state thermal conductivity of the $V_{1-x}Ti_x$ alloys is at least an order of magnitude higher than that of the Nb-Ti alloys. Addition of Gd in $V_{0.60}Ti_{0.40}$ does not suppress the thermal conductivity very significantly. The thermal conductivity of the $V_{1-x}Zr_x$ alloys, on the other hand, are similar to or somewhat better than those of the $V_{1-x}Ti_x$ alloys in the normal state. The J_c of the $V_{1-x}Zr_x$ alloys are also much higher than the $V_{1-x}Ti_x$ alloys.

Chapter 1

Introduction

1.1 Preamble

Superconductors are now used in many fields, ranging from doing cutting edge research at the Large Hadron Collider to high resolution imaging of the human body in Magnetic Resonance Imaging machines and the usage is growing every day. However, even after 109 years of discovery, the superconductors used for high current high field applications are mostly Nb-based materials e.g. Nb-Ti, Nb_3Sn etc. This might lead to a scarcity of Nb. Apart from this, the Nb-derived materials are also not suitable for neutron irradiation environment (e.g. fusion reactor). This is because, Nb forms radioactive isotopes with very long half-lives when exposed to long period neutron irradiation [1, 2]. Thus, there is a need for materials alternate to Nb for technological applications of superconductors. The V based alloys and compounds are considered promising materials alternate to the commercially available Nb-based superconductors. The superconducting V-Ti alloys have relatively high upper critical field and good mechanical properties [3, 4, 5]. These alloys are also good for use in the neutron irradiation environment [2]. However, the critical current density (J_c) of the V-Ti alloys is about two orders of magnitude less than the commercial superconductors [6, 7].

On the other hand, the C15 laves phase ZrV_2 based superconductors have high upper critical field (H_{c2}) and high J_c [8, 9, 10, 11]. But these alloys are brittle at room temperature and

below and it is difficult to make wires and cables using them. Modern processing technologies like rapid heating and quenching (RHQ), powder-in-tube (PIT) and rod restack technologies have been extensively used for the fabrication of wires from various brittle superconductors like high-temperature ceramics, MgB_2, A15 materials etc. [12, 13, 14, 15, 16, 17, 18]. Hence there is a possibility that such advanced techniques may be useful for the ZrV_2 based superconductors as well. However, before using such techniques, one needs to have better understanding about various properties of these materials including the J_c and flux line pinning.

Apart from the J_c, the thermal conductivity (κ) of the material is another important property of a superconductor that one needs to consider for practical applications. Thermal conductivity gives information on the ability of a material to conduct heat. To avoid unwanted quench and ensure uninterrupted operation of a magnet, it is necessary to know the κ and its temperature dependence at the relevant temperature regime. Apart from that, the detailed analysis of κ gives idea about various scattering mechanisms present in the system, which in turn reflects upon the role of the defects present in the system [19]. The knowledge generated in this analysis may also help in enhancing the J_c of these alloys.

In this direction, we present a thesis on the detailed studies on the κ and J_c of some of the V-based alloy systems. In the first chapter, we start with a brief discussion on the phenomenon of superconductivity and the J_c of superconductors. This is followed by a discussion on the basics of thermal conductivity in the normal and superconducting states. At the end of this chapter, we present the plan of the thesis.

1.2 Basics of superconductivity and flux pinning in superconductors

1.2.1 Zero resistance and Meissner effect

There are two characteristic properties that separate the superconductors from other materials. One is the zero resistance, which allows them to carry dissipationless current and the other is the perfect diamagnetism. When cooled to sufficiently low temperatures, the resistivity of certain materials abruptly drops to zero. The temperature at which the resistivity becomes zero is known as the critical temperature (T_c). This was first observed for Hg at the Leiden laboratory when H. Kamerlingh Onnes found the resistance to fall below 10^{-5} Ω (limit for the measurement at that time) around 4.2 K [20]. Since then superconductivity has been observed in more than 30 elements and thousands of other alloys and compounds under suitable conditions.

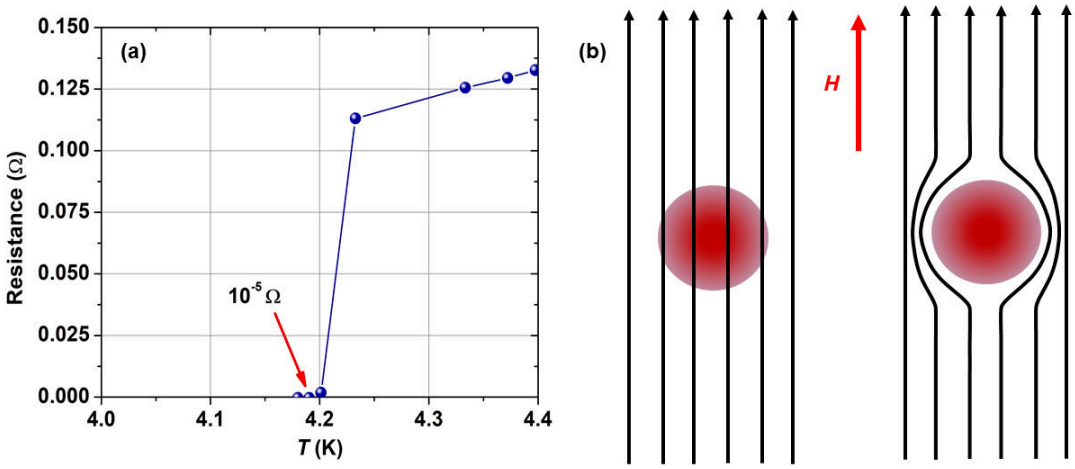

FIGURE 1.1: Temperature dependence of resistance of Hg as measured by Kamerlingh Onnes. The drop of resistance near 4.2 K marks the onset of superconductivity (figure regenerated using the data from Ref. [21]). (b) Schematic diagram of the Meissner effect. The magnetic flux is expelled from the interior of the superconductor when it is cooled below the critical temperature (T_c).

Twenty-two years after the discovery of superconductivity, Meissner and Oschenfeld

found that superconductors expel the magnetic flux from their inside irrespective of their magnetic history. This is known as the Meissner-Oschenfeld effect [22]. To expel the magnetic flux a diamagnetic screening current needs to flow at the surface of the material. This screening current cannot be confined only at the surface as that will make the current density infinite. F. London and H. London gave an explanation of the Meissner effect on the basis of the two-fluid model of Gorter and Casimir [23]. According to this model the free electron density is the sum of the superconducting electron density and normal electron density. Using this model, F. and H. London argued that the magnetic field inside a superconductor does not become zero instantly and falls over a characteristic length scale λ_L, now known as the London penetration depth.

1.2.2 Ginzburg-Landau theory of superconductors

The first phenomenological theory of superconductivity was given by Ginzburg and Landau. This theory is based on Landau's theory of second order phase transition, which considers the superconducting state to be more ordered than the normal state [24, 25, 26]. They considered the effective wavefunctions of the electrons $\psi(r)$ as the order parameter that is non-zero for $T < T_c$ and is zero for $T \geq T_c$. The Ginzburg-Landau (GL) theory does not give the microscopic mechanism of superconductivity but examines the macroscopic properties using thermodynamic arguments. In the Landau theory of second-order phase transition, the free energy is expanded in powers of the order parameter – which is small near the T_c [24]. Hence, it will be valid only at temperatures close to the T_c, i.e, $(T_c - T) \ll T_c$.

Ginzburg and Landau took the effective wavefunction of the superconducting electrons $\psi(r)$ as the order parameter such that its normalization gives the number density of the Cooper pairs (n_s) as [24],

$$|\psi(r)|^2 = \frac{n_s}{2}. \tag{1.1}$$

For a superconductor in a uniform field, the Gibbs free energy (g_s) can be expanded in terms of the order parameter. For $(T_c - T) \ll T_c$,

$$g_s = g_n + \int dV \left[\alpha|\psi|^2 + \beta|\psi|^4 + \frac{1}{4m}\left| -i\hbar\nabla\psi - \frac{2e}{c}\mathbf{A}\psi \right|^2 + \frac{H.H}{8\pi} - \frac{H.H_0}{4\pi} \right], \quad (1.2)$$

here H_0 is the applied magnetic field and $\mathbf{A}$ is the magnetic vector potential. In equation 1.2, g_n is the free energy in the normal state. The last two terms give the magnetic field contribution to the free energy, where H is the exact microscopic field at any point of the superconductor. The term $\alpha|\psi|^2 + \beta|\psi|^4$ is a typical Landau term and the term $\frac{1}{4m}\left|-i\hbar\nabla\psi - \frac{2e}{c}\mathbf{A}\psi\right|^2$ gives the kinetic energy of a charged particle of charge $2e$ and mass $2m$ moving in a magnetic field with vector potential $\mathbf{A}$. Minimising equation 1.2 for $\psi^*(r)$ and $\mathbf{A}$ we find,

$$\alpha\psi + \beta\psi|\psi|^2 + \frac{1}{4m}\left| -i\hbar\nabla - \frac{2e}{c}\mathbf{A} \right|^2 \psi = 0 \quad (1.3)$$

and

$$j_s = -\frac{i\hbar e}{2m}(\psi^*\nabla\psi - \psi\nabla\psi^*) - \frac{2e^2}{mc}|\psi|^2\mathbf{A}. \quad (1.4)$$

Equations 1.3 and 1.4 are known as first and second GL equations respectively [24].

1.2.3 Characteristic length scales of the superconducting state and classification of superconductors

The superconducting state of a material can be described by two length scales i.e. the coherence length ξ and the London penetration depth λ_L. The ξ gives the distance over which the superconducting order parameter varies i.e., the distance over which the superconducting correlations grows. The λ_L gives the distance over which the magnetic field inside a superconductor drops from its value outside.

From the first and second GL equations we obtain the expressions for ξ and λ_L respectively as [24],

$$\xi = \sqrt{\frac{\hbar^2}{4m|\alpha|}} \tag{1.5}$$

and

$$\lambda_L = \sqrt{\frac{mc^2}{8\pi e^2}\left|\frac{\beta}{\alpha}\right|}. \tag{1.6}$$

The ratio of λ_L and ξ is known as the GL parameter ($\kappa_{GL} = \frac{\lambda_L}{\xi}$) and is independent of temperature within the GL theory. The superconductors are classified in two categories on the basis of the value of κ_{GL}.

For the superconductors with $\kappa_{GL} < \frac{1}{\sqrt{2}}$, the magnetic flux is expelled completely up to an applied magnetic field H_c, known as the critical field. These superconductors are known as type-I superconductors, and they become normal when the applied magnetic field value exceeds H_c. The temperature dependence of H_c follows the relation, $H_c(T) = H_c(0)(1 - (T/T_c)^2)$ [24].

For $\kappa_{GL} > \frac{1}{\sqrt{2}}$, the superconductors expel the magnetic flux completely up to an applied magnetic field H_{c1}. When the applied magnetic field exceeds H_{c1}, these superconductors expel the magnetic flux partially up to a higher field H_{c2}. These superconductors are known as the type-II superconductors. H_{c1} and H_{c2} are known as the lower and upper critical fields respectively. In the field range between H_{c1} and H_{c2}, the superconductor is threaded by vortices of quantized magnetic flux and is said to be in the mixed state. The field vs. temperature phase diagram of type-I and type-II superconductors are respectively shown in figures 1.2 (a) and 1.2 (b) respectively.

For a type-I superconductor, the magnetization decreases linearly with the increase in the magnetic field up to H_c and attains the normal state value for $H > H_c$. In type-II superconductors, the magnetization decreases up to H_{c1} due to complete expulsion of flux and starts to increase for applied fields greater than H_{c1} and obtain the normal state value at $H = H_{c2}$. The field dependence of magnetization is shown in figures 1.2 (c) and (d) for

type-I and for type-II superconductors.

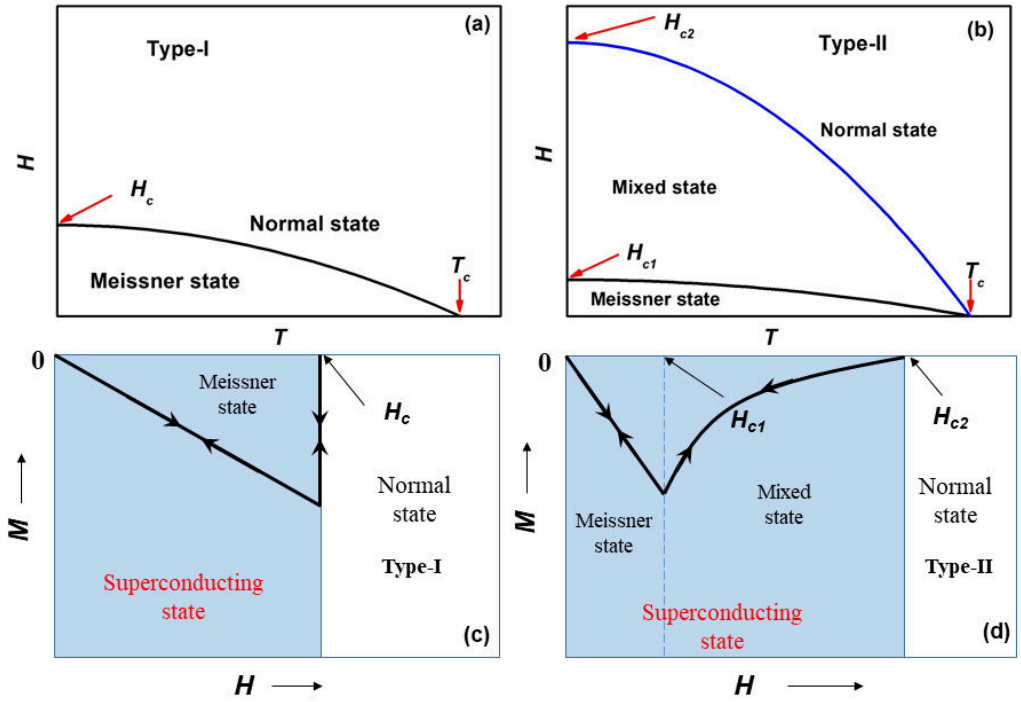

FIGURE 1.2: (Schematic) Field (H) vs. temperature (T) phase diagram for (a) type-I and (b) type-II superconductors respectively. Field dependence of magnetization ($M(H)$) for ideal reversible (c) type-I and (d) type-II superconductors.

1.2.4 Field of an isolated vortex and flux line lattice

For a type-II superconductor, the surface energy of the interface between the normal and superconducting region is negative. This makes it energetically favourable for these materials to separate out into normal and superconducting regions. The normal regions form in such a way that the boundaries lie parallel to the applied magnetic field. The boundary between normal and superconducting region is not sharp but spread over the coherence length ξ. Thus, the superconducting electron density decreases over a distance ξ and goes to zero at the centre of the core. On the other hand, the magnetic field penetrates the superconducting region over a length λ_L. Thus, the magnetic field in the core will be generated by the vortex

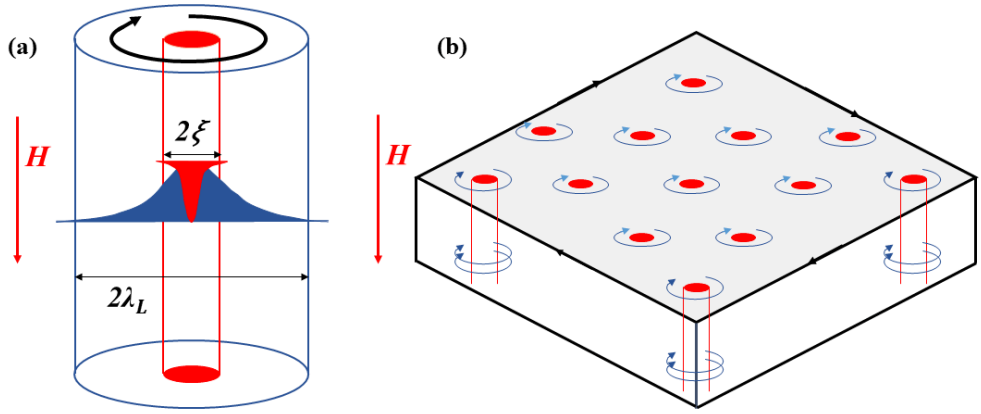

FIGURE 1.3: (Schematic) (a) The variation of the superconducting order parameter and the magnetic field profile of an isolated field vortex. (b) Schematic of a superconductor in the mixed state. The normal cores arrange themselves in a regular hexagonal (triangular) arrangement known as the Abrikosov lattice [24].

of a persistent current circulating over a distance over λ_L [27]. The schematic of the variation of order parameter and magnetic field profile of an isolated vortex is shown in figure 1.3 (a).

In the mixed state of an ideal superconductor, the bulk of the superconductor is diamagnetic. A screening current circulates around the perimeter of the sample and opposes the applied magnetic field. On the other hand, a vortex current circulates around the normal cores in the direction opposite to that of the diamagnetic screening current. The vortex current of one core repels that of adjacent cores and thus, the normal cores cannot lie randomly in the superconductor. Abrikosov showed that the normal cores arrange themselves in a triangular or hexagonal periodic array. This arrangement is known as the fluxon lattice or Abrikosov lattice [27] (shown in figure 1.3 (b)).

1.2.5 Pinning of flux lines and magnetic irreversibility of type-II superconductors

For an ideal superconductor that does not contain any disorder, the magnetization is reversible with respect to increasing and decreasing fields. But in real superconductors, there

are many defects such as voids, impurities, dislocations, grain boundaries, secondary phase precipitates etc. The free energy at the defect sites is different from that in the superconducting region. The gradient in the free energy between the normal and superconducting regions gives rise to the pinning force and the normal cores can get pinned at the defect sites if the size of the defects are of the order of ξ [28]. Hence these imperfections in the crystal are known as pinning centres. Pinning of the flux lines at these defect sites give rise to the irreversibility of magnetization for a type-II superconductor. Figure 1.4 shows a schematic for reversible and irreversible type-II superconductor.

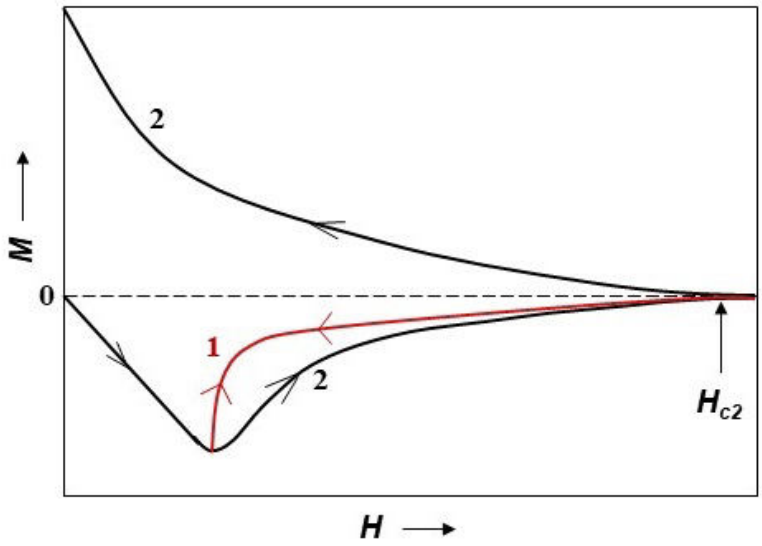

FIGURE 1.4: Schematic for the field dependence of magnetization (M(H)) for a type-II superconductor. Curve 1 shows the M(H) for an ideal type-II superconductor free from defects. Curve 2 represent the M(H) for a superconductor with various defects present.

1.2.6 Critical current density of the superconductors

The J_c of a superconductor is one of the most important properties from the application point of view. For an applied magnetic field less than H_{c1}, a type-II superconductor expels the magnetic flux completely. As the applied magnetic field is increased above H_{c1}, normal cores are formed and the superconductor goes to the mixed state. If a transport current is

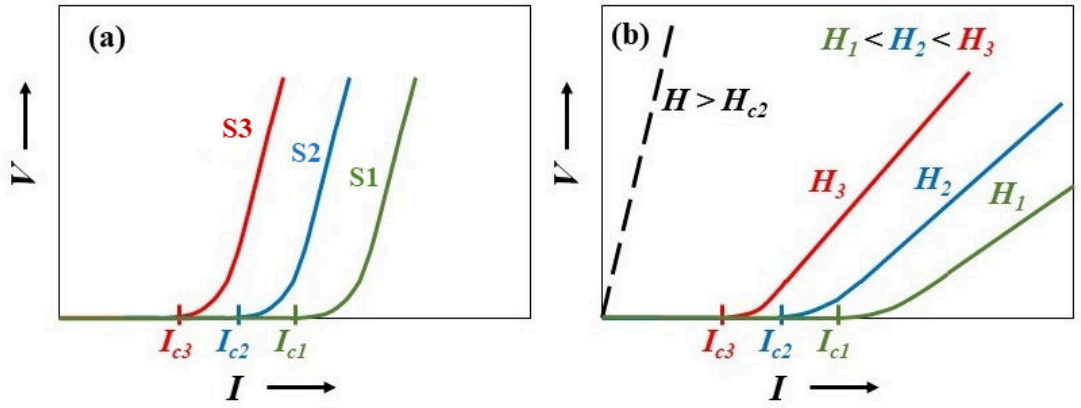

FIGURE 1.5: (Schematic) (a) Voltage (V) vs. current (I) characteristics of three different superconductors having different amount of defects measured in the same applied magnetic field. Sample S1 has the maximum defects and sample S3 has the least defects. The critical current density increases with increasing amount of defects. (b) The $V - I$ characteristics of a superconductor in the presence of different applied magnetic fields. The order of the magnitude of the applied magnetic field is $H_1 < H_2 < H_3 < H_{c2} < H$.

passed through a superconductor in the mixed state, the normal cores will feel a Lorentz force in a direction perpendicular to both the applied magnetic field and the transport current. If the material is free from defects, very small amount of current will generate enough Lorentz force to set the cores into motion causing dissipation of energy. In a real system, the defects work as pinning centres and hinder the motion of the flux lines. The transport current density required to overcome the pinning force is known as the critical current density J_c. The relation between the critical current (I_c) and J_c is, $I_c = J_c \times A$, where A is the cross-sectional area perpendicular to the direction of the current. The J_c can be estimated from the voltage-current curves of a superconductor. The pinning force depends on the nature of the defects present in the system and the Lorentz force depends on the applied magnetic field. Thus, the J_c will depend on both the applied field and the amount of the disorder present in the system. Figure 1.5 shows the characteristic of the current-voltage graphs of a superconductor. The J_c is obtained from the value of the transport current, where a finite voltage drop across the sample is observed [27].

1.2.7 Dew-Hughes' theory of flux pinning in type-II superconductors

The irreversibility in the field dependence of magnetization ($M(H)$) occurs due to the presence of defects in the superconductors. The amount of current that a superconductor can carry without giving rise to any resistance also depends on the defects present in the system. Thus, it is possible to find a relation between the J_c and the difference in magnetization between increasing and decreasing magnetic fields. This problem was solved by the model developed by C. P. Bean, which assumes that the supercurrent flows in accordance with the Maxwell's equation $\nabla \times H = J_c$ (H is the internal field) [29, 30]. The critical state is obtained when the Lorentz force just balances the pinning force, i.e., $\left|\vec{F_P}(H)\right| = \left|\vec{J_c}(H) \times \vec{H}\right|$ [31, 32].

TABLE 1.1: Functional form of $f_P(h)$ corresponding to different kinds of pinning centres according to Dew Hughes' theory.

Curve no. in figure 1.6	Type of pinning	Geometry	Functional form	Position of the peak
Magnetic interaction				
1	Normal	Volume	$h^{0.5}(1-h)$	0.33
2	$\Delta\kappa_{GL}$	Volume	$h^{0.5}(1-2h)$	0.17, 1
Core interaction				
3	Normal	Volume	$(1-h)^2$	-
4	$\Delta\kappa_{GL}$	Volume	$h(1-h)$	0.5
5	Normal	Surface	$h^{0.5}(1-h^2)$	0.2
6	$\Delta\kappa_{GL}$	Surface	$h^{1.5}(1-h)$	0.6
7	Normal	Point	$h(1-h)^2$	0.33
8	$\Delta\kappa_{GL}$	Point	$h^2(1-h)$	0.67

The $F_P(H)$ should be zero at $H = 0$, pass through at least one maximum as H is increased and return to zero at the irreversibility field $H = H_{irr}$. It was found that if the normalized

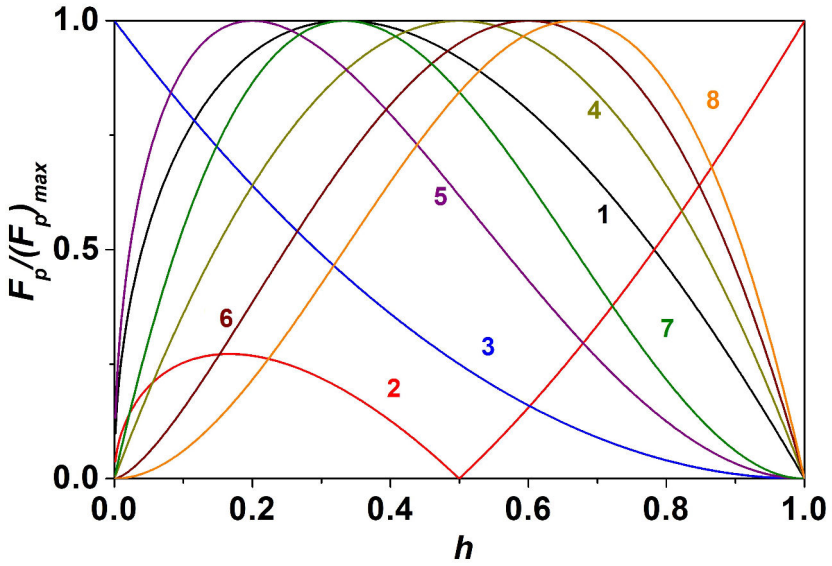

FIGURE 1.6: $f_P(h)$ for different pinning mechanisms.

flux pinning force density ($f_P = \frac{F_P}{(F_P)_{max}}$) is plotted as a function of the reduced field ($h = H/H_{c2}$), then it follows a functional form, $f_P \propto h^p(1-h)^q$, where p and q are two constants, whose value depend on the details of the pinning mechanisms. Dew-Hughes performed a detailed analysis and obtained the functional form of f_P and the position of the maximum in f_P for different types of pinning mechanisms. According to the Dew-Hughes' theory, if the size of the defects and the spacing between them is more than the penetration depth of the material, then the magnetic field will be in equilibrium everywhere in the superconductor, but will have different values in the pinning centres as compared to that in the matrix. The pinning originating from this type of interaction is known as magnetic interaction. If the size of the defects or the separation between them is less than the penetration depth, then the magnetic field cannot achieve such equilibrium and the pinning appearing from this type of interaction is known as the core interaction. Again, the pinning centres can be both normal and superconducting. If the pinning centres are normal inclusions, they give rise to the so called 'normal pinning'. If the pinning centres are superconducting, the pinning force may originate from a small difference in the critical temperature or GL parameter. This type of pinning is known as the '$\Delta\kappa_{GL}$' pinning. table 1.1 lists the functional form of f_P and

position of maximum for different type of pinning mechanisms according to Dew-Hughes' theory [31], and figure 1.6 shows the curves corresponding to these functional forms.

1.3 Critical current density of different superconducting systems

From the viewpoint of high field-high current applications, the most important property of a superconductor is the maximum current it can carry without giving rise to any dissipation, i.e., the critical current density J_c. The J_c of commercial multifilamentary Nb-Ti is reported to be $\sim 2.5 \times 10^9$ A/m^2 (4.2 K and 5 T) [33, 34, 35, 36, 37, 38, 39] and that for commercial Nb_3Sn is 4.7×10^9 A/m^2 (4.2 K and 9 T) [37, 40, 41]. We have earlier mentioned that the potential alternate to the Nb-based superconductors may be clubbed into two broad categories. First, the superconductors exhibiting very high J_c and upper critical field (H_{c2}) but brittle in nature. The A15 compounds, high-temperature superconductors, Chevrel phase superconductors, Laves phase C15 superconductors, MgB_2 etc. fall in this category. Second, the superconductors having ductility and malleability but having only moderate J_c in comparison with the NbTi and Nb_3Sn superconductors. The transition metal-based V-Ti, Mo-Re etc. fall under this category.

Among the brittle superconductors with very high J_c and H_{c2}, the A15 Nb_3Al, Chevrel phase $PbMo_6S_8$, some of the high-T_c cuprates, and MgB_2 are considered potential superconductors for future applications [5]. Although such brittle superconductors are now used to fabricate wires using advanced processing technologies like PIT, rod restack, RHQ etc., the J_c strongly depends on the final composition [11, 12, 13, 42, 43]. Moreover, the J_c for a coil is found to be lower in comparison with that of the bulk for all these materials [18, 44].

With an $H_{c2}(0)$ of 35 T [45, 46] ($\sim$ 10 T higher than Nb_3Sn), Nb_3Al is considered to be one of the best alternative for the Nb_3Sn superconductor. Low temperature processed Nb_3Al multifilamentary wires have $J_c \sim 7 \times 10^7$ A/m^2 (4.2 K and 10 T) [47], which is slightly lower

than the commercial Nb_3Sn wires but the strain tolerance in Nb_3Al is much better than the Nb_3Sn superconductor [47, 48, 49]. In a recent study, Lin *et al.* has showed that the J_c of Nb_3Al gets enhanced by hot pressure sintering due to increased grain connectivity [50].

The $PbMo_6S_8$ Chevrel phase superconductors have an $H_{c2} \sim 55$ T at 4.2 K [51]. This makes $PbMo_6S_8$ a potential material for applications in much higher fields than what is achievable with the Nb_3Sn superconductors. $PbMo_6S_8$ has a $J_c \sim 5 \times 10^8$ A/m^2 (4.2 K and 15 T) [51, 52]. The MgB_2 is another superconductor that has a very high H_{c2} [53]. The J_c of the MgB_2 strands with 2% carbon made via internal magnetism diffusion has $J_c \sim 4 \times 10^8$ A/m^2 (4.2 K and 12 T) [54, 55].

The high-T_c superconductors possess very high H_{c2} but the J_c of these materials is quite low in the presence of magnetic fields [56, 57]. This is due to the weak links between the grains. Another problem with the high-T_c materials is that there exists a huge anisotropy in the J_c. For practical purpose, the high-T_c superconductors are fabricated in the form of tapes. With modern processing technologies the J_c of the order of 10^9 A/m^2 (20 K and $H = 0$) has been reported for Ag-sheathed Bi-2223 [56, 58]. However, one should note that, Ag possesses the same problem as Nb when exposed to long term neutron irradiation [5].

The C15 Laves phase superconductors have J_c and H_{c2} comparable to the Nb-based superconductors. In fact, composite tapes of $V/Hf_{0.4}Zr_{0.6}$ have $J_c \sim 10^7$ A/m^2 (4.2 K and 15 T) [8, 9], which is higher than Nb_3Sn at this temperature and field. In a recent report Wu *et al.* has shown that the H_{c2} of the HfV_2 increases with Nb doping [59].

Vetrano *et al.* first reported the J_c of the $V_{0.2}Ti_{0.8}$ alloy [60]. He studied the effects of heat treatment on the J_c of this alloy. The heat treatment precipitates the secondary α and ω phases that work as pinning centres. Thus, the critical current density increases with heat treatment. The maximum value of the J_c achieved for this alloy is $\sim 3 \times 10^8$ A/m^2 [60]. Tai *et al.* has shown that heat treatment causes the α-Ti deposition in the sample and that leads to the enhancement of the J_c in these alloys [5]. They found that the heat treatment

causes the enhancement of J_c from 7×10^7 A/m^2 (4.2 K and 6.5 T) to 1.7×10^8 A/m^2 (4.2 K and 6.5 T) in a V-45 at % Ti alloys [5]. Following up the work of Tai *et al.*, Matin *et al.* in our laboratory studied in detail the J_c and flux pinning properties of the as-cast and annealed V-Ti alloys and correlated them with the metallurgical phases present in the alloys [6, 7]. The maximum J_c of 6×10^8 A/m^2 (2 K and $H = 0$) was observed for the as cast $V_{0.3}Ti_{0.7}$ alloy [7].

1.4 Thermal conductivity

The study of thermal conductivity (κ) gives idea about how a material carries heat and what are the factors that affect the same. Electrons and lattice waves (phonons) are the two primary carriers of heat in any material. Other excitations such as magnons, spin waves etc. can also carry some amount of heat. Thus, the total thermal conductivity of a material may be expressed as [19],

$$\kappa = \sum_{\alpha} \kappa_{\alpha} \tag{1.7}$$

where α stand for a specific type of excitation. The magnitude and nature of the temperature dependence of κ of a material can vary significantly, depending upon the amount of disorder present, anharmonicity of the crystal, carrier type and concentration, types of interactions present and their relative strength etc. Figure 1.7 shows the thermal conductivity of two Ag samples with different amounts of disorder. The thermal conductivity of Ag with less disorder increases with increasing temperature, goes through a peak and becomes almost constant at higher temperature. The Ag sample with more disorder shows a monotonic rise with increasing temperature. Historically, the lattice defects have been investigated using the thermal conductivity measurements as a tool [19]. In the following sub-sections, we discuss on the basics of the thermal conductivity of materials in both the normal and superconducting states.

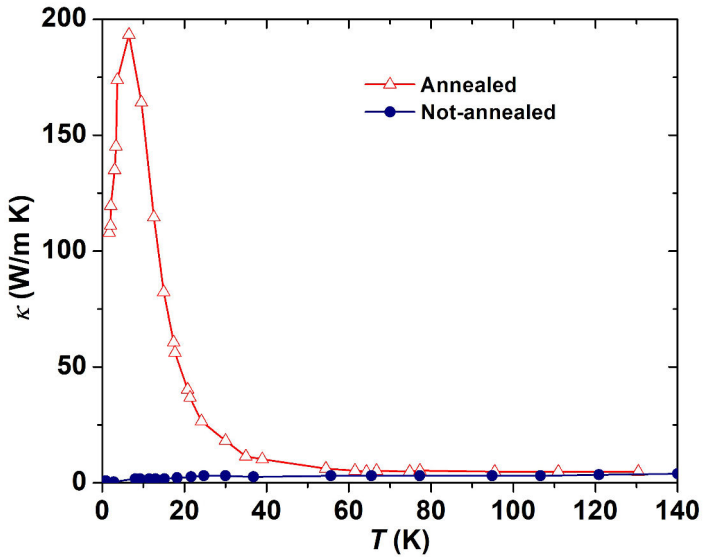

FIGURE 1.7: Thermal conductivity of two Ag samples with different amounts of disorder. Figure reproduced using the data reported in ref. [61].

1.4.1 Kinetic theory

The thermal conductivity of a material is defined as,

$$\kappa = -\frac{\mathbf{Q}}{\nabla T}, \tag{1.8}$$

where **Q** is the amount of the heat flowing through the perpendicular surfaces of a unit cube and ∇T is the temperature difference between the surfaces. Using kinetic theory, one can find [20],

$$\kappa = \frac{1}{3} C v l, \tag{1.9}$$

where C is the specific heat, v is the velocity and l is the mean free path of the excitation concerned. Thus, the total thermal conductivity can be obtained as,

$$\kappa = \sum_{\alpha} \frac{1}{3} C_{\alpha} v_{\alpha} l_{\alpha}. \tag{1.10}$$

Although equation 1.10 has been estimated very crudely, it gives fairly accurate idea about the value of thermal conductivity of materials.

1.5 Thermal conductivity in the normal state

Electrons and (or) phonons are the carriers of heat in a solid. So, the total thermal conductivity is given by,

$$\kappa_n = \kappa_{en} + \kappa_{ln}, \tag{1.11}$$

where κ_{en} and κ_{ln} are respectively the electronic and phononic thermal conductivities in the normal state.

In pure metals, the majority of heat (if not all) is carried by the electrons almost over the whole temperature range up to the melting point. In metallic alloys, although the electronic thermal conductivity dominates at low temperature ($T \ll \theta_D$), phonons carry substantial amount of heat at higher temperature. For semiconductors, apart from electrons there are positively charged holes to contribute to the heat conduction. Due to the presence of the band gap, in some semiconductors the lattice thermal conductivity dominates the heat conduction (depending on the energy gap) over a wide temperature range. Insulators do not have conduction electrons. Phonons are the major carriers of heat in these materials. Here we will confine our discussion to the metals and metallic alloys. Thus, in our analysis, we shall consider both the electronic and phononic thermal conduction.

1.5.1 Electronic thermal conductivity in the normal state

Conduction electrons are scattered by the lattice defects, phonons and other electrons while carrying heat. As the same electrons are scattered from multiple lattice disorders, phonons or other electrons, the electronic thermal resistivity is considered to be additive in nature. The relaxation time for electron-electron scattering is about 10^4 times longer in comparison with the electron-defect or electron-phonon scattering relaxation times [62]. This makes the

electron-electron scattering to be hardly effective except for highly pure metals at very low temperatures. Thus, this term is ignored for practical purpose. Hence, the electronic thermal conductivity is given by,

$$\kappa_{en} = \frac{1}{w_{en}} = \frac{1}{w_{ei,n} + w_{el,n}}, \tag{1.12}$$

here w_{en} is the total electronic thermal resistivity in the normal state, $w_{ei,n}$ is the normal state electronic thermal resistivity limited by the scattering of electrons by defects and $w_{el,n}$ is the electronic thermal resistivity limited by scattering of electrons from phonons. The electronic thermal conductivity limited by scattering electrons from defects ($\kappa_{ei,n}$) can be estimated using equation 1.9. The electronic heat capacity is given by, γT, where γ is the Sommerfeld coefficient. The defects in the metals being static, the mean free path is constant. Again, the electrons in a conduction band move with the Fermi velocity, which is independent of temperature. Thus, the $\kappa_{ei,n}$ becomes,

$$\kappa_{ei,n} = \frac{1}{3}\gamma T v_e l_e = \frac{T}{A_n} = \frac{1}{w_{ei,n}}, \tag{1.13}$$

here A_n is the coefficient of electronic thermal resistivity due to scattering of electrons from disorders ($w_{ei,n}$). Thus, the $w_{ei,n}$ is inversely proportional to temperature. One way to estimate the $\kappa_{ei,n}$ is to use Wiedemann-Franz (WF) law, which says that the ratio of thermal to electrical conductivity (σ) is proportional to temperature, i.e.,

$$\frac{\kappa}{\sigma} = L_0 T, \tag{1.14}$$

$L_0 = \frac{\pi^2 k_B^2}{3e^2}$ is the Lorentz number, where k_B is the Boltzmann constant and e is the electronic charge. Although the WF law gives a very crude way of estimation of the electronic thermal conductivity, using it at low temperatures one can get an idea about the share of heat conducted by the electrons in a metallic system as compared to that by the phonons.

In most of the materials, scattering of electrons from the phonons play a major role in determining the electronic thermal conductivity over a wide range of temperatures. The

thermal resistance appearing from this interaction is known as ideal resistance (w_{el}) and is given by [19],

$$w_{el} = \frac{B_n}{T}\left(\frac{T}{\theta_D}\right)^5 J_5\left(\frac{\theta_D}{T}\right)\left\{1+\frac{3}{\pi^2}\left(\frac{k_F}{q_D}\right)^2\left(\frac{\theta_D}{T}\right)^2-\frac{1}{2\pi^2}\frac{J_7\left(\frac{\theta_D}{T}\right)}{J_5\left(\frac{\theta_D}{T}\right)}\right\}, \tag{1.15}$$

where $J_n\left(\frac{\theta_D}{T}\right)$ is given by $\int_0^{\theta_D/T}\frac{x^n e^x}{(e^x-1)^2}dx$. Here, θ_D is the Debye temperature, k_F is the electron wave number at the Fermi surface, q_D is the phonon wave number B_n is the coefficient of electronic thermal resistivity due to scattering of electrons from phonons.

At high temperatures ($T \geq \theta_D$), equation 1.15 becomes [19],

$$w_{el} = \frac{B_n}{4}\frac{1}{l_0 T}\frac{T}{\theta_D}, \tag{1.16}$$

and at low temperatures ($T \ll \theta_D$), equation 1.15 becomes [19],

$$w_{el} = 37.8\frac{B_n}{L_0\theta_D}\left(\frac{k_F}{q_D}\right)^2\left(\frac{T}{\theta_D}\right)^2. \tag{1.17}$$

Thus, the w_{el} increases linearly with increasing temperature at high temperatures and is proportional to the square of temperature at low temperatures.

1.5.2 Phonon thermal conductivity in the normal state

Phonons carry majority of the heat in non-metallic systems. Similar to electrons, the phonons get scattered by defects, electrons and other phonons. But unlike electrons, the phonons get scattered differently from various defects and the total phonon resistivity (w_l, n) is given by,

$$w_{l,n} = w_{lb,n} + w_{ld,n} + w_{lp,n} + w_{le,n} + w_{ll,n}, \tag{1.18}$$

where $w_{lb,n}$, $w_{ld,n}$, $w_{lp,n}$, $w_{le,n}$ and $w_{ll,n}$ are respectively the phonon thermal resistivity limited by scattering of phonons from grain boundaries, dislocations, point defects, electrons

and other phonons. There are two types of phonon-phonon scattering that takes places in a lattice – the normal scattering and the Umklapp scattering. The normal phonon scattering does not give rise to any resistance to heat conduction. The resistance to the heat conduction occurs only from Umklapp scattering. To estimate the phonon thermal conductivity, one needs to evaluate different phonon relaxation times, which is difficult to estimate for a real solid. Using the Debye approximation, the lattice thermal conductivity may be calculated as [19],

$$\kappa_{l,n} = \frac{k_B}{2\pi^2 v_l}\left(\frac{k_B}{\hbar}\right)^3 T^3 \int_0^{\theta_D/T} dx\tau(x)\frac{x^n e^x}{(e^x-1)^2}, \tag{1.19}$$

here v_l is the average phonon velocity, $\hbar$ is the reduced Planck's constant, τ is the relaxation time of the phonons and $x = \frac{\hbar\omega}{k_B T}$ is the reduced phonon frequency. In the presence of multiple scattering mechanisms, one can approximate the relaxation time such that,

$$\tau^{-1} = \tau_{lb}^{-1} + \tau_{ld}^{-1} + \tau_{lp}^{-1} + \tau_{le}^{-1} + \tau_{ll}^{-1}, \tag{1.20}$$

τ_{lb}^{-1}, τ_{ld}^{-1}, τ_{lp}^{-1}, τ_{le}^{-1} and τ_{ll}^{-1} are respectively the relaxation time of phonons scattered by grain boundaries, dislocations, point defects, electrons and other phonons.

Substituting the relaxation times for different scattering mechanisms we obtain,

$$\kappa_{l,n} = \int_0^{\theta_D/T} dx \frac{x^n e^x}{(e^x-1)^2} \frac{1}{\frac{N_n}{M}\frac{1}{T^3} + \frac{L_n}{M}\frac{x}{T^2} + \frac{E_n}{M}\frac{x}{T^2} + \frac{P_n}{M}x^4 T + \frac{U}{M}T^2 \exp(-\frac{\theta_D}{3T})}, \tag{1.21}$$

where $M = \frac{k_B^4}{2\pi^2 v_l \hbar^3}$ and N_n, L_n, E_n, P_n, U represent the strength of scattering of phonons from boundary, dislocations, point defects, electron and other phonons respectively in the normal state [19].

1.6 Thermal conductivity in the superconducting state

The thermal conductivity of a material has non-zero value both in the normal and superconducting states. This makes the thermal conductivity measurement a good tool for understanding the superconducting state and its correspondence to the normal state. When a material is cooled below the superconducting transition temperature T_{sc}, the Cooper pairs are formed and the normal electron density n_e reduces with decreasing temperature. On the other hand, the application of magnetic field breaks the Cooper pairs and n_e increases with increasing H. Since the Cooper pairs do not carry heat, the electronic contribution to the thermal conductivity reduces with decreasing temperature below T_{sc}. However, since n_e reduces with temperature, the scattering of phonons by the electrons also reduce at the same time. Hence the phonon thermal conductivity increases with the decrease in temperature in the superconducting state. However, with the reduction in temperature, the number of phonons also reduces, which reduces the phonon thermal conductivity. Thus, there is a competition between these two processes and a peak in the thermal conductivity in the superconducting state is observed at about 0.2 T_{sc} to 0.3 T_{sc} [63]. Similar to the normal state, electrons and phonons carry the heat in the superconducting state also, and the total thermal conductivity in the superconducting state κ_s is given as,

$$\kappa_s = \kappa_{es} + \kappa_{ls} \tag{1.22}$$

here κ_{es} and κ_{ls} are respectively the electronic and phononic thermal conductivity in the superconducting state.

The theory of thermal conductivity in the superconducting state (κ_s) was developed by Bardeen, Rickayzen and Tewordt (BRT) on the basis of the BCS theory of superconductors [64]. This theory is known as the BRT theory [63]. The BRT theory gives the ratio of the thermal conductivity in the superconducting state to that in the normal state limited by the scattering of electrons from disorder, scattering of electrons from phonons, and scattering

of phonons from electrons. Although the BRT theory was developed for low temperature superconductors, it was later extended for high-T_c superconductors also by Tewordt and Wölkahusen [65, 66].

1.6.1 Electronic thermal conductivity in the superconducting state

The BRT theory is based on the law of corresponding states, which states that the ratio of the thermal conductivity in the superconducting state to that in the normal state (κ_n) will be a universal function of T/T_{sc} when one specific scattering mechanism dominates. Considering only scattering of electrons from static defects, the ratio of κ_s to the κ_n is given by [63],

$$\left(\frac{\kappa_s}{\kappa_n}\right)_{ei} = \frac{1}{f(0)}\left[f(-y) + y\ln(1+\exp(-y))\frac{y^2}{2(1+\exp(y))}\right], \tag{1.23}$$

where $y = \Delta(T)/k_BT$ and $f(-y)$ is the Fermi integral given by, $f(-y) = \int_0^\infty \frac{z}{1+\exp(z+y)}dz$. The $\Delta(T)$ is given as [67],

$$\Delta(T) = \Delta_0[\tanh\{1.82[1.018(T_{sc}/T-1)]^{0.51}\}], \tag{1.24}$$

here Δ_0 is the superconducting energy gap at the zero temperature limit. For a BCS superconductor $\Delta_0 = 1.76k_BT_{sc}$.

Similarly, the ratio of κ_s to the κ_n for electron-phonon scattering is given by [63],

$$\left(\frac{\kappa_s}{\kappa_n}\right)_{el} = \frac{\int_1^\infty x\left(x^2-1\right)^{1/2}\operatorname{sech}^2\left(\frac{1}{2}xy\right)[\Gamma_s(xy)]^{-1}dx}{\int_0^\infty z^2\operatorname{sech}^2\left(\frac{1}{2}z\right)[\Gamma_n(z)]^{-1}dz}. \tag{1.25}$$

The functional form of $\Gamma_s(xy)$ is given as [68, 69],

$$\begin{aligned}\Gamma_s(xy) = &\int_0^{x-1} \frac{t^2(x-t-x^{-1})}{[(x-t)^2-1]^{1/2}} \left\{ \left(1+e^{-y(x-t)}\right)^{-1} + \left(e^{yt}-1\right)^{-1} \right\} dt \\ &+ \int_0^{\infty} \frac{t^2(x+t-x^{-1})}{[(x-t)^2-1]^{1/2}} \left\{ \left(1-e^{-yt}\right)^{-1} + \left(1-e^{-y(x+t)}\right)^{-1} \right\} dt \\ &+ \int_{x+1}^{\infty} \frac{t^2(t-x-x^{-1})}{[(t-x)^2-1]^{1/2}} \left\{ \left(1+e^{y(t-x)}\right)^{-1} + \left(e^{yt}-1\right)^{-1} \right\} dt,\end{aligned} \tag{1.26}$$

and $\Gamma_n(z)$ is given as,

$$\Gamma_n(z) = \frac{8}{3}F_2(0) + F_2(z) + F_2(-z), \tag{1.27}$$

where $F_2(\eta) = \int_0^{\infty} t^2(1+e^{t-\eta})^{-1}dt$. Figures 1.8 (a) - (b) show the plots of $\left(\frac{\kappa_s}{\kappa_n}\right)_{ei}$ and $\left(\frac{\kappa_s}{\kappa_n}\right)_{el}$ as a function of T/T_{sc} estimated for $\Delta_0/k_BT_{sc} = 1.76$. Multiplying equations 1.23 and 1.25 by their corresponding normal state thermal conductivity one can find the thermal conductivity in the superconducting state.

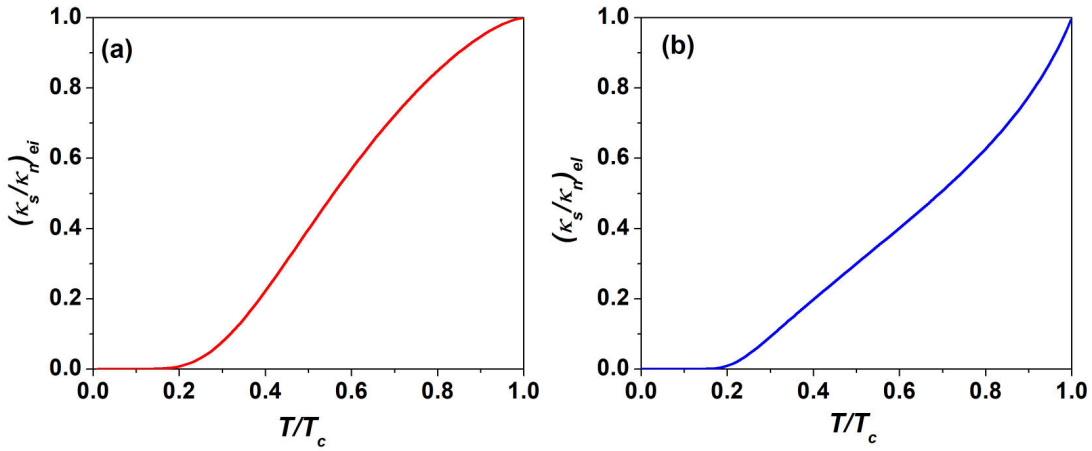

FIGURE 1.8: Ratio of electronic thermal conductivity in the superconducting state to the normal state limited by (a) electron-defect scattering and (b) electron-phonon scattering. The curves in the panel (a) and (b) are generated using Matlab.

1.6.2 Phonon thermal conductivity in the superconducting state

The static defects do not change when a material becomes superconducting. Thus, only the relaxation time due to the scattering of phonons from electrons changes and the phonon thermal conductivity in the superconducting state is given by [70, 71],

$$\kappa_{l,s} = \int_0^\infty dx \frac{x^n e^x}{(e^x-1)^2} \frac{1}{\frac{N_s}{M}\frac{1}{T^3} + \frac{L_s}{M}\frac{x}{T^2} + \frac{E_s}{M}\frac{x}{T^2}g(x) + \frac{P_s}{M}x^4 T}. \tag{1.28}$$

The symbols have usual meaning as before, and the function $g(x)$ gives the ratio of relaxation time in the superconducting state to that in the normal state due to phonon-electron scattering. To obtain the $\kappa_{l,s}$, we have used the functional expression for $g(x)$ given in Ref. [63]. The plots of $g(x)$ for different values of $y = \Delta(T)/k_B T$ and the plot of the ratio of phonon thermal conductivities in the superconducting and normal states limited only by scattering of phonons from electron are shown in figure 1.9.

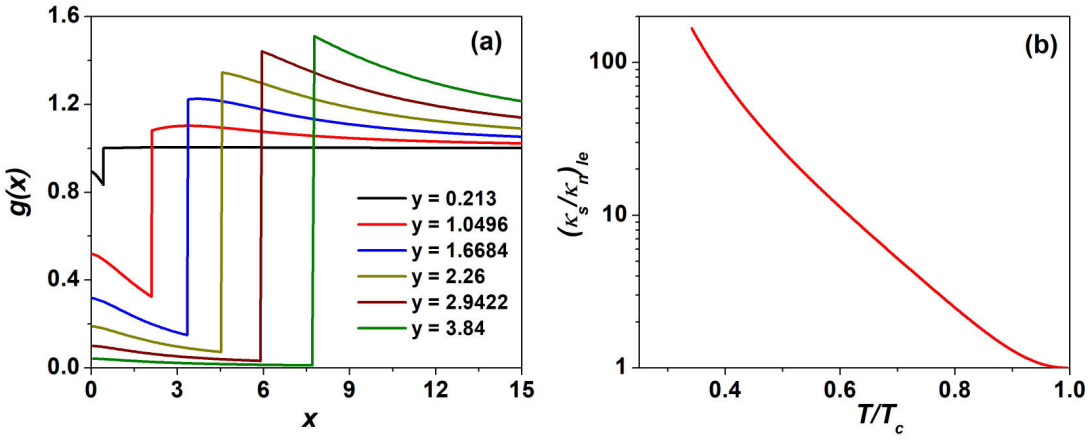

FIGURE 1.9: (a) $g(x)$ for different values of y is shown. The values of $g(x)$ were estimated using Matlab. (b) The ratio of phonon thermal conductivity in the superconducting state to that in the normal state limited by scattering of phonons from electrons according to the BRT theory. The curve is generated using Matlab.

1.7 Motivation of the thesis

The κ and J_c depend heavily on the types and amounts of disorders present in the system. The pinning of flux lines increases with increasing disorder in the system, which increases the J_c. At the same time, the electronic and phononic thermal conductivity reduces with increasing disorder due to increased scattering. Therefore, to optimize a material for practical applications, it is important to have the knowledge regarding how J_c and κ are affected by the presence of various defects.

The $\kappa(T)$ of V with different amount of disorder has been studied extensively [72, 73]. But there are very few reports available on the κ of the $V_{1-x}Ti_x$ alloys. Morton *et al.* have studied the $\kappa(T)$ of the $V_{1-x}Ti_x$ alloys at low temperatures. The value of κ reported by them is almost two orders of magnitude higher than similar alloys [74] and has been doubted by other authors [75]. Thus, a detailed study of the κ of the $V_{1-x}Ti_x$ alloys considering the disorders present in the system is very much required at present.

In a previous study, Matin *et al.* shown that the moderate J_c of the $V_{1-x}Ti_x$ alloys is due to the low grain boundary density in these alloys. Thus, the grain refinement seems to be an effective method to enhance the J_c of the $V_{1-x}Ti_x$ alloys. The rare earth (RE) alloys have been extensively used for grain refinement in various steel and high entropy alloys [76, 77, 78, 79]. Therefore, we find it worthwhile to study the effect of the addition of RE elements into the $V_{1-x}Ti_x$ alloys. The addition of RE element is expected to increase the disorder in the system and the J_c, but might in turn affect the κ of the $V_{1-x}Ti_x$ alloys.

Another system we mentioned as an alternate to the commercial superconductors is the C15 ZrV_2 based superconductors. Some of these brittle C15 superconductors have J_c even higher than the Nb_3Sn superconductors. Alloying and off-stoichiometry methods may be useful [80] in improving the mechanical properties of such brittle materials. Thus, studying the J_c and κ of the off-stoichiometric $V_{1-x}Zr_x$ alloys instead of the ZrV_2 based compounds looks useful towards finding a suitable superconductor alternate to the Nb based materials.

With this motivation, we study the J_c and κ of the $V_{1-x}Ti_x$, $V_{0.60-x}Ti_{0.40}Gd_x$ and $V_{1-x}Zr_x$ alloys, and present them in this thesis.

1.8 Plan of the thesis

Our results on the J_c and κ of the alloys are complemented by structural studies performed with the help of X-ray diffraction (XRD) and metallography. Having introduced the topics in Chapter 1, Chapter 2 describes different measurement techniques used for the work. We have discussed our results on the normal and superconducting state thermal conductivity of the $V_{1-x}Ti_x$ alloys in Chapter 3. Our results show that the presence of large amount of disorder and strong electron-phonon coupling lead to the dominance of phonon thermal conductivity over the electronic thermal conductivity in the superconducting state of these metallic alloys. Chapter 4 presents our results on the effect of Gd addition on the J_c of the $V_{0.60}Ti_{0.40}$ alloy. We found that the reduction in the grain size due to the addition of Gd increases the pinning at the grain boundaries, which leads to the enhancement of J_c in these alloys. For the alloy with 1% Gd, the J_c is enhanced by more than 20 times than the parent alloy. In Chapter 5, we present the analysis of the normal and superconducting state thermal conductivities of the $V_{0.60-x}Ti_{0.40}Gd_x$ alloys. Chapter 6 discusses the structural and magnetic properties of the as-cast $V_{1-x}Zr_x$ alloys. The J_c of some of these alloys were found to be high. The J_c of the $x = 0.40$ alloy is in the same order of magnitude as that of the commercial Nb-Ti superconductor. Our study shows that by choosing proper composition and heat treatments, the J_c of these alloys can be enhanced. We have discussed the temperature dependence of C and κ of the $V_{1-x}Zr_x$ alloys in Chapter 7. The κ in the superconducting state of these alloys was found to be more than that expected theoretically, due to the presence of two parallel channels (normal and superconducting) of heat conduction. In Chapter 8, we have summarised the work and presented the conclusions of the thesis. At the end of this chapter, the directions for possible future studies are presented.

Chapter 2

Experimental details

This chapter describes the methods of sample preparation, characterization and various measurement techniques used in the present study. All the V-Ti, V-Zr, Gd-added $V_{0.60}Ti_{0.40}$ alloys studied here were prepared using an arc melting furnace. The alloys were characterized using the X-Ray Diffraction (XRD) and metallography. Some of the alloys were further characterized using the Energy Dispersive X-ray Spectroscopy. The temperature and field dependence of the thermal and magnetic properties of these alloys were investigated after the characterization.

2.1 Sample preparation

The $V_{1-x}Ti_x$ (x = 0 - 0.7), $V_{1-x}Zr_x$ (x = 0 - 0.40) and $V_{0.60-x}Ti_{0.40}Gd_x$ (x = 0 - 0.02) alloys were synthesized by melting the constituting elements in a tri-arc furnace (Centorr Vacuum Industries, Model 5TA) under 99.999% pure Argon (Ar) atmosphere. The suffix for each element indicates their atomic ratio in the corresponding alloy. Figure 2.1 shows an image of the main components of the furnace.

In an arc-melting furnace, the electrical arc is generated using the principle of electric discharge. The generated arc is then used to melt the elements. The furnace has two main components – a hearth and three electrodes. The hearth with the elements has one electrical polarity while the electrodes have the opposite polarity. When sufficient voltage difference is created between the elements and the electrodes, the arc is generated. The water-cooled lower

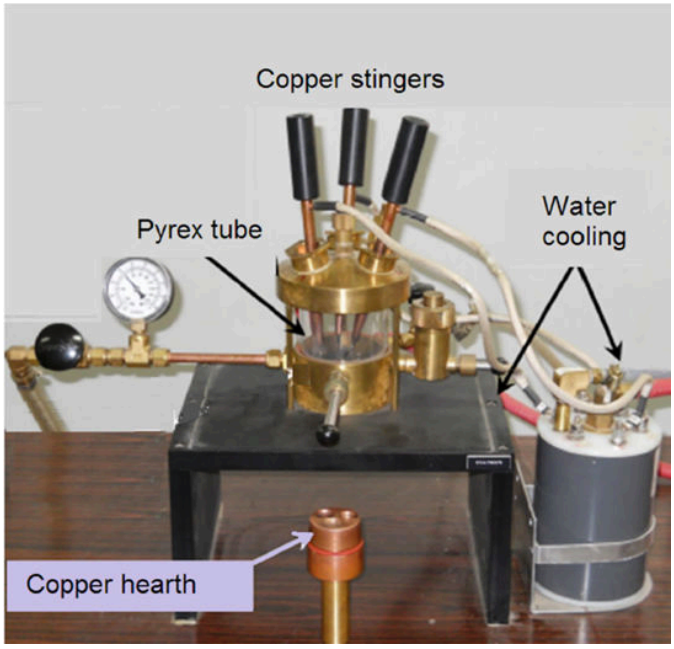

FIGURE 2.1: Arc melting furnace (model 5TA from Centorr Vacuum Industries).

and upper sections of the furnace is separated by a Pyrex tube. Three copper stingers with tungsten electrodes are inserted from the upper section of the furnace as shown in figure 2.1. The elements required to synthesize a sample are cleaned, dried, taken in stoichiometric ratios and placed on the copper hearth. A ball of Ti is used as a getter material. The tapered copper hearth with the elements and the Ti-getter (placed in a separate cavity in the hearth) is then loaded through a tapered hole at the bottom of the furnace. The melting chamber is then purged and backfilled with 99.999% pure Ar gas through leak-proof inlet and outlet ports. To melt the sample, an arc is created by applying a small current of $\sim$ 50 A, then the arc is brought onto the sample and the current is increased to the required value to melt the charge. During melting, the Ti-getter is melted first and while the getter is in red hot condition, the sample-charge is melted. A continuous flow of the pure Ar gas is maintained during the whole melting process. A button shaped ingot is obtained after the melting. The ingots are flipped and re-melted 5 more times to ensure homogeneity of the sample. The mass loss during the melting process is found to be negligible. The as-cast samples are then

cut using a low speed diamond saw (Buehler Inc.) into different shapes and sizes required for structural characterization and various other measurements.

2.2 X-ray diffraction

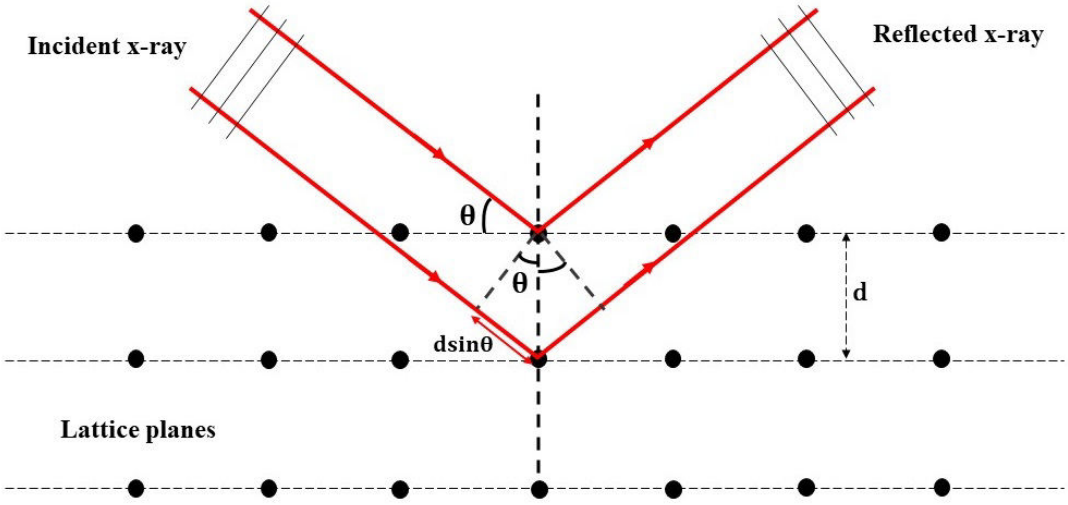

FIGURE 2.2: Schematic of X-ray diffraction.

XRD measurements are used to determine the crystal structure of the alloys. Figure 2.2 shows the schematic of XRD from two parallel planes of a material. For a material with inter-planer spacing 'd' and the incident angle 'θ', the path difference between the reflected rays from two adjacent planes is $2dsin\theta$. For constructive interference [81, 82],

$$2dsin\theta = n\lambda, \tag{2.1}$$

which is the Bragg's law and is used to estimate the lattice parameters of a material. The XRD measurements in this thesis were performed in a Bruker D8 ADVANCE diffractometer. The sample is scanned in Theta-Theta geometry using Cu-K_α (average wavelength λ = 1.54060 Å) radiation in this diffractometer, which is equipped with a LYNXEYE detector.

2.3 Metallography

The metallography micrographs provide information about the grain size, presence of dislocations, impurity phases etc. The micrographs of some of the present alloys were taken using an optical microscope. Before taking the images, the samples were polished, cleaned and etched chemically to reveal the microstructure. The following steps were followed to prepare the samples for metallography.

Grinding and polishing: Small pieces of samples were cut and cleaned using acetone. Moulds were prepared by mixing resin (90% vol.) and hardener (10% vol.) with the sample attached to them. The moulds were then cured overnight at room temperature till a hard mould was obtained. The samples were then ground in sequence using 240 grit, 400 grit, 600 grit and 1200 grit SiC paper. After each step of grinding, the samples were cleaned with soap solution, dried and examined under an optical microscope to ensure that all the scratches from the previous step have been removed. After adequate grinding, the samples were polished in sequence using 6 μm, 3 μm, 1 μm and 0.25 μm diamond paste. Before moving to the next step, the samples were cleaned carefully to remove any trace of diamond paste remaining on the sample.

Etching: The polished surfaces of the alloys were then chemically etched as described below. To prepare the etchant for the $V_{1-x}Ti_x$ alloys, a solution of 1 ml HNO_3 and 1 ml of HF was added to 100 ml water. For the $V_{1-x}Zr_x$ and $V_{0.60-x}Ti_{0.40}Gd_x$ alloys, an aqueous solution of HNO_3 and HF (1ml HNO_3: 1 ml of HF: 50 ml water) was used as the etchant. The polished surfaces of the alloys were then wiped for 5 seconds using cotton buds wetted in the etchant and checked under a microscope after cleaning. The last step was repeated till microstructures were visible.

The images of the etched samples were captured using in a high-power optical microscope (Olympus, PME-3). Images with magnifications up to 100 times of the actual size of the sample were taken using this microscope. Figure 2.3 shows the metallography images of (a) V and (b) $V_{0.4}Ti_{0.6}$ alloy. The optical image of V shows both grain boundaries and

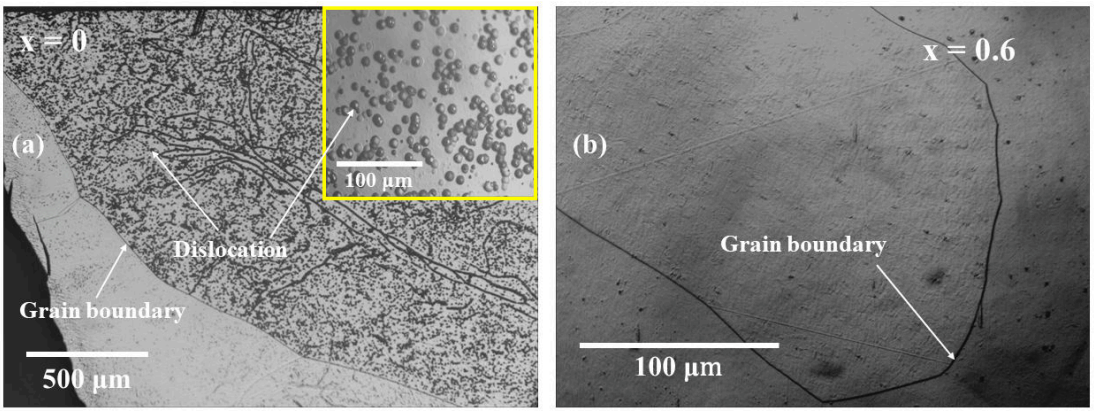

FIGURE 2.3: Optical metallography images of (a) V and (b) $V_{0.4}Ti_{0.4}$ alloy. Metallography image of V shows both grain boundaries and dislocations (etch pits in the inset), whereas only grain boundaries are visible for the $x = 0.6$ alloy.

dislocations (etch pits in the inset), whereas only grain boundaries are visible for $x = 0.6$ alloy.

2.4 Scanning electron microscopy

Scanning electron microscopy is a powerful tool for high resolution imaging of a sample surface. In a scanning electron microscope (SEM), the sample surface is scanned using a focused beam of high energy electrons. The schematic diagram of a SEM is shown in figure 2.4.

The electron beam generated from an electron gun passes through electromagnetic lenses (condenser and objective lenses respectively) and falls on the sample surface. A scanning coil is used to move the incident electron beam over the sample surface. The high energy electron beam interacts with the sample and produces different signals, e.g., secondary electrons, back-scattered electrons, characteristic X-rays etc. In a traditional SEM, the secondary electrons are collected to reveal the surface morphology. Figure 2.5 shows the SEM images of the $V_{1-x}Zr_x$ (x = (a) 0.20 & (b) 0.40) alloys.

The images were taken using a Nova NanoSEM 450 instrument (FEI Company, USA)

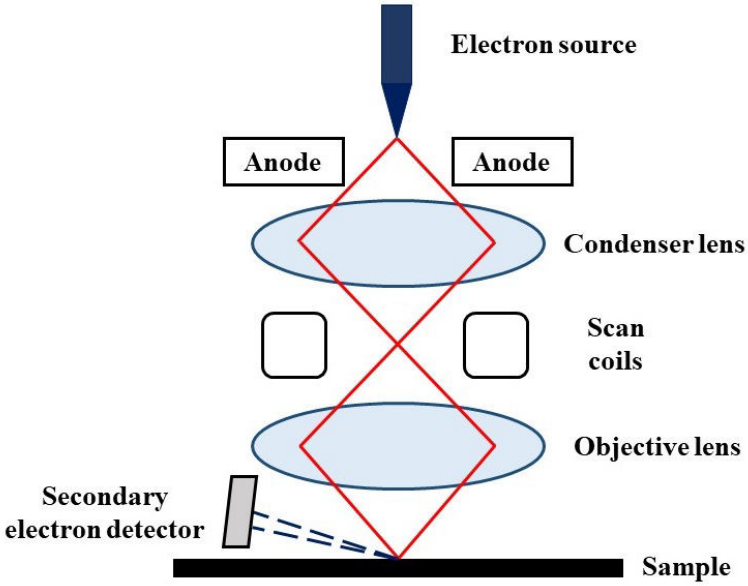

FIGURE 2.4: Schematic of the basic components of a SEM set up.

that operates at 18 kV. The Nova NanoSEM 450 has a 110 × 100 mm, 5-axis, motorized, eucentric stage and the navigation of the sample is supported by an in-chamber camera [83]. A resolution of 1 nm can be obtained in this instrument.

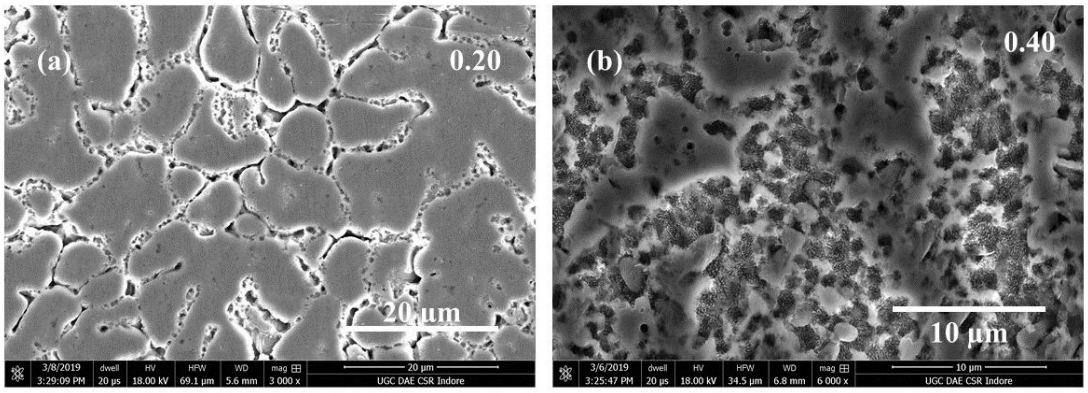

FIGURE 2.5: SEM images of $V_{1-x}Zr_x$ alloys for x = (a) 0.20 and (b) 0.40.

2.5 Energy dispersive spectroscopy

Energy dispersive spectroscopy (EDS) is a useful technique for elemental analysis of a sample. It is normally used in conjugation with the SEM and is based on the fact that each element has a different electronic structure. When an element is bombarded with electrons with sufficient energy, the electrons from the atoms near the surface get knocked out. This creates an electron vacancy which is filled by an electron from a higher energy state. As the electron jumps from the higher energy state, a characteristic X-ray is emitted corresponding to the energy difference between the levels. Thus, measuring the energy difference and relative intensities, one can identify the elements and estimate the relative abundance of a specific element in the sample.

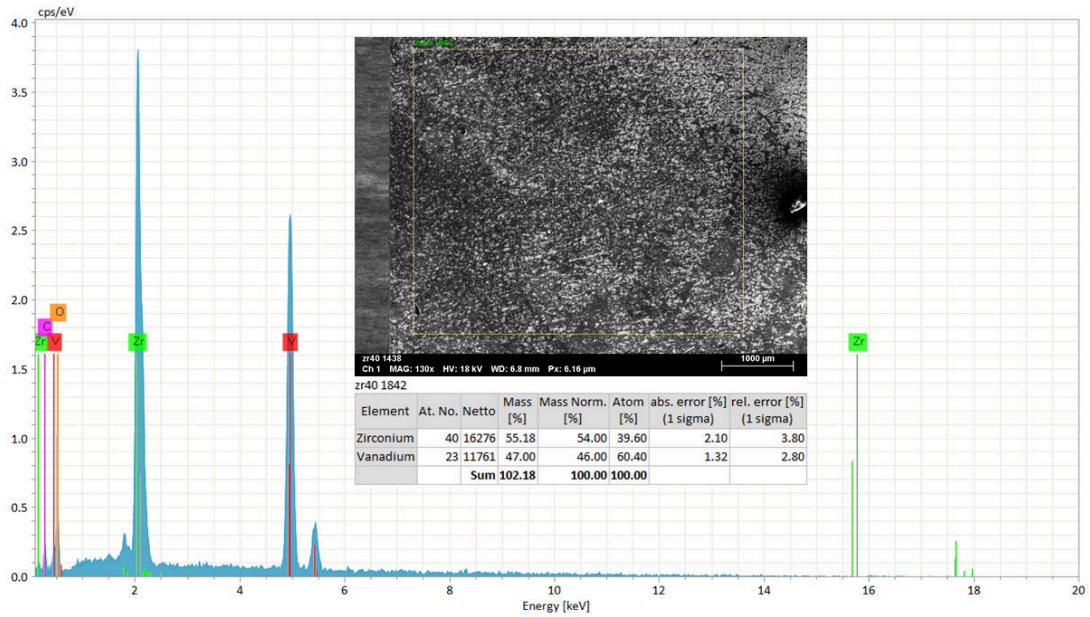

Element	At. No.	Netto	Mass [%]	Mass Norm. [%]	Atom [%]	abs. error [%] (1 sigma)	rel. error [%] (1 sigma)
Zirconium	40	16276	55.18	54.00	39.60	2.10	3.80
Vanadium	23	11761	47.00	46.00	60.40	1.32	2.80
		Sum	102.18	100.00	100.00		

FIGURE 2.6: EDS spectrum of the $V_{0.60}Zr_{0.40}$ alloy. The rectangle in the inset shows the area over which the spectrum is obtained. The spectrum indicates the presence of V and Zr only with 60 and 40 stoichiometric ratios respectively.

The EDS spectrum of the alloys presented in this thesis was estimated using a X-flash 6130 energy dispersive spectroscopy attachment (Bruker, Germany) and the Esprit software. The X-flash 6130 has an energy resolution of 123 eV at Mn-K_α, 45 eV at C-K_α and 53 eV at

F-K_α with a solid angle of 30 mm^2 active area chip [84]. Figure 2.6 shows a characteristic EDS spectrum of the $V_{0.60}Zr_{0.40}$ alloy.

2.6 Electrical resistivity measurement

The phonons and the disorder in the lattice scatter the electrons moving in a metal. For electrons moving under the influence of electric potential, this hindrance to the electron motion gives rise to the electrical resistance. Thus, the temperature and field dependence of electrical resistance can give information about different scattering mechanisms present in the system. Measuring the voltage drop along a sample through which a constant current is flowing, we can find the resistance (R) of the material using Ohm's law. Measuring the cross-section of the sample (A) and the separation of the voltage leads (l), we can estimate the resistivity (ρ) of the material using the expression, $\rho = R\frac{A}{l}$. The resistivity of the present alloys varies from few $\mu\Omega$cm to few hundred $\mu\Omega$cm. Hence, a four-probe configuration was used to measure the electrical resistivity of these samples. Figure 2.7 shows a schematic configuration of the four-probe measurement set up.

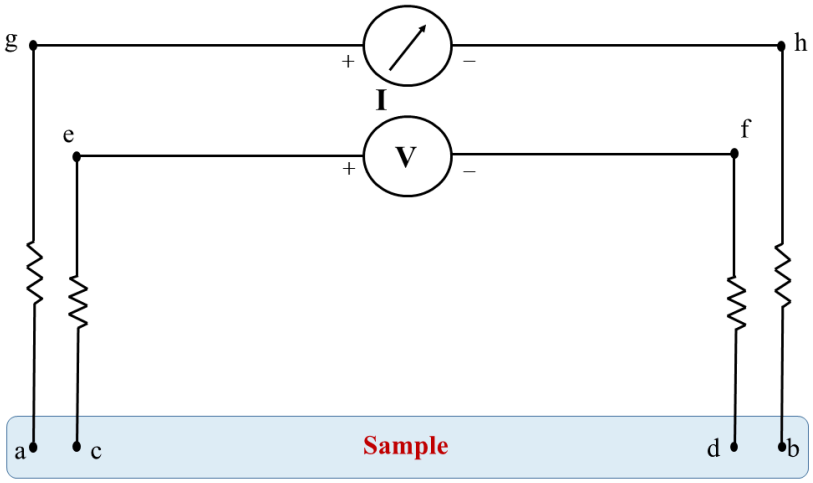

FIGURE 2.7: Schematic representation of the four-probe resistivity measurement technique.

The voltage difference across the voltmeter (V) is given by,

$$V_{cd} = V_{ec} + V_{ef} + V_{df}. \tag{2.2}$$

The voltmeter has a very high input impedance of the order of 10^9 Ω to 10^{12} Ω. This makes the current passing through the voltmeter practically zero. Thus $V_{ec} = V_{df} \approx 0$, and equation 2.2 becomes,

$$V_{ef} = V_{cd}. \tag{2.3}$$

For a test current I, the resistance of the sample becomes,

$$(R_{cd})_{sample} = \frac{V_{cd}}{I}. \tag{2.4}$$

By measuring the sample dimensions, the resistivity of the sample can be obtained. The electrical resistivity of the samples presented in this thesis has been measured in 9 T and 16 T Physical Property Measurement System (PPMS, Quantum Design, USA) in four-probe configuration, where the ρ can be measured in the temperature range 1.8-400 K for a magnetic field of 0 to ± 9 T (9 T PPMS) or ± 16 T (16 T PPMS). The experimental error in the resistivity was observed to be less than 1% of the measured values.

2.7 Magnetization measurement

The magnetization (M) of a material can be measured experimentally using both direct and indirect measurement techniques. The direct techniques involve the force methods, which include the Faraday balance, torque magnetometer etc. and the flux methods that include the vibrating sample magnetometer (VSM) and Superconducting Quantum Interference Device (SQUID) magnetometer. The indirect measurement techniques include Hall effect, magneto-optical Kerr effect, nuclear magnetic resonance, neutron scattering, Mossbauer effect etc., in which a known relation between the measured property and the magnetic property of the

material is used to estimate M. We have used a VSM (Quantum Design, USA) and a closed cycle refrigerator-based SQUID-VSM (MPMS-3, Quantum Design, USA) to measure the temperature and field dependence of magnetization of the samples reported in this thesis. The magnetization can be measured in the temperature range 1.8 K to 400 K for a magnetic field 0 to $\pm$ 7 T in the SQUID-VSM. In the VSM, the M can be measured in the temperature range 1.8 K to 400 K for a magnetic field 0 to $\pm$ 16 T. The SQUID-VSM has an ultimate resolution of $\sim 10^{-7}$ emu, whereas for the VSM, the resolution is $\sim 10^{-5}$ emu. Although the SQUID-VSM has much better sensitivity than the VSM, the measurement process is much faster in the VSM [85]. The working principle of SQUID-VSM and VSM is described in the following sections.

The temperature dependence of magnetization ($M(T)$) of the present samples are measured using the zero-field-cooled (ZFC) warming, field-cooled-cooling (FCC) and field-cooled-warming (FCW) protocols. Before every measurement, to remove any trapped field in the superconducting solenoid, a high magnetic field (1 T) is applied and the field is oscillated back to zero. During ZFC, the sample is cooled down to the lowest temperature of measurement in the absence of any applied magnetic field. The magnetic field is switched on and the $M(T)$ is measured while warming up the sample. During FCC, the magnetic field is switched on at a temperature higher than the superconducting transition temperature (T_{sc}) and the $M(T)$ is measured while cooling down the sample. During FCW, the $M(T)$ is measured while warming up the sample after it is cooled down to the lowest temperature during FCC. The $M(H)$ measurements on the present samples have always been started from a ZFC state.

2.7.1 Vibrating sample magnetometer (VSM) [86, 87]

The VSM works on the principle of Faraday's law of electromagnetic induction. According to this law, a voltage is developed in an electromagnetic loop placed in a time varying magnetic field. The schematic of a VSM is shown in figure 2.8.

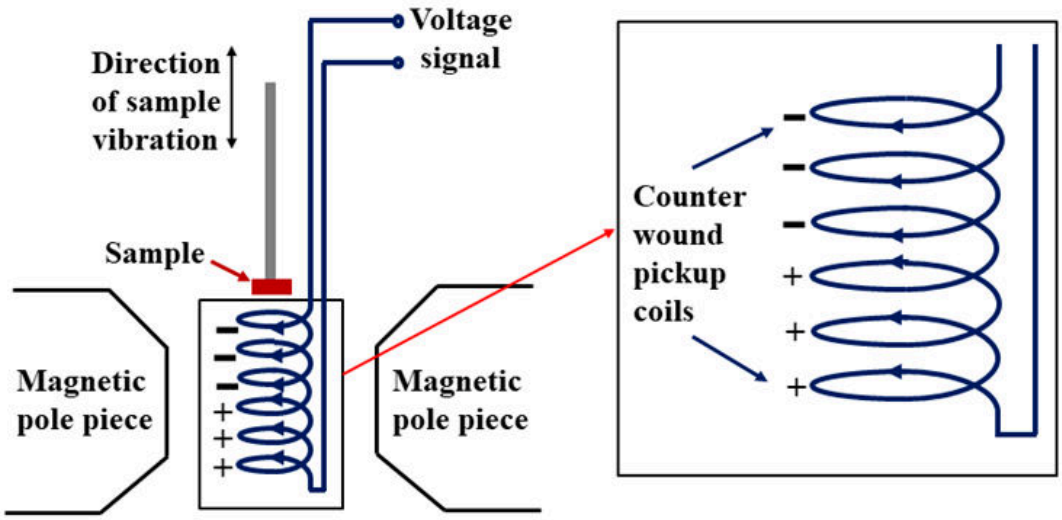

FIGURE 2.8: Schematic diagram of the experimental configuration of the vibrating sample magnetometer (VSM, Quantum Design, USA) [86, 87]. The pickup coils are wound in the second order gradiometer configuration.

The periodic vibration of the sample in the detection coil leads to a periodic change of the magnetic flux linked with the detection coil. This leads to the generation of a periodic voltage in the detection coil with the same frequency as that of the sample vibration. The voltage across the detection coil depends on various parameters like, sample vibration, frequency and amplitude of vibration and the distance of the sample from the detection coil. As the sample distance from the detection coil, frequency and amplitude of vibration are fixed before the measurement in the VSM, the voltage across the detection coil is directly proportional to the magnetic moment of the sample.

2.7.2 SQUID-VSM [88]

A SQUID-based magnetometer consists of superconducting loops with Josephson junctions. The basic working principle of the SQUID is based on the fact that the magnetic flux linked with this superconducting circuit is in the multiples of flux quantum $\Phi_0 = h/2e$, where h is the Planck's constant and e is the electronic charge. This quantization of magnetic flux occurs due to the quantum interference of the electron pair wave functions. A schematic of

the MPMS-3 SQUID-VSM is shown in figure 2.9 (a). Figure 2.9 (b) depicts the 2ω detection principle used for the measurement of M in the MPMS-3 SQUID-VSM magnetometer. As the sample moves up-down in the detection coil (shown in figure 2.9), it generates a current in the detection coil, which is inductively coupled to the instrument's SQUID sensor (as shown in figure 2.9). The SQUID sensor precisely converts the current into voltage, which is amplified and digitized by the instrument electronics [88].

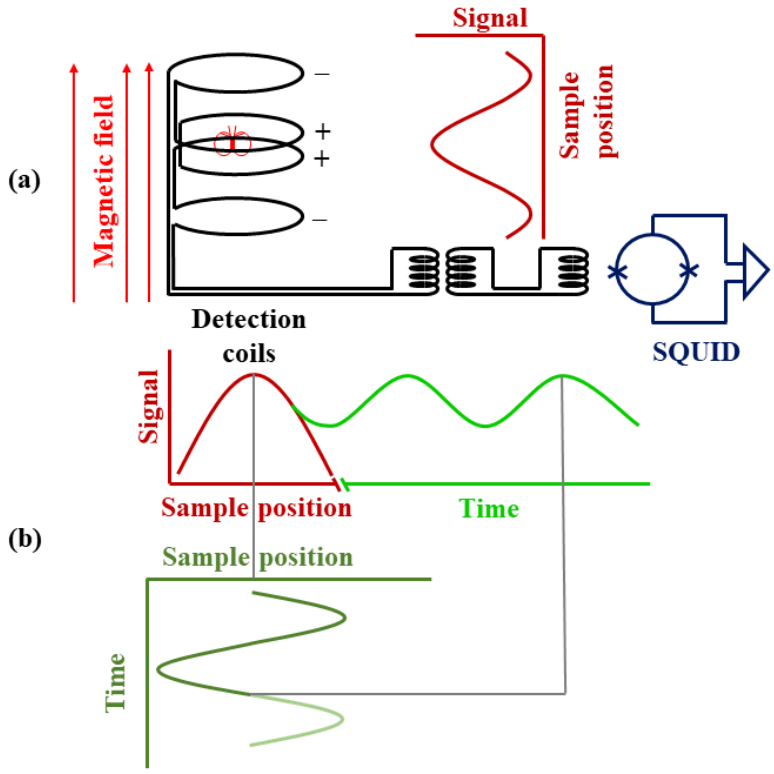

FIGURE 2.9: (a) Schematic of the detection technique in the MPMS-3 SQUID-VSM. (b) 2ω detection principle used for magnetic moment measurement in the MPMS-3 SQUID-VSM (Quantum Design, USA) [diagram reconstructed from Ref. [88]].

To measure the magnetic moment in the MPMS-3 SQUID-VSM, the sample vibrates at the centre of the superconducting detection coil at a frequency ω. At this position the SQUID sensor shows the maximum signal with respect to the sample position z as shown in figure 2.9 (b). For small sample vibrations about the centre of the detection coil, the SQUID signal V as a function of sample position z is $V(z) = Az^2$ and the sample position as a

function of time t is $z(t) = B\sin(\omega t)$, which in combination gives the SQUID signal as a function of time t, as [88],

$$V(t) = AB^2\sin^2(\omega t). \tag{2.5}$$

Here, A is a scaling factor relating to the magnetic moment of the sample and B is the amplitude of the sample vibration. Since $\sin^2(\omega t) = \frac{1}{2} - \frac{1}{2}\cos(2\omega t)$, equation 2.5 becomes,

$$V(t) = \frac{AB^2}{2}(1 - \cos(2\omega t)). \tag{2.6}$$

Equation 2.6 shows that the signal at frequency 2ω is exclusively from the sample and can be accurately measured using the lock-in technique.

2.8 Heat capacity measurement [89]

The heat capacity of a material is defined as the amount of heat required to be added or subtracted to change the temperature of the system by one degree. If the temperature of a system changes (adiabatically) from T_i to T_f ($T_f > T_i$) when an amount of heat Q is added, then the average heat capacity of the system (C) is given by,

$$C = \frac{Q}{T_f - T_i}. \tag{2.7}$$

As Q and $(T_f - T_i)$ becomes smaller, C approaches a limiting value for $(T_f - T_i) \sim 0$ and is given by,

$$C = \left(\frac{dQ}{dT}\right)_{T=T_i}. \tag{2.8}$$

This method of estimation of heat capacity is known as the adiabatic method. This method has very good accuracy for big samples at high temperatures, but the accuracy of the C estimated using this method becomes poor for small samples at low temperatures as

the heat leak cannot be neglected in comparison with the power supply. The thermal relaxation technique gives a fairly accurate estimate of the heat capacity for the small samples. In this method, the sample temperature is raised by very small amount ΔT over a constant bath temperature T_0 (usually $\Delta T/T_0 \sim 1\%$). The temperature decreases exponentially as the heat supply is turned off. Assuming one dimensional heat flow, if the time constant of relaxation is τ, the heat capacity of the sample is given by, $C = K_W \tau$, where K_W is the thermal conductance of the connecting wires between the sample and the heat bath (see figure 2.10). The heat capacity of the samples used in the present work were measured in a 9 T PPMS using the thermal relaxation technique. A calorimeter is used to thermally insulate the sample from the surroundings. Figure 2.10 shows a schematic of the set up used to measure the sample heat capacity [89] in a PPMS.

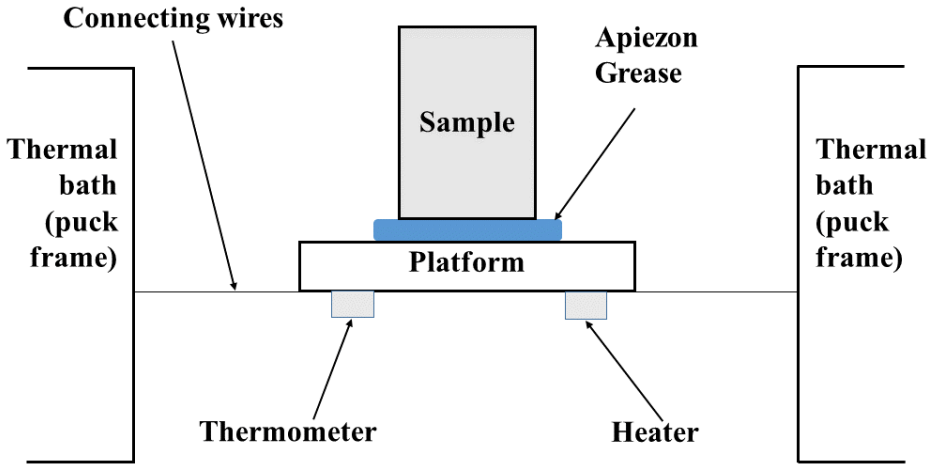

FIGURE 2.10: Schematic diagram of the heat capacity measurement setup in PPMS. (Image reconstructed from [89])

A heater and a thermometer are attached (deposited) at the bottom of the sample platform. Thin, small wires made of gold alloy provide electrical connection to the heater and thermometer. These wires also provide support to the sample platform and thermal anchoring between the puck frame and the sample platform. The sample is mounted on the platform

using a thin layer of thermally conducting grease which provides the necessary thermal contact between the sample and sample platform. An in-built cryopump provides a vacuum $\sim$ 0.1 mTorr to minimize the heat loss. The whole sample assembly is covered using a thermal shield to reduce heat loss by radiation. There are three steps of heat capacity measurement −

I. Calibration

II. Addenda measurement

III. Sample heat capacity measurement.

The calibration is done in two steps. First, the resistances of the puck thermometer and platform thermometer are measured while cooling from the highest temperature and a table of resistance values at different temperatures is obtained therefrom. In the second step the thermal conductance of the connecting wires and the resistance of the platform heater are calibrated. These two steps are repeated for different magnetic fields to obtain the calibration for the magnetoresistance effects. During the addenda measurement, a small amount of conducting grease is applied on the sample platform and the heat capacity of the platform with the grease is measured. Finally, the sample is attached to the grease on the platform and the total heat capacity along with the sample is measured. The heat capacity of the sample is obtained by subtracting the addenda heat capacity from the total heat capacity obtained with the sample.

Two different analysis models are available for finding the sample heat capacity, depending upon the thermal contact between the sample platform and the sample.

1. Simple model: This model is used when the thermal contact between the sample and the sample platform is perfect and these is no temperature difference between the sample and sample platform. The heat balance equation in such a case is given by [89],

$$C_t \frac{dT_p}{dt} = P_w(t) - K_W(T_p(t) - T_b), \tag{2.9}$$

where C_t is the total heat capacity of the sample and the platform. T_b and T_p are respectively bath (puck frame) and sample platform temperatures. P_w is the applied heater power. The heater power equals to a constant P_0 during the heating cycle and 0 during the cooling cycle. The time constant of temperature relaxation (τ) is obtained as, $\tau = C_t/K_W$. The addenda heat capacity (C_A) is obtained using simple model with $C_t = C_A$.

2. Two-tau model: In this model apart from the temperature difference between the puck frame and the sample platform, a temperature difference exists between the sample and sample platform due to poor thermal contact across the conducting grease. The heat balance equation in such a case is given by [89],

$$C_p \frac{dT_p}{dt} = P_w(t) - K_W(T_p(t) - T_b) + K_g(T_s(t) - T_p(t)), \tag{2.10}$$

and

$$C_m \frac{dT_s}{dt} = -K_g(T_s(t) - T_p(t)), \tag{2.11}$$

here C_p and C_m are respectively the heat capacities of the sample platform and sample. K_W and K_g are thermal conductances of the connecting wires and the grease. T_s is the sample temperature. In the two-tau model, the relaxation of temperature between puck-frame and sample platform, and between sample platform and the sample are both considered. Hence, two time-constants are involved in the thermal relaxation process. They are given as, $\tau_1 = \frac{1}{\alpha+\beta}$ and $\tau_2 = \frac{1}{\alpha-\beta}$ [89], where

$$\alpha = \frac{1}{2}\left[\frac{K_W}{C_p} + \frac{K_g}{C_p} + \frac{K_g}{C_m}\right], \tag{2.12}$$

and

$$\beta = \sqrt{\frac{K_g^2 C_m^2 + K_g^2 C_m C_p + K_g^2 C_p^2 + K_W^2 C_m^2 + 2K_W K_g C_m^2 - 2K_W C_m K_g C_p}{2C_m C_p}}. \tag{2.13}$$

The experimental temperature response is fitted with K_g and C_m as fitting parameters, whereas K_W is taken from the calibration. While using the two-tau model, the addenda heat capacity C_A is taken as the platform heat capacity C_p. The thermal contact between the sample platform and the sample is defined in terms of the sample coupling, given by $\frac{K_g}{K_g+K_W} \times 100$ %. Heat capacity of the samples presented in this thesis has been measured in 9 T and 16 T PPMS. The heat capacity can be measured in the temperature range 1.8 - 400 K for magnetic fields from 0 to $\pm$ 9 T (9 T PPMS) or $\pm$ 16 T (16 T PPMS). Before every measurement, the PPMS software determines the sample coupling. If the sample coupling is 100%, the simple model is used and for sample coupling less than 100%, the two-tau model is used to estimate the sample heat capacity. For sample coupling less than 90%, the data is considered erroneous and better sample preparing procedures (e.g. polishing the sample surface to enhance the sample coupling) are used. The experimental error in the heat capacity was observed to be less than 2.5% of the measured values.

2.9 Thermal conductivity measurement [90]

According to Fourier's theory of one-dimensional heat flow, the rate flow of heat $\left(\frac{dQ}{dt}\right)$ from one face of a sample to the opposite face is given by,

$$\frac{dQ}{dt} = -\kappa A \frac{dT}{dx}, \tag{2.14}$$

where A is the area of each face and $\frac{dT}{dx}$ is the thermal gradient. Thus, for $A = 1$ and $\frac{dT}{dx} = 1$, we get $\frac{dQ}{dt} = \kappa$.

The thermal conductivity κ of a material is the amount of heat flowing per second through a sample from one face to the opposite face having unit surface area, when a unit thermal gradient is maintained between them.

The thermal conductivity of the samples reported in this thesis was measured in a 9 T PPMS, where the thermal conductivity can be measured in the temperature range 1.8-400 K

for magnetic fields from 0 to $\pm$ 9 T.

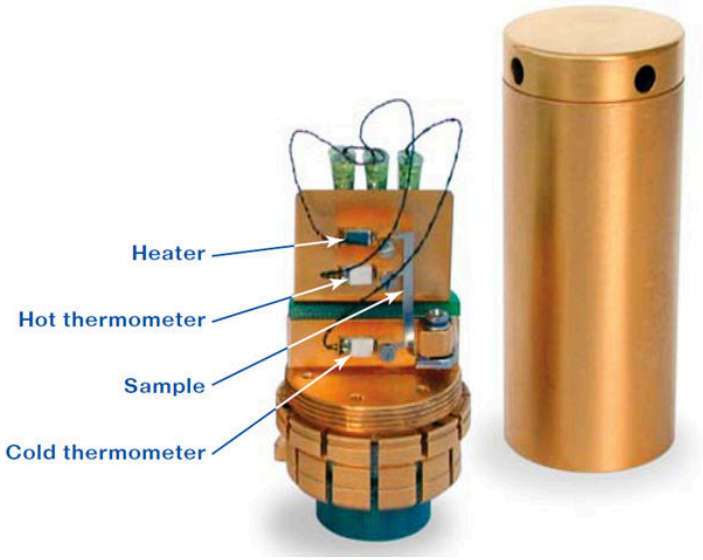

FIGURE 2.11: Thermal conductivity puck along with the sample and the thermal shield used in the PPMS (taken from ref. [91]).

Figure 2.11 shows the image (taken from ref. [91]) of the thermal conductivity puck along with the standard sample used to measure the thermal conductivity in the PPMS. The heater and the thermometers are also connected. The necessary thermal gradient for the thermal conductivity measurements is created using the heater, and the temperature difference between the hot and cold thermometers is recorded as ΔT.

There are two measurement modes for the measurement of κ of the sample in the PPMS.

1. Single measurement mode: In this mode, the temperature is stabilized in both the hot and cold thermometer ends and the offset is measured. Then a heat pulse is applied and maintained until the steady state thermal gradient is achieved. After the thermal equilibrium is achieved, the thermal conductivity of the material is measured. As the system is required to reach equilibrium at each temperature, data acquisition in the single measurement mode is very slow.

2. Continuous measurement mode: Maldonado developed an ac method to measure the

thermal conductivity continuously. In this method, the bath temperature is continuously varied and a square wave heat pulse is used to generate the thermal gradient. This square pulse generates a piecewise exponential signal for the temperature gradient across the sample. Measuring the relaxation time for the temperature, the thermal conductivity of the material can be estimated [92]. A similar model is followed in the PPMS to measure the thermal conductivity continuously [90]. In the continuous measurement mode, the thermal conductivity is recorded continuously and an adaptative software is used to optimize the various parameters (e.g. heater power, heating period etc.) to obtain a ΔT (thermal gradient) vs. time curve. The time response of the hot and cold end temperatures and the temperature gradient with the application of the square pulse for an ideal sample is shown in figure 2.12.

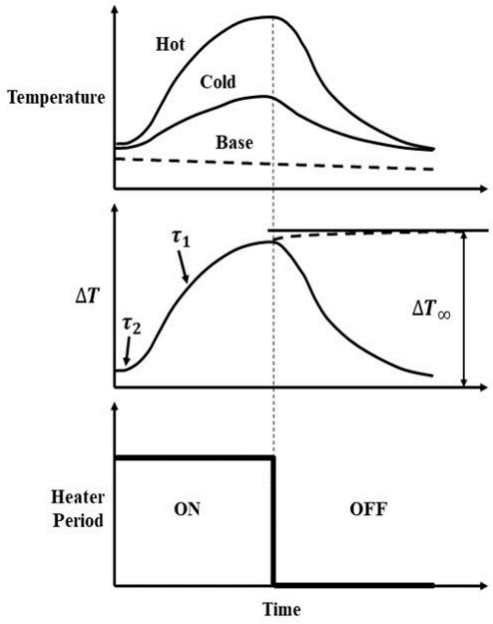

FIGURE 2.12: Time response of temperatures and the temperature gradient with the application of the square pulse in the heater (Image reconstructed from [90]).

When the ΔT vs. time data is obtained, a non-linear least square fitting is used to fit the data using the empirical formula [90],

$$\Delta T_{model} = \Delta T_\infty \left[1 - \tau_1 exp(-t/\tau_1) - \tau_2 exp(-t/\tau_2)/(\tau_1 - \tau_2)\right], \tag{2.15}$$

where ΔT_∞ is the temperature drop across the sample if the heater is left on for indefinite time, τ_1 and τ_2 are two empirical time constants. The fitting routine optimizes these parameters to minimize the residual (error) in the curve fit.

2.9.1 Correction due to heat loss

It is not possible to directly measure the actual heat flux in the sample. So, the heat conducted through the sample is determined by subtracting the heat losses from the applied heater power. There are two sources of heat loss – one is due to radiation P_r and the other is conduction down the leads from the sensor and heater assemblies, given by K_s. Thus, the net conduction is given by [90],

$$K = (I^2R - P_r)/\Delta T - K_s. \tag{2.16}$$

Here K_s and P_r are given as follows [90],

$$K_s = aT + bT^2 + cT^3, \tag{2.17}$$

and

$$P_r = \frac{S}{2}\sigma_s\epsilon(T_{hot}^4 - T_{cold}^4), \tag{2.18}$$

where a, b, c are constants, S is the sample surface area, ϵ is the infrared emissivity and σ_s is the Stefan-Boltzmann constant. The factor $\frac{1}{2}$ comes from the approximation that only half of the sample surface is at hot temperature and this part of the sample surface radiates the heat. The major source of error in the thermal conductivity measurement comes from the inaccuracy in measuring the ΔT. We observed that the experimental error in the thermal conductivity was observed to be less than 2.5% of the measured values.

Chapter 3

Thermal Conductivity of $V_{1-x}Ti_x$ alloys

The $V_{1-x}Ti_x$ alloy superconductors have a J_c of $> 10^8$ A/m^2 in the zero field limit, and possess good mechanical properties [4, 5, 6]. Since, their J_c values are still about two orders of magnitude lower than the commercial Nb-Ti alloys, one may think of increasing the defects/disorders in the system to improve the J_c. These defects however, become scattering centres for the electrons and phonons, and limit the heat flow. Therefore, the knowledge of thermal conductivity of the $V_{1-x}Ti_x$ alloys would be beneficial for technological applications. However, the thermal conductivity of the $V_{1-x}Ti_x$ alloys has not been studied in detail. In this chapter, we provide a detailed analysis on the temperature dependence of thermal conductivity ($\kappa(T)$) of the $V_{1-x}Ti_x$ (x = 0, 0.1, 0.3, 0.5, 0.6 and 0.7) alloys in both the normal and superconducting states.

3.1 Results and discussion

3.1.1 Structural characterization

The room temperature XRD patterns of the $V_{1-x}Ti_x$ alloys are shown in figure 3.1. Details of the XRD measurements are available in the section 2.2 of chapter 2. The $V_{1-x}Ti_x$ alloys used in this study form in the body centred cubic (*bcc*) structure (space group $Im\bar{3}m$) [93, 94] and the peaks corresponding to the *bcc* phase are indexed in the figure. The two peaks marked by '*' appearing at the same positions for all the samples are from the sample holder.

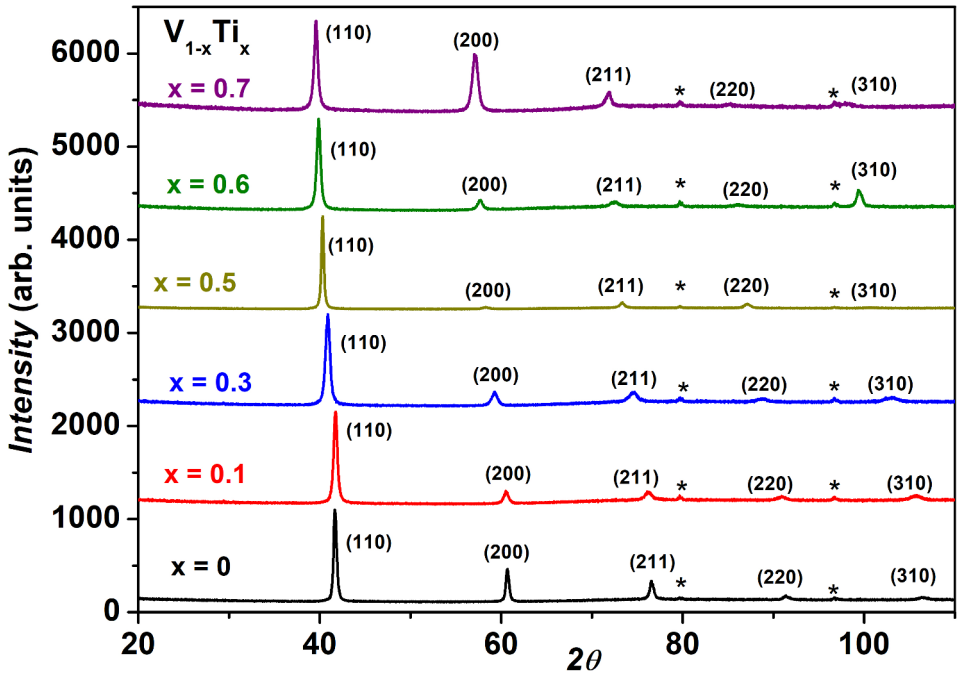

FIGURE 3.1: X-ray diffraction patterns of the $V_{1-x}Ti_x$ alloys.

As discussed in chapter 1, the $\kappa(T)$ of a metal is given by, $\kappa(T) = \kappa_e(T) + \kappa_l(T)$, where $\kappa_e(T)$ and $\kappa_l(T)$ are the electronic and phononic thermal conductivities respectively. According to the kinetic theory, $\kappa = \frac{1}{3}Cvl$, where C, v, l are respectively the heat capacity, velocity and the mean free path of the heat carrier. Using the experimentally obtained heat capacity values [95] and taking the velocity of electrons and phonons respectively as the Fermi velocity ($\sim 10^6$ m/s) and velocity of sound ($\sim 10^3$ m/s) in the $V_{1-x}Ti_x$ alloys at 10 K, the ratio κ_l/κ_e comes out to be $\sim 10^{-5} l_l/l_e$, where l_l and l_e are respectively the mean free path of the phonons and electrons. This shows that at low temperatures, the electrons carry majority of the heat, as expected in the metallic systems. The Wiedemann-Franz (WF) law gives a rough estimation of the amount of heat carried by electrons in a metal at low temperatures. According to the WF law [19], the κ_e is given as, $\kappa_e(T) = L_0 T/\rho(T)$, where L_0 ($L_0 = 2.44\times10^{-8}$ W Ω K^{-2}) is the Lorenz number and $\rho(T)$ is the electrical resistivity. We therefore study the $\rho(T)$ of the $V_{1-x}Ti_x$ alloys.

3.1.2 Electrical resistivity of the $V_{1-x}Ti_x$ alloys

Figure 3.2 (a) shows the $\rho(T)$ of the $V_{1-x}Ti_x$ ($x = 0 - 0.7$) alloys in the temperature range 2 - 300 K in the absence of any magnetic field. The $\rho(T)$ of V increases with increasing temperature indicating that the effective mean free path (l_e) of the conduction electrons reduces with increasing temperature [96]. Using an argument based on the uncertainty relation, Ioffe and Regal [97, 98, 99] showed that the metallic state of a material cannot survive indefinitely with the increase in temperature. They argued that the theory of metallic electronic conduction breaks down when l_e approaches the inter atomic distance d_a. This is known as the Ioffe-Regal criterion. According to the Ioffe-Regal criterion a metal to insulator transition is observed for [99, 100],

$$k_F l_e \approx 1, \tag{3.1}$$

here k_F is the Fermi wave vector. According to free electron theory, $k_F l_e = \hbar(3\pi^2)^{2/3}/(e^2\rho n^{1/3})$, where e is the electronic charge and n is the density of the electrons in the material. Mott also gave a similar argument on the of minimum metallic conductivity [101] and equation 3.1 thus became known as the Mott-Ioffe-Regal (MIR) limit. It becomes problematic to interpret the MIR criterion physically if $k_F l_e \approx 1$ is taken. The k_F is given by $k_F = \pi/d_a$, thus l_e becomes d_a/π, which is much smaller than atomic spacing. Mott suggested $k_F l_e \approx \pi$ [101], which makes $l_e \approx d_a$. According to Elliott, an electron loses phase memory while moving from one atom to another atom for $l_e < d_a$ and an insulating state is observed [100, 102]. Although the increase in disorder reduces l_e to the order of d_a, a quantum metal to insulator transition (Anderson transition [103, 104]) is never observed in a 3D metallic system even in the extreme level of disorder. Gantmakher studied the $\rho(T)$ of high-resistive alloys with a quantum correction using first-order perturbation theory [105]. He showed that the electrons get localized in these alloys due to scattering from the disorder. However, a system with high electron density does not transform into a state with multifractal wave functions due to the presence of disorder [106]. This prohibits the observation of strong localization and thus an actual insulating state is not observed. The resistivity saturation in

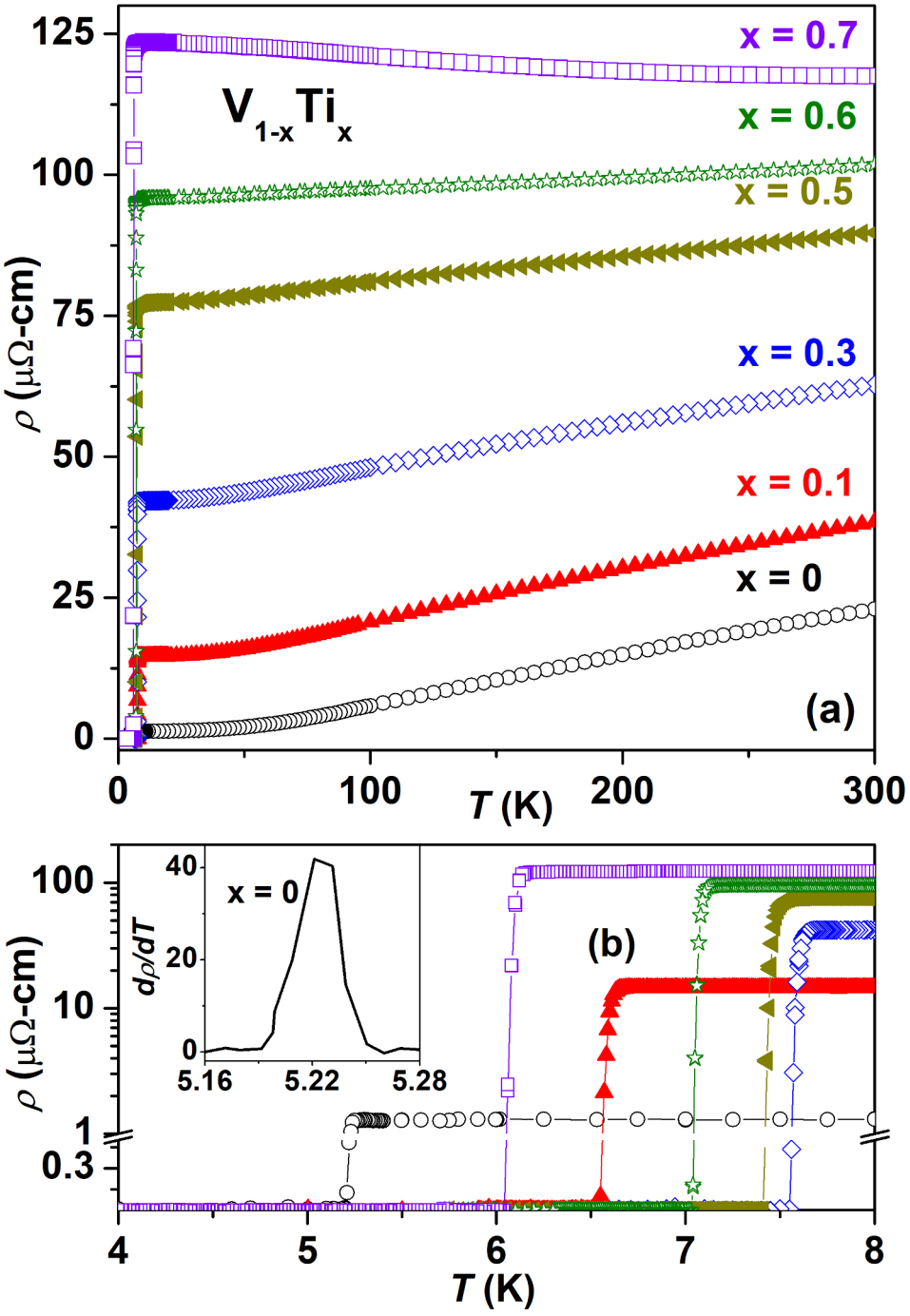

FIGURE 3.2: (a) Temperature dependence of electrical resistivity (ρ(T)) of the $V_{1-x}Ti_x$ alloys in the temperature range 2- 300 K in the absence of applied magnetic field. Residual resistivity (ρ_0) increases and the coefficient of temperature dependence of resistivity also changes from positive for $x = 0$ to negative for $x = 0.7$. The ρ(T) of the $V_{1-x}Ti_x$ alloys near the superconducting transition is shown in the figure (b). Inset to (b) shows the $d\rho/dT$ for V. The $d\rho/dT$ is maximum at 5.22 K, which corresponds to the superconducting transition temperature (T_{sc}).

various elements (La [107], Ti [108]), A15 compounds (Nb_3Sn [109, 110], Nb_3Ge [110], Nb_3Pt [111], V_3Si [111], Mo_3Ge [112]) and in other alloys and intermetallics ($Ti_{1-x}Al_x$ [108, 113], In_5B_3 [114], $Fe_{80-x}Ni_xCr_{20}$ [115]) are known for the manifestation of the MIR criterion. This special case of MIR criterion is called Mooij criterion [113]. For a typical metal, the condition $l_e \approx d_a$ is achieved for a resistivity $\sim$ 100 - 300 $\mu\Omega$ cm and a crossover between positive temperature coefficient of resistivity (TCR) to the negative TCR is observed in this resistivity range [113].

The residual resistivity (ρ_0 defined as the ρ (8 K)) of the $V_{1-x}Ti_x$ alloys increases from 1.29 $\mu\Omega$ cm for V to 123.48 $\mu\Omega$ cm for the $x = 0.7$ alloy. The residual resistivity ratio (RRR, defined as ρ(300 K)/ρ(8 K)) also decreases with increasing x and drops to 0.951 for the x = 0.7 alloy. The RRR < 1 indicates that these alloys are highly disordered. Table 3.1 lists the values of ρ_0 and RRR for the $V_{1-x}Ti_x$ alloys. The TCR goes from positive to negative in the $V_{1-x}Ti_x$ alloys as x is increased to 0.7 in V, which is in line with the Mooij criterion [113]. According to Sommerfeld theory of electronic conduction, the l_e is given by [62],

$$l_e = \frac{(r_s/a_0)^2 \times 92}{\rho}, \tag{3.2}$$

where r_s is the radius of the sphere that has a volume equal to the volume occupied by each conduction electron in the system and a_0 is the Bohr radius. The resistivity is taken in $\mu\Omega$ cm and the l_e is given in Å. The ρ(8 K) has been used to estimate the l_e. V and Ti have electronic structures [Ar]$3d^24s^2$ and [Ar]$3d^24s^2$ respectively. Thus, the r_s has been estimated considering 5 and 4 conduction electrons for V and Ti respectively. The minimum inter atomic distance for a *bcc* system is given by, $d_a = \sqrt{3}a/2$. Here, a is the lattice parameter. We have used the value of a obtained from the XRD pattern. The values of l_e, a and d_a of the $V_{1-x}Ti_x$ alloys are listed in table 3.1. We can see from table 3.1, the l_e decreases with the increasing Ti content and falls below d_a for the $x = 0.7$ alloy that shows negative TCR. Figure 3.2 (b) shows the $\rho(T)$ of the $V_{1-x}Ti_x$ alloys near the superconducting transition. The superconducting transition temperature (T_{sc}) is taken as the temperature at

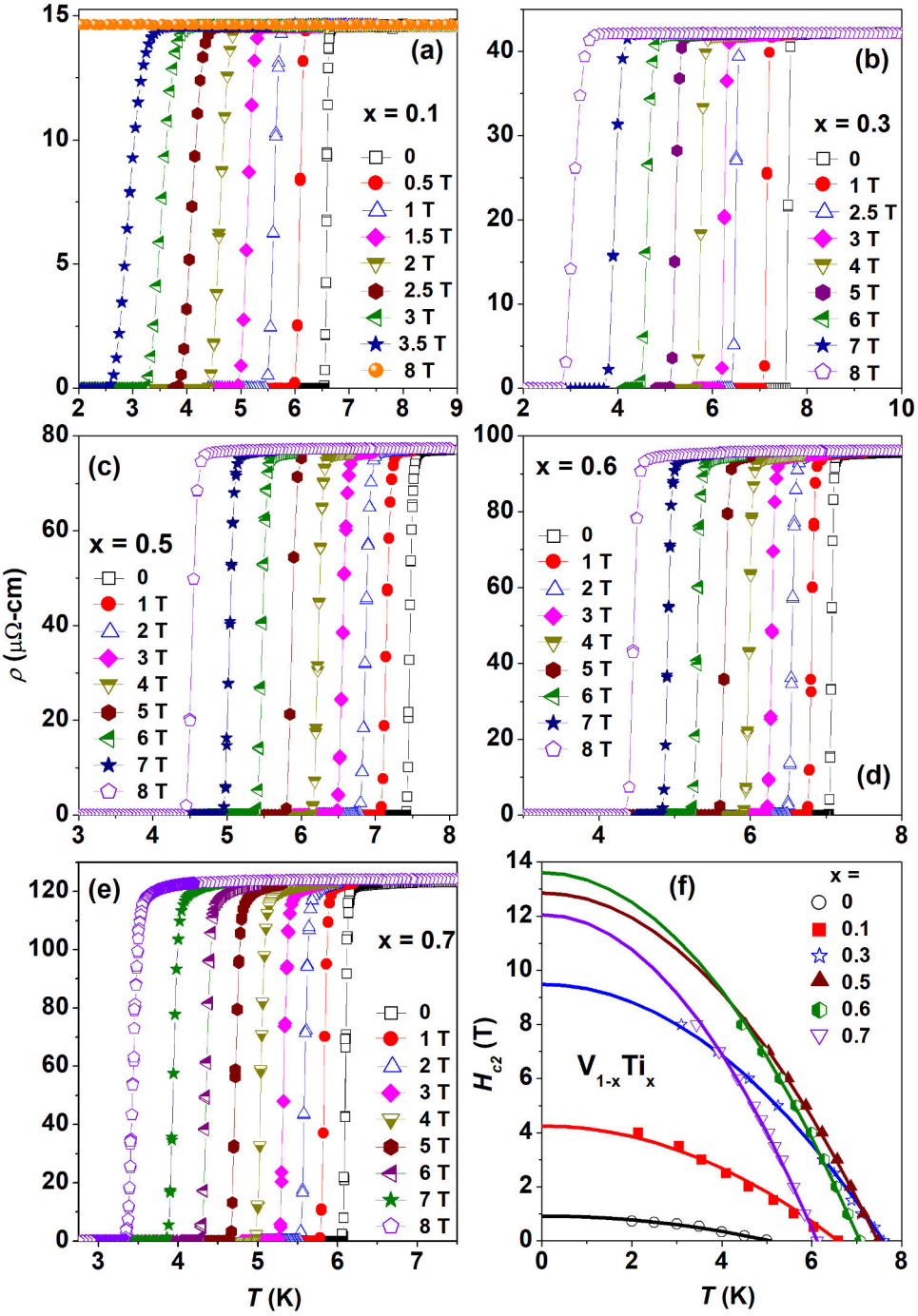

FIGURE 3.3: (a)-(e) Temperature dependence of electrical resistivity (ρ(T)) of the $V_{1-x}Ti_x$ alloys in the presence of different magnetic fields. (f) Plot of H_{c2} as a function of temperature for all the alloys. The symbols correspond to the experimentally obtained data points, whereas the lines show fit to the experimentally obtained H_{c2}.

which the $d\rho/dT$ is maximum. The inset to figure 3.2 (b) shows the $d\rho/dT$ of V. The T_{sc} of V is 5.22 K. Similar procedure has been followed to estimate the T_{sc} of all the alloys (table 3.1).

TABLE 3.1: Different parameters obtained from the resistivity and XRD of the $V_{1-x}Ti_x$ alloys.

x	T_{sc} (K)	ρ_0 ($\mu\Omega$cm)	RRR	l_e (nm)	a (nm)	d_a (nm)	$H_{c2}(0)$ (T)	$\xi(T \to 0)$ (nm)
0	5.22 $\pm$0.01	1.29 $\pm$ 0.06	17.85	19.3 $\pm$0.5	0.304 $\pm$0.001	0.263 $\pm$0.001	0.92 $\pm$0.02	18.9 $\pm$0.4
0.1	6.59 $\pm$0.01	14.60 $\pm$ 0.12	2.63	1.76 $\pm$ 0.01	0.306 $\pm$0.001	0.265 $\pm$0.001	4.25 $\pm$0.09	8.8 $\pm$0.2
0.3	7.60 $\pm$0.01	42.16 $\pm$ 0.35	1.50	0.65 $\pm$ 0.01	0.311 $\pm$0.001	0.269 $\pm$0.001	9.49 $\pm$0.07	5.89 $\pm$0.08
0.5	7.47 $\pm$0.01	77.33 $\pm$ 0.23	1.69	0.38 $\pm$ 0.01	0.316 $\pm$0.001	0.274 $\pm$0.001	12.86 $\pm$0.07	5.06 $\pm$0.06
0.6	7.07 $\pm$0.02	96.16 $\pm$ 0.20	1.07	0.32 $\pm$ 0.01	0.319 $\pm$0.001	0.276 $\pm$0.001	13.61 $\pm$0.12	4.92 $\pm$0.07
0.7	6.12 $\pm$0.02	123.48 $\pm$ 0.10	0.95	0.25 $\pm$ 0.01	0.322 $\pm$0.001	0.279 $\pm$0.001	12.06 $\pm$0.09	5.22 $\pm$0.08

Figures 3.3 (a) - (e) show the $\rho(T)$ of the $V_{1-x}Ti_x$ alloys at low temperatures in the presence of different magnetic fields, whereas figure 3.3 (f) shows the corresponding curves $H_{c2}(T)$. The $H_{c2}(T)$ of these alloys follow the relation $H_{c2}(T) = H_{c2}(0)(1-(T/T_{sc})^2)$ [24], shown by the fitted line. Using the $H_{c2}(0)$ values obtained from the fitting, the coherence length in the zero temperature limit is estimated as, $\xi\ (T \to 0) = \sqrt{\Phi_0/(2\pi H_{c2}(0))}$, where Φ_0 is the magnetic flux quantum. The $\xi\ (T \to 0)$ for the alloys is about an order of magnitude higher than the l_e. This is in line with the observation of relatively high $T_{sc}(H=0)$ in the $V_{1-x}Ti_x$ alloys even in the extremely disordered state. We observe that the l_e of these alloys decreases significantly with increasing x and for the alloys with $x \geq 0.3$, the l_e is close to the MIR limit. In such a case, κ_e is suppressed to its minimum value.

The loss of electrons in the superconducting state might lead to the observation of some interesting behaviour in the $\kappa(T)$. In the following section we discuss the $\kappa(T)$ of the $V_{1-x}Ti_x$ alloys.

3.1.3 Temperature dependence of thermal conductivity of the $V_{1-x}Ti_x$ alloys

Figures 3.4 (a) - (f) show the $\kappa(T)$ of the $V_{1-x}Ti_x$ alloys. The black circles and the red square symbols correspond to the thermal conductivity in the normal ($\kappa_n(T)$) and superconducting ($\kappa_s(T)$) states respectively. The $\kappa_s(T)$ has been measured in the absence of magnetic field. The upper critical field (H_{c2}) of the alloys with $x \geq 0.3$ is much higher than 8 T (the maximum field we apply). Therefore, the $\kappa_n(T)$ was obtained by measuring the thermal conductivity down to 4.5 K in the presence of an 8 T magnetic field. The κ_n reduces by almost an order of magnitude when Ti is added in V. The blue lines in the figure 3.4 correspond to the $\kappa_e(T)$ estimated using the WF law, which indicates that below 8 K, the electrons carry more than 70% of heat in the normal state of these alloys. However, the WF law considers the scattering of electrons from the static defects only. We are therefore cautious about using the WF law in the temperature range where scattering of electrons from phonons contribute significantly to the electrical resistivity.

Figure 3.4 (a) shows that the $\kappa_s(T)$ of V starts to reduce with the reduction of temperature below T_{sc}, which is the expected case for a metallic superconductor where electrons dominate the heat conduction. The $\kappa_s(T)$ for the $x = 0.1$ alloy starts to reduce initially as the temperature is reduced below T_{sc} but then start to increase around 4.5 K with further reduction in T. The difference between the κ_n and κ_s for the $x = 0.1$ alloy is very small. When more Ti is added in V, the κ_s starts to increase with the reduction in temperature below T_{sc}. The observation of $\kappa_s > \kappa_n$ below T_{sc} indicates that the phonons carry majority of the heat in the superconducting state of the $V_{1-x}Ti_x$ alloys for $x \geq 0.3$. The rise of κ_s below T_{sc} is observed in systems like the ceramic superconductors (high-T_{sc} superconductors [65, 116, 117, 118],

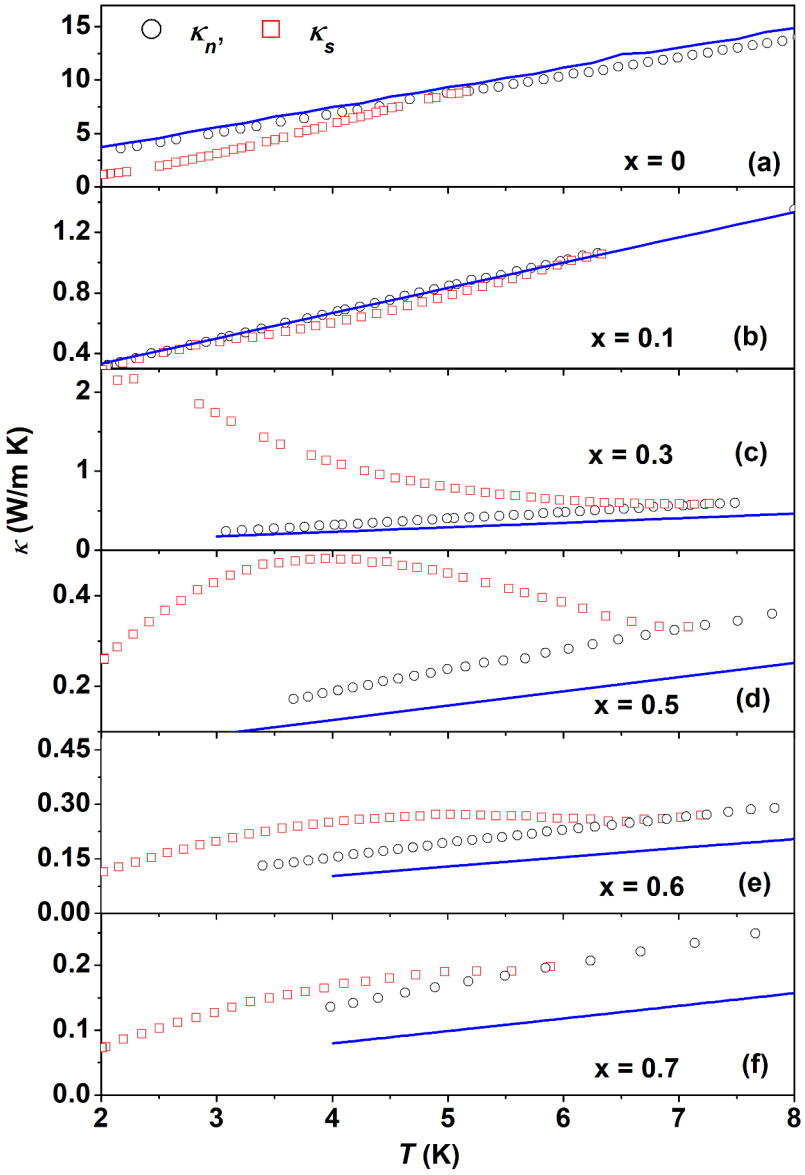

FIGURE 3.4: (a)-(f) Temperature dependence of thermal conductivity ($\kappa(T)$) of the $V_{1-x}Ti_x$ alloys in the absence of applied magnetic field (red open square) and in the presence of 8 T magnetic field (black open circle). The blue line is the electronic thermal conductivity estimated using the Wiedemann-Franz law.

NbC [119]) and amorphous superconductors [120, 121, 122, 123, 124, 125]. The free carrier density in high-T_{sc} superconductors is about two orders of magnitude less than the metals [126] and the lack of crystallinity in the amorphous superconductors strongly suppresses the electronic thermal conductivity. As a result, the phonons carry majority of the heat in the normal state of these systems. When such materials become superconducting, the scattering of phonons from electrons reduces due to the reduction of n_e and this causes the κ_s to rise with the reduction of temperature. The $V_{1-x}Ti_x$ alloys being a crystalline metallic system, this rise of κ_s in the superconducting state is surprising. To understand this, we have analysed the $\kappa_n(T)$ and $\kappa_s(T)$ of the $V_{1-x}Ti_x$ alloys considering the scattering of electrons and phonons from various defects.

3.1.4 Analysis of the thermal conductivity of the $V_{1-x}Ti_x$ alloys in the normal and superconducting states

Information about the Debye temperature (θ_D) is required to fit κ_e and κ_l using the equations 1.15 and 1.19. The superconducting energy gap (Δ_0) is required to estimate the electronic and phononic thermal conductivities in the superconducting state. We have obtained the θ_D and Δ_0 from the temperature dependence of heat capacity ($C(T)$) of these alloys and used these experimentally obtained values to estimate the κ_{es} and κ_{ls} using equations 1.23, 1.26 and 1.28. Different kinds of defects scatter the phonons differently and cause changes to the T dependence of κ_l. Thus, the knowledge of the defects present in the system is necessary for analyzing κ_l. For this, we have performed metallography studies on these alloys.

Temperature dependence of heat capacity of the $V_{1-x}Ti_x$ alloys

The $C(T)$ curves for the $V_{1-x}Ti_x$ (x = 0, 0.1, 0.3, 0.5, 0.6 and 0.7) alloys in the T range 2 - 10 K is shown in the figures 3.5 (a) - (f). The empty and filled symbols correspond to the $C(T)$ for H = 0 and H = 8 T respectively. Sharp jump is observed at the T_{sc} with a transition width less than 0.3 K for all the alloys. The superconducting transition moves

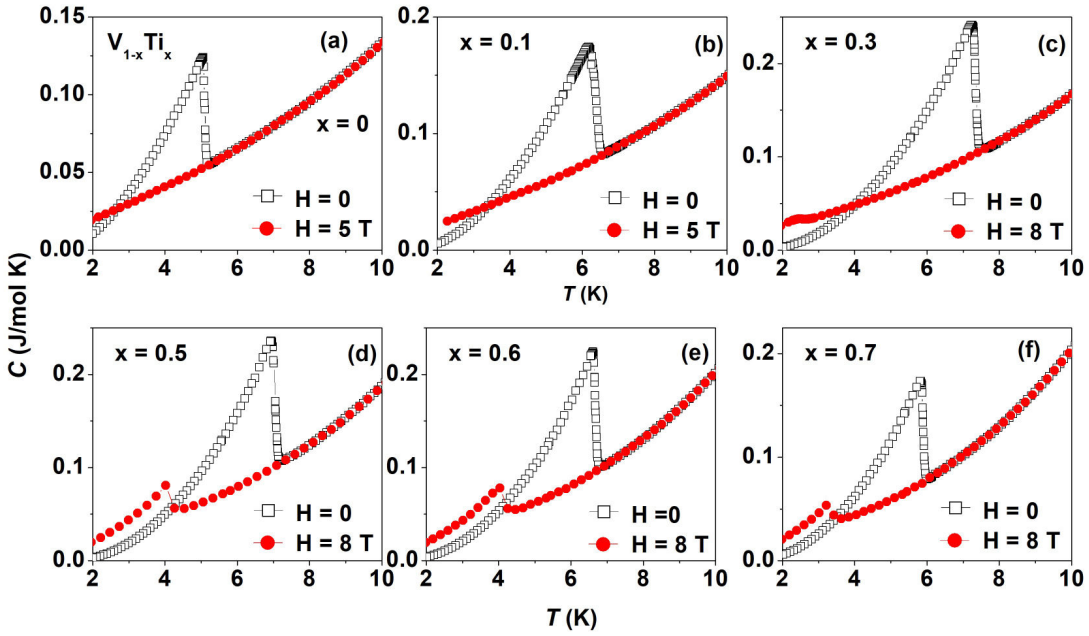

FIGURE 3.5: (a) - (f) Temperature dependence of heat capacity of the $V_{1-x}Ti_x$ alloys in the temperature range 2 - 10 K.

towards lower temperatures with the application of magnetic field. For $H = 8$ T, the alloys up to $x = 0.1$ remain normal for T down to 2 K, whereas the alloys with $x \geq 0.3$ become superconducting between 2.5 - 4.5 K. The low T heat capacity in the normal state (C_n) is given by, $C_n = C_{en} + C_{ln} = \gamma T + \beta T^3$. Here, C_{en} is the electronic heat capacity and C_{ln} is the phononic heat capacity. The $\gamma = (\pi^2/3)k_B^2 N(0)$ and β are respectively the Sommerfeld coefficient and the coefficient of the phononic heat capacity. Here, $N(0)$ is the electronic density of states at the Fermi level. Figure 3.6 shows the linear fit to the C/T vs. T^2 data for the $V_{1-x}Ti_x$ alloys. The symbols and lines in figure 3.6 are respectively the experimental data and the fit to the same. The γ and β are obtained from the intercept and slope of the linear fit. The Debye temperature (θ_D) is estimated as, $\theta_D = \sqrt[3]{1943.66/\beta}$. Figures 3.7 (a) and (b) respectively show the plots of γ and θ_D as a function of the Ti concentration. The γ increases initially with the addition of Ti up to 30% Ti in V and decreases subsequently with further increase of Ti content. The θ_D decreases monotonically with increasing Ti content.

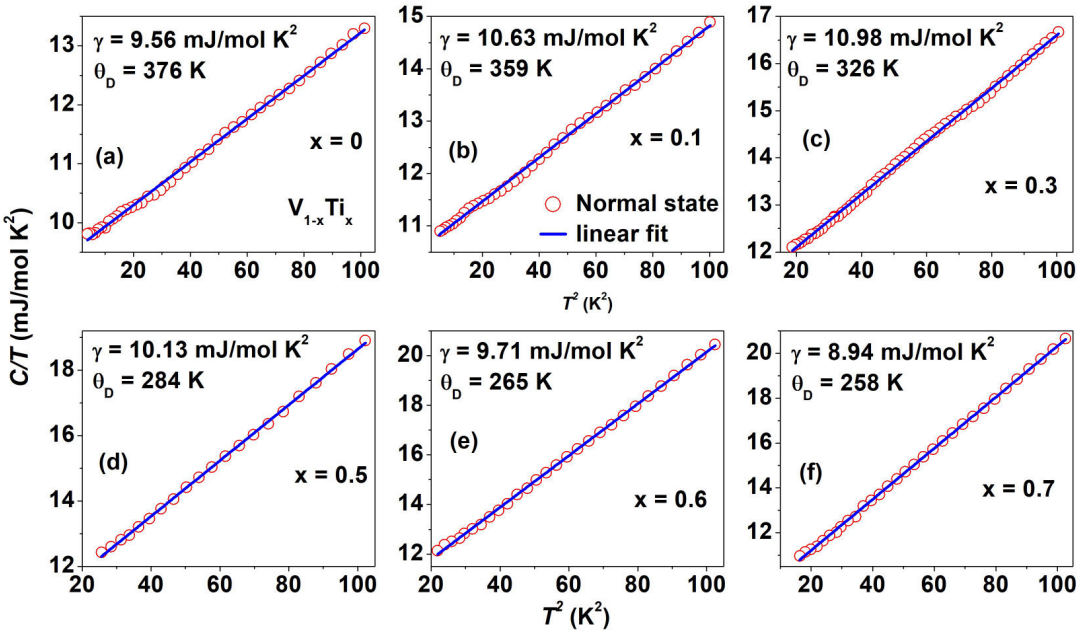

FIGURE 3.6: (a) - (f) Linear fit to the C/T vs. T^2 curves for the $V_{1-x}Ti_x$ alloys below 10 K. The open red circles are the experimental data points, whereas the blue line is the fit to the experimental data.

The normal electron density (n_e) changes when a material becomes superconducting because of the formation of Cooper pairs below the T_{sc}. As the n_e changes, electronic heat capacity also changes in the superconducting state. The phonon spectrum does not change when a material becomes superconducting and the phononic heat capacity in the superconducting state remains same as that of the normal state. Thus, the electronic heat capacity in the superconducting state (C_{es}) can be estimated by subtracting the phononic heat capacity from the total heat capacity (C_s) in the superconducting state, i.e., $C_{es} = C_s - \beta T^3$. The C_{es} is related to the superconducting energy gap as [127, 128, 129],

$$\frac{C_{es}}{\gamma T_{sc}} = \frac{6\alpha^2}{\pi^2}\frac{1}{4\pi}\frac{T_{sc}}{T}\int_0^{2\pi} d\phi \int_0^{\pi} d\theta sin\theta \int_0^{\infty} dx \left(-\frac{df}{dE}\right)\left(E^2 - \frac{T}{2}\frac{d\delta}{dT}\right), \tag{3.3}$$

here $E = x^2 + \delta^2$, $f = (1 + exp(\alpha T_{sc} E/T))^{-1}$, $\alpha = \Delta_0/k_B T_{sc}$, $\delta = \Delta(T)/\Delta_0$ and Δ_0 is the superconducting energy gap at $T \to 0$. The experimentally obtained $C_{es}/\gamma T_{sc}$ is fitted with $\Delta_0/k_B T_{sc}$ as a fitting parameter and considering the superconducting gap to be isotropic.

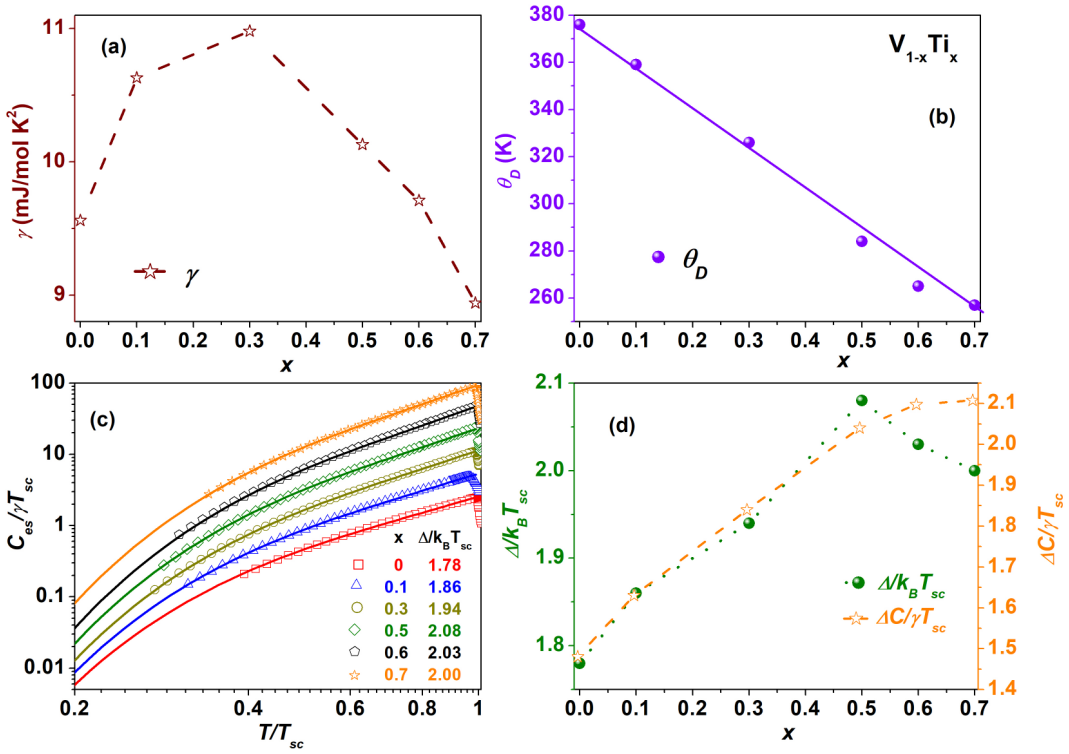

FIGURE 3.7: Variation of (a) γ and (b) θ_D as a function of Ti concentration. (c) Temperature dependence of the electronic heat capacity in the superconducting state divided by γT_{sc} ($C_{es}/\gamma T_{sc}$) as a function of normalized temperature (T/T_{sc}). The lines are fit to the experimental data. (d) Variation of $\Delta_0/k_B T_{sc}$ and $\Delta C/\gamma T_{sc}$ as a function of Ti concentration.

In such a case, Δ_0 does not explicitly depend on ϕ and θ. Therefore, the integration over ϕ and θ has been carried out independently. We have estimated the $C_{es}/\gamma T_{sc}$ and χ^2 for different values of $\Delta_0/k_B T_{sc}$ varied in steps of 0.02. The $\Delta_0/k_B T_{sc}$ was taken for which the χ^2 is minimum. The fit to $C_{es}/\gamma T_{sc}$ for different alloys are shown in figure 3.7 (c). The $C_{es}/\gamma T_{sc}$ for the alloys are shifted along the vertical axis for better visibility. A plot of $\Delta_0/k_B T_{sc}$ as a function of Ti concentration is shown on the left-hand axis of the figure 3.7 (d). The value of $\Delta_0/k_B T_{sc}$ increases from 1.78 for V to 2.08 for the $x = 0.5$ alloy and then decreases slightly with further Ti addition. This shows that the electron-phonon coupling is strong in the $V_{1-x}Ti_x$ alloys [95]. The ratio of the jump in heat capacity at T_{sc} to electronic heat capacity at T_{sc}, $\Delta C/\gamma T_{sc}$ is shown on the right-hand axis of the figure 3.7 (d). The value of $\Delta C/\gamma T_{sc}$ is higher than 1.43 in these alloys which also shows that the electron-phonon

coupling is strong in these alloys.

Role of different scattering mechanisms in limiting the thermal conductivity of $V_{1-x}Ti_x$ alloys

The metallography images of the $V_{1-x}Ti_x$ alloys are shown in the figure 3.8. The grain boundaries are marked by dashed lines (except for $x = 0.1$ alloy) for better visibility. The grain sizes of these alloys vary from few hundreds of μm to few mm. The dislocations being hot spots for acid etching, the etch pits develop at the position of dislocations. The rarity of etch pits in the images indicate that very few dislocations are present in these alloys. The phonons are scattered from a specific type of defect only if the average phonon mean free path l_l becomes of the order of the inter defect distances. The l_l in the normal state can be estimated using the formula, $l_{ln} = 3\kappa_{ln}/C_{ln}v_s$. We have mentioned earlier that more than 70% of heat is carried by electrons in the normal state of these alloys (from WF law). Thus, assuming phonons carry 30% or less amount of heat in the normal state and taking v_s = 2650 m/s [4], we found that the l_{ln} is 100 nm or less for these alloys at 10 K. In estimating l_{ln}, we have used the experimental C_{ln} obtained from the heat capacity measurements. As the phonon mean free path is much smaller than the average grain size and since very few dislocations are present in these alloys, scattering of phonons from grain boundaries and dislocations do not affect the κ_l significantly. We have previously shown that the electron-phonon interaction in the $V_{1-x}Ti_x$ alloys is strong [95], which makes the electrons the major scatterer in limiting the heat conduction by phonons. This is also supported by the observation of an increase of κ_s below T_{sc}. Again, the addition of Ti in V results in the generation of random atomic disorder, which act as point defects and scatter the phonons.

Unlike phonons, the electrons do not distinguish between various defects and gets scattered from them. On the other hand, the electron-phonon coupling being strong in these alloys, we need to consider the scattering of electrons from phonons as well. Therefore, considering the scattering of electrons from disorder and phonons and the scattering of phonons

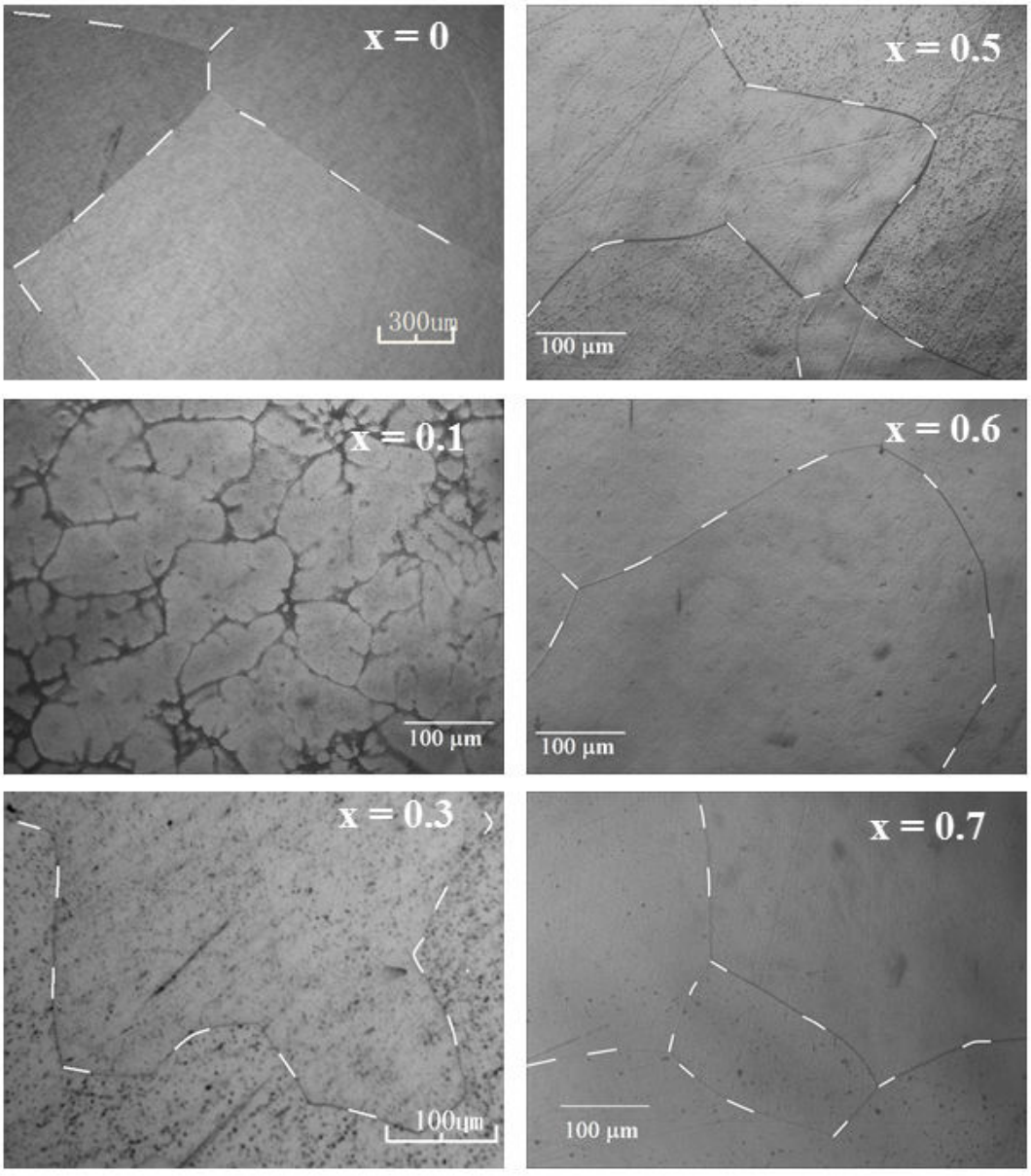

FIGURE 3.8: Metallography images of the $V_{1-x}Ti_x$ alloys.

from electrons and point defects we have analysed the normal state $\kappa(T)$ of the present alloys.

3.1.5 Normal state thermal conductivity of the $V_{1-x}Ti_x$ alloys

As we need to consider four different scattering mechanisms, we have analysed the temperature dependence of the thermal conductivity in the normal state $\kappa_n(T)$ of the $V_{1-x}Ti_x$ alloys in the T range 2 - 30 K for V and 4.5 - 50 K for the alloys with Ti. The κ_n of the $V_{1-x}Ti_x$ alloys are fitted following the procedure described below. We have mentioned in the previous section that the κ_n of these alloys are limited by the scattering of electrons from the static defects and phonons and the scattering of the phonons from electrons and point defects. Therefore, the scattering coefficients A_n, B_n, E_n/M and P_n/M were obtained as fitting parameters. The linearity of the κ_n between 2-10 K indicates that the scattering of electrons from the static defects limit the heat conduction in this temperature range. Therefore, to have an initial guess for A_n, we have used the WF law and estimated A_n using the ρ_0. We fitted the κ_n in the temperature range 2-10 K using a low temperature formula of κ_n [71], to obtain the initial guess value for the B_n. These obtained values of A_n and B_n obtained in this manner were used to obtain the κ_{en}. As the κ_n below is mostly electronic, we have estimated the κ_{en} up to 50 K and subtracted it from the κ_n to obtain κ_{ln}. The rise of the κ_s with decreasing temperature indicates that the scattering of the phonons from electrons play a major role in limiting the κ_{ln}. Therefore, we have varied the E_n/M till the estimated value of the κ_{ln} becomes close to the experimental κ_{ln}. After that, we varied the P_n/M keeping the E_n/M fixed to have an initial guess. These values of A_n, B_n, E_n/M and P_n/M were used as initial guesses to fit the experimental κ_n. To fit the κ_n, it was necessary to numerically evaluate different integrals. To optimize the error in integration, we varied both the limits and step size of the integration till the error of the integration (taken as the difference between two successive integration with different step size or limit) remain below 10^{-5}. Then, a least square error minimizing routine based on the Levenberg-Marquardt algorithm was used to fit the experimental data. The convergence criterion for the reduced chi-square was

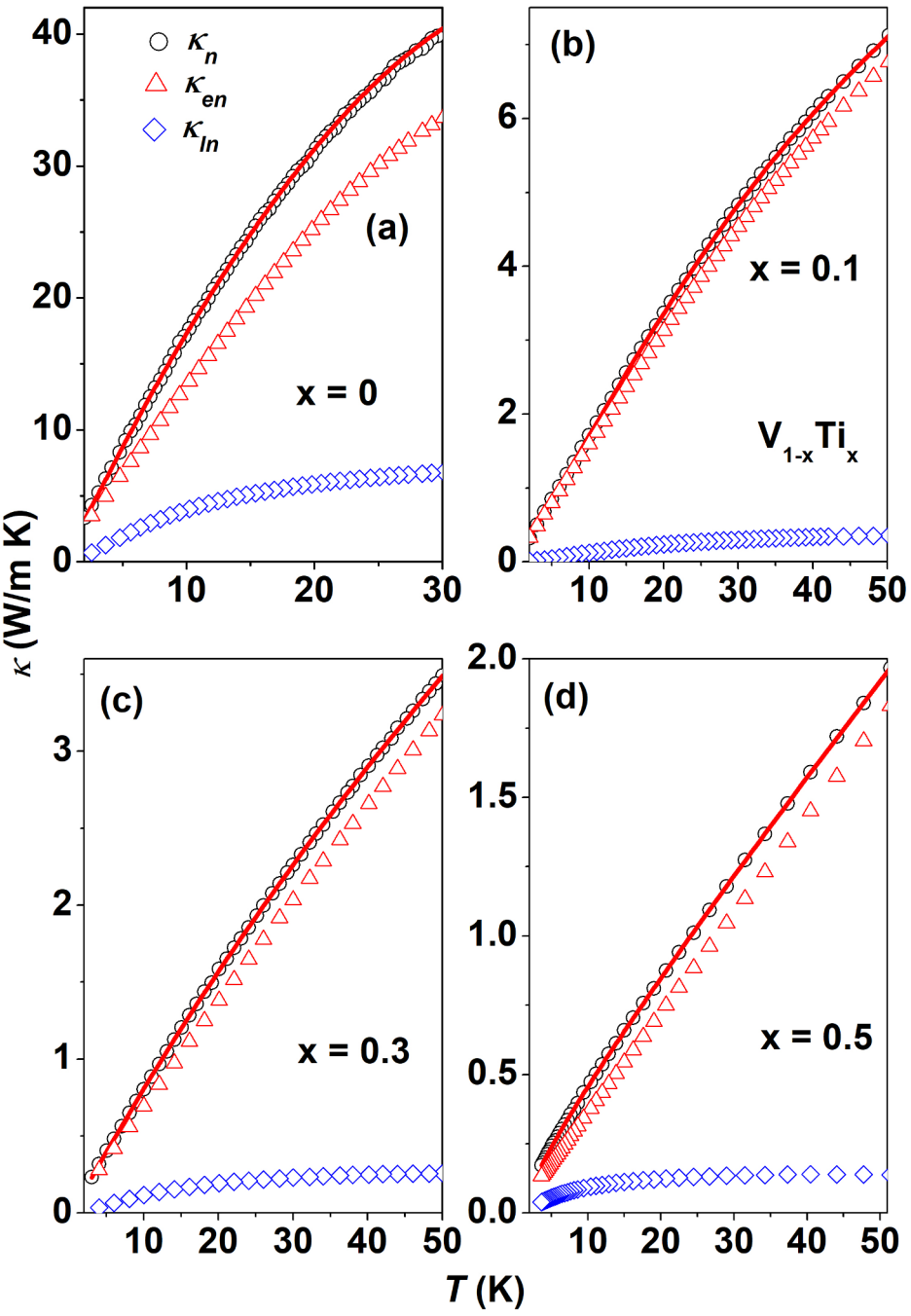

FIGURE 3.9: Temperature dependence of the normal state thermal conductivities with the electronic and phononic parts separated for (a) $x = 0$, (b) $x = 0.1$, (c) $x = 0.3$, (d) $x = 0.5$ respectively. Electrons carry the majority of the heat in the normal state of these alloys.

set to 10^{-4}. After obtaining the initial set of parameters from the fitting, the convergence was further checked by changing the initial guess values repeatedly. The fitting parameters obtained are listed in table 3.2a. Figure 3.9 shows the $\kappa_n(T)$ of the $V_{1-x}Ti_x$ alloys with the electronic (κ_{en}) and phononic (κ_{ln}) contribution separated out. The black circles in figure 3.9 show the experimental $\kappa_n(T)$ and the red line is the fit to the same using equations 1.11, 1.12 and 1.21 (see section 1.5 in chapter 1 for the details).

The red triangle and blue diamond symbols are respectively $\kappa_{en}(T)$ and $\kappa_{ln}(T)$ of these alloys. We see that electrons indeed carry more than 70% of heat in the normal state of these alloys, although l_e approaches the Mott-Ioffe-Regal (MIR) limit. This is commensurate with the κ_{en} estimated using the WF law. The phonons are found to be less effective in limiting the heat flow by electrons. However, the experimental data can not be fitted if this term is ignored. We found that the static defects are the major scatterers of electrons limiting the κ_{en}. In such a case, where the scattering of electrons from phonons does not affect the heat conduction, κ_{en} is given by, $\kappa_{en} = \frac{1}{3}C_e v_F l_e = (k_B^2/9\hbar)T(3\pi^2 n_e)^{2/3} l_e$. Thus, for pure metals, with the reduction of temperature below T_{sc}, the κ_{es} reduces due to the reduction in n_e but κ_{es} still continues to dominate over κ_{ls} due to the large value of l_e. When the materials go to the MIR limit, κ_{en} has the least possible value and the electrons still carry 70% of heat in the normal state of the $V_{1-x}Ti_x$ alloys due to very large free electron density and the high mobility of the electrons.

3.1.6 Superconducting state thermal conductivity of the $V_{1-x}Ti_x$ alloys

Figure 3.10 shows the results of analysis of $\kappa_s(T)$ of the $V_{1-x}Ti_x$ alloys in the temperature range 2 K to T_{sc}. The κ_s of these alloys has been analysed using equations 1.23, 1.25 and 1.28 mentioned in chapter 1. The solid and open black circles represent the experimentally obtained κ_n and κ_s, respectively. The κ_{es} of these alloys are estimated as, $\kappa_{es} = \kappa_{es,i}^{-1} + \kappa_{es,l}^{-1}$. Here, $\kappa_{es,i}$ and $\kappa_{es,l}$ are respectively the electronic thermal conductivity in the superconducting state limited by scattering of electrons from disorder and phonons. The κ_{ls} is obtained

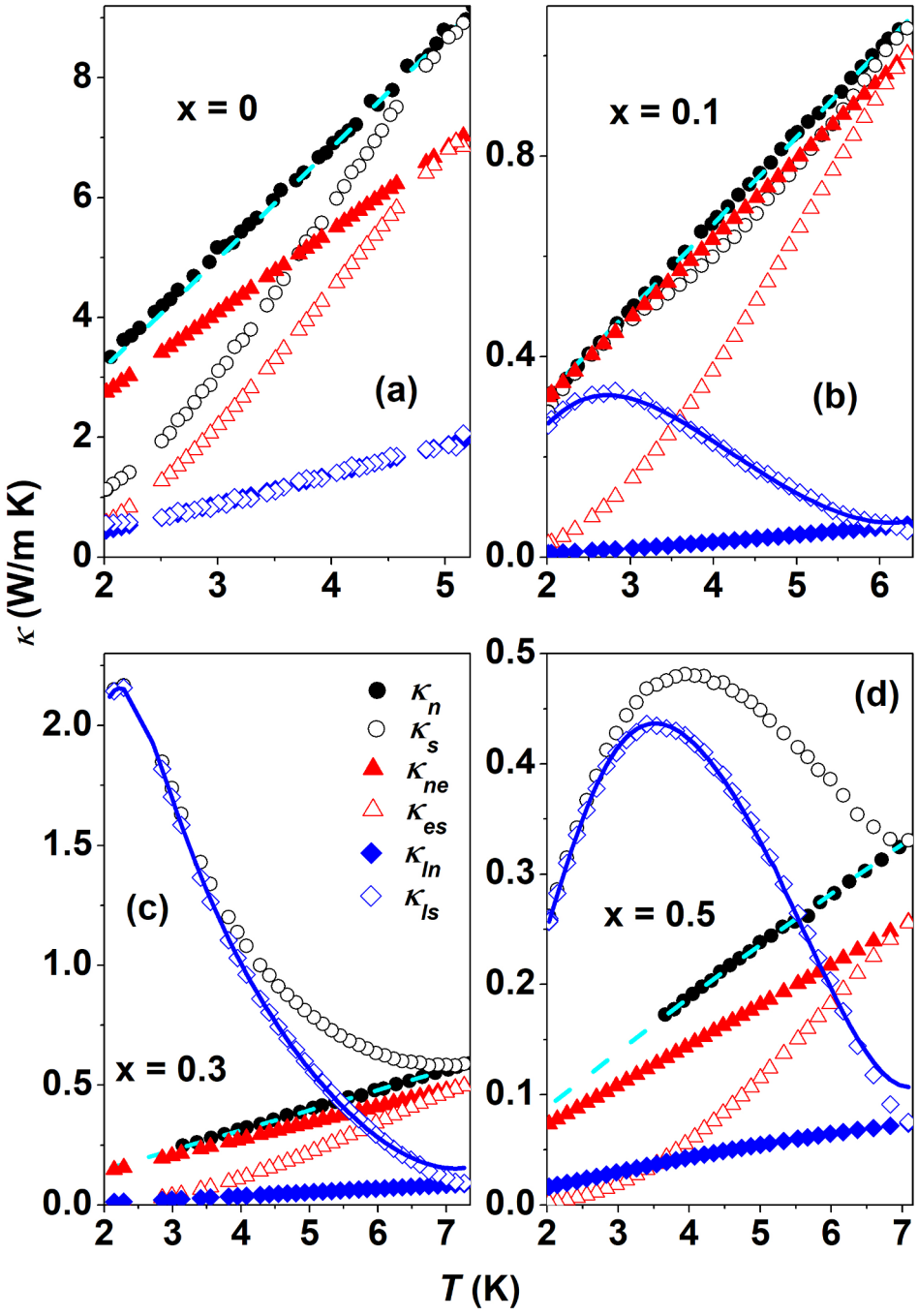

FIGURE 3.10: Temperature dependence of the superconducting state thermal conductivities with the electronic and phononic parts separated for (a) $x = 0$, (b) $x = 0.1$, (c) $x = 0.3$, (d) $x = 0.5$ respectively. Phonons carry majority of heat in the normal state of these alloys.

by subtracting the κ_{es} from κ_s. The open red triangle and the open blue diamond symbols show the κ_{es} and κ_{ls} of the alloys, whereas the solid red triangle and the solid blue diamond symbols show the κ_{en} and κ_{ln}. The dashed line in cyan colour shows fit to the κ_n of these alloys and the blue solid line shows fit to κ_{ls}. The κ_{ls} of these alloys are fitted using a least square error minimization procedure as described in earlier section. The κ_s of V shows a behaviour similar to other metallic superconductors like Nb [70, 71]. The κ_s for V lies below κ_n for the temperature range $T_{sc}/2 < T < T_{sc}$. The κ_{ls} is lower than κ_{es} for $T \geq 2$ K and the temperature dependence of κ_s follows the temperature dependence of κ_{es}. The κ_{ls} and κ_{ln} are almost the same for V for temperatures below T_{sc} except around 2 K, where κ_{ls} shows a slight upturn. This is also evident from the value of the fitting parameter E/M (table 3.2a), which is about an order of magnitude lower for V in comparison with the alloys with Ti. Thus V is a perfect example of a system where the electrons dominate heat conduction in both the normal and superconducting states. The κ_{ls} of the $x = 0.1$ alloy start to rise with the reduction of temperature below T_{sc} (= 6.4 K). The crossover between κ_{es} and κ_{ls} is observed at $T = 3.4$ K, which is higher than $T_{sc}/2$. For the alloys with $x > 0.1$, The crossover between κ_{es} and κ_{ls} is observed very close to the T_{sc}.

The relaxation time of phonons corresponding to the scattering from point defects vary as $\propto \omega^4$. Thus, the point defects effectively scatter the high frequency phonons. This leaves a large portion of the heat to be carried by the low-frequency phonons. As the electron-phonon coupling in the $V_{1-x}Ti_x$ alloys is strong, these low frequency phonons are scattered only by the electrons in the normal state. So, when the material becomes superconducting, the loss of normal electrons enhances the κ_{ls} significantly. When the temperature is reduced further, with the reduction in scattering of phonons from electrons, the effective phonon mean free path (l_{ph}) increases and approaches the inter-dislocation distances. Thus, the scattering of phonons from the dislocations lead to the reduction of κ_{ls} with decreasing T. These results show that the $V_{1-x}Ti_x$ alloys are a rare example of a metallic system where electrons carry

the majority of heat in the normal state, but phonons carry the majority of heat in the superconducting state. The enhancement of κ with the reduction of T below T_{sc} is also observed in the heavy fermion superconductor $CeCoIn_5$ [130]. In the case of $CeCoIn_5$, the sample was a good quality single crystal free from the grain boundaries and dislocations. This led to the loss of electrons below T_{sc} and to the rise of κ_s. Thus the rise of κ_s is observed in the systems, where scattering of phonons from grain boundaries and dislocations are negligible.

TABLE 3.2: Parameters obtained from the fitting of (a) $\kappa_n(T)$ and (b) $\kappa_{ls}(T)$. The variation in the values of the parameters satisfying the convergence criterion was within 2%.

(A) **Normal state**

x	A_n (m K^2 W^{-1})	B_n (m K^{-1} W^{-1})	E_n/M (m K^3 W^{-1})	P_n/M (m W^{-1})
0	0.7443	3.8466×10^{-6}	58.2273	0.0063
0.1	6.2795	7.8635×10^{-6}	3683.3	0.0651
0.3	14.3506	8.74039×10^{-6}	2835.4	0.1362
0.5	27.4028	6.9182×10^{-6}	1516.9	0.5303
0.6	32.1086	0	657.05	3.183

(B) **Superconducting state**

x	E_s/M (m K^3 W^{-1})	L_s/M (m K^3 W^{-1})	P_n/M (m W^{-1})
0.1	3899.7	87.2577	0.0125
0.3	2595.6	10.5179	0.00123
0.5	2834.7	101.7091	0.01427
0.6	5188.2	240.9905	0.03126

The thermal resistivity coefficients obtained by fitting the κ_n and the κ_{ls} with the equations 1.12, 1.21and 1.28 are listed in table 3.2a and table 3.2b respectively. The variation in the values of the parameters satisfying the convergence criterion was within 2%. We have not fitted the κ_{ls} for the $x = 0$ alloy as there is no difference in the κ_l between the normal and superconducting states. The coefficient B_n (which is due to the scattering of electrons from phonons) is much smaller than the A_n (due to the scattering of electrons from defects). For the details on A_n and B_n see equations 1.13 and 1.15 in section 1.5 of chapter 1. The coefficient A_n increases almost linearly with increasing Ti content, as disorder increases in the system with the addition of Ti. This is also evident from the increase of ρ_0 with the addition

of Ti (see table 3.1 for details). The majority of these defects are the point defects generated due to the addition of Ti in V. This increase in point defect increases the resistance to the heat flow. However, strong electron-phonon coupling is persistent throughout the composition range due to lattice softening with the addition of Ti in V. This leads to the increase of E_n/M by two orders of magnitude when 10% of Ti is added in V. The E_n/M decreases significantly at large values of x due to the reduction of electron-phonon coupling and the incipient instability of the lattice. The thermal resistivity coefficient due to the scattering of phonons from the point defects (P_n/M) increases with the increasing Ti content due to the point defects created with the addition of Ti.

In the superconducting state, E_s/M for all the alloys containing Ti remain almost constant and has a large value as κ_{ls} is hardly affected by the scattering of phonons from electrons. However, in the superconducting state, P_s/M reduces by an order of magnitude due to the re-normalization of the l_{ph}. This re-normalization makes the dislocations effective scatterrers in the superconducting state.

3.2 Summary

We have analysed in detail the $\rho(T)$, $C(T)$ and $\kappa(T)$ behaviour of the $V_{1-x}TI_x$ alloys. The TCR of these alloys goes from positive for the $x = 0.6$ alloy to negative for $x = 0.7$. Our analysis shows that this change in TCR is due to the reduction of l_e below the inter-atomic distances, leading the system to the Mott-Ioffe-Regal limit [101]. From our analysis of $C(T)$ we find that the electron-phonon coupling in these alloys is strong. The $\kappa_s(T)$ in some of these alloys rises as T decreases below T_{sc}. We show that this rise of κ_s in a metallic crystalline system with high electron density like the $V_{1-x}Ti_x$ alloys requires a large number of point defects to be present in the system. When present in very large number, the point defects reduce the l_e to inter atomic distances, limiting the κ_e to a minimum. In the case of phonons, the point defects scatter the high frequency phonons incoherently, leaving the heat conduction to the low frequency phonons only. In the absence of scattering of phonons

from dislocations and grain boundaries, the κ_l is limited only by the scattering of phonons from the electrons at low temperatures. When the material becomes superconducting, the scattering of phonons from the electrons reduces due to the formation of Cooper pairs. This leads to the rise of $\kappa(T)$ in the superconducting state. It is worthwhile to note that this rise of the $\kappa(T)$ in the superconducting state provides an opportunity to increase the J_c of these alloys as well, through the process of introducing additional defects.

Chapter 4

Enhancement of the critical current density of the $V_{0.60}Ti_{0.40}$ alloy with the addition of Gd

In the previous chapter in figure 3.10, we have seen that close to 0.5 T_{sc}, the thermal conductivity of some of the $V_{1-x}Ti_x$ alloys is 2 to 4 times higher than that at T_{sc} [131], which gives the opportunity to introduce further disorder in the system. The introduction of disorder might enhance the J_c of the alloys. Previously, Matin *et al.* studied the J_c and the pinning force density (F_p) of the $V_{1-x}Ti_x$ alloys in detail [6, 7]. Their studies reveal that though the grain boundaries (GB) provide the strongest pinning mechanism in this alloy system, the GB density is rather low as compared to the commercial Nb_3Sn and Nb-Ti superconductors. The average grain size of the as-cast Ti-V alloys vary from hundreds of microns to a few mm [6, 7, 131], whereas the grain size of the Nb_3Sn and Nb-Ti superconductors are in the range of few tens to few hundreds of nm [40, 132]. Point defects are also effective in pinning the flux lines in the $V_{1-x}Ti_x$ alloys, but only for high magnetic fields close to the irreversibility field (H_{irr}) [6, 7]. Grain refinement can be an effective method for enhancing the J_c of the Ti-V alloys. The rare earth (RE) elements have been extensively used for grain refinement in various steel and high entropy alloys, where the RE elements mostly get segregated along the GB [76, 77, 78, 79]. Since, the RE elements are immiscible in the *bcc* transition metals

[133] due to their low melting temperature and higher ionic radius, introducing a RE element into the β-phase $V_{1-x}Ti_x$ alloys may be an effective method of enhancing the J_c. This is because of the fact that the immiscible RE element might reduce the grain size and also generate additional point defects. Campbell and Evetts have shown that the magnetic inclusions are more effective in pinning the flux lines as compared to normal metallic inclusions or normal point defects [134]. Accordingly, we have introduced Gd in the $V_{0.60}Ti_{0.40}$ alloy. In this chapter, we discuss the effect of Gd addition on the J_c and F_P of the $V_{0.60}Ti_{0.40}$ alloy. The as-cast $V_{0.60-x}Ti_{0.40}Gd_x$ ($x = 0$, 0.005, 0.01 and 0.02) alloys are studied with the help of the XRD, metallography, $\rho(T)$, $M(T)$ and $M(H)$ measurements.

4.1 Results and discussion

4.1.1 Characterization of the $V_{0.60-x}Ti_{0.40}Gd_x$ alloys

Figure 4.1 shows the XRD patterns of the $V_{0.60}Ti_{0.40}$ alloys after the addition of Gd. The XRD measurements are performed using λ = 0.83019 Å radiation from BL12 beamline of the Indus-2 synchrotron facility at the Raja Ramanna Centre for Advanced Technology, Indore [135]. The XRD data from the samples are shifted vertically for better visibility. Distinct peaks corresponding to reflections from *bcc* $V_{0.60}Ti_{0.40}$ (indexed in figure 4.1 (a)) and hexagonal closed packed (*hcp*) Gd phases (indexed in figure 4.1 (b)) are seen in the samples containing Gd. The positions of the peaks corresponding to the $V_{0.60}Ti_{0.40}$ alloy does not shift with the increasing Gd content in the alloys. This indicates that the *hcp*-Gd is immiscible in $V_{0.60}Ti_{0.40}$ alloys. The lattice parameter of *bcc*-$V_{0.60}Ti_{0.40}$ phase is 3.13 Å which is in agreement with that reported in literature [7, 93, 94]. The lattice parameters of Gd precipitates are observed to be a = 3.636 Å and c = 5.783 Å which is similar to that reported for the bulk Gd [136]. Few peaks with lower intensities and shifted positions corresponding to reflections from *hcp*-Gd were also observed. This indicates that there is a distribution of size among the Gd clusters.

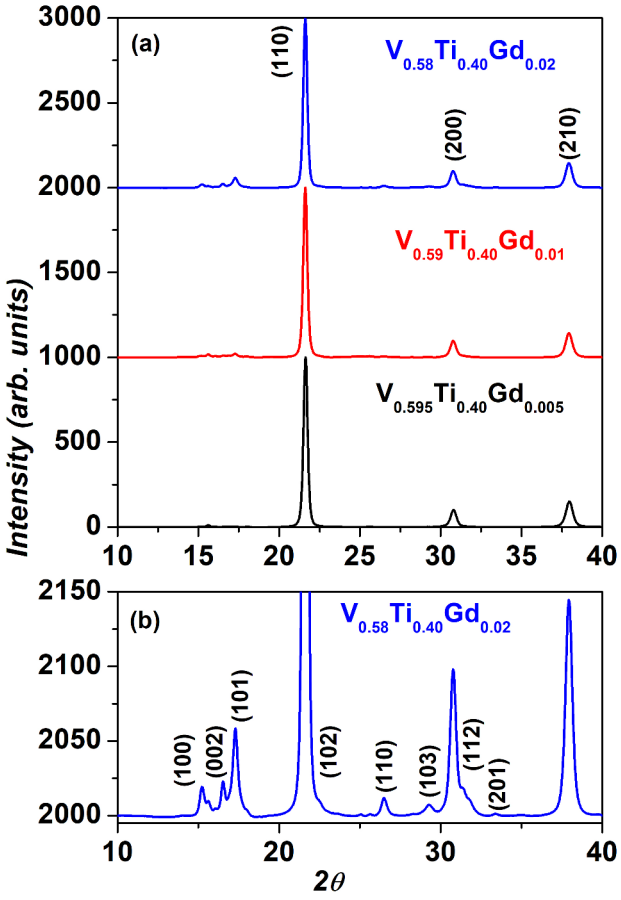

FIGURE 4.1: (a) X-ray diffraction patterns of the $V_{0.60}Ti_{0.40}$ alloys with the addition of Gd, which is immiscible in $V_{0.60}Ti_{0.40}$. (b) The reflections corresponding to *hcp*-Gd in the $V_{0.58}Ti_{0.40}Gd_{0.02}$ alloy.

The metallography images of the $V_{0.60-x}Ti_{0.40}Gd_x$ alloys are shown in the figure 4.2. The average grain size of the $V_{0.60}Ti_{0.40}$ alloy is ~ 250 μm. The grain size reduces with the addition of Gd. For the $x = 0.02$ alloy, the average grain size is ~ 20 μms. From the scanning electron microscopy and energy dispersive x-ray analysis, we observed the Gd to be distributed only in the clusters along the grain boundaries. The size of the clusters are $<$ 1.5 μm. The formation of closed pattern by the clusters indicates that Gd is distributed along the grain boundaries. The inset to figure 4.2 (d) shows an enlarged metallography image of the $x = 0.02$ alloy. The regions marked by '+' inside the circles contain Gd. No trace of Gd is observed inside the grains (regions marked by the cyan box in the inset to figure 4.2 (d)).

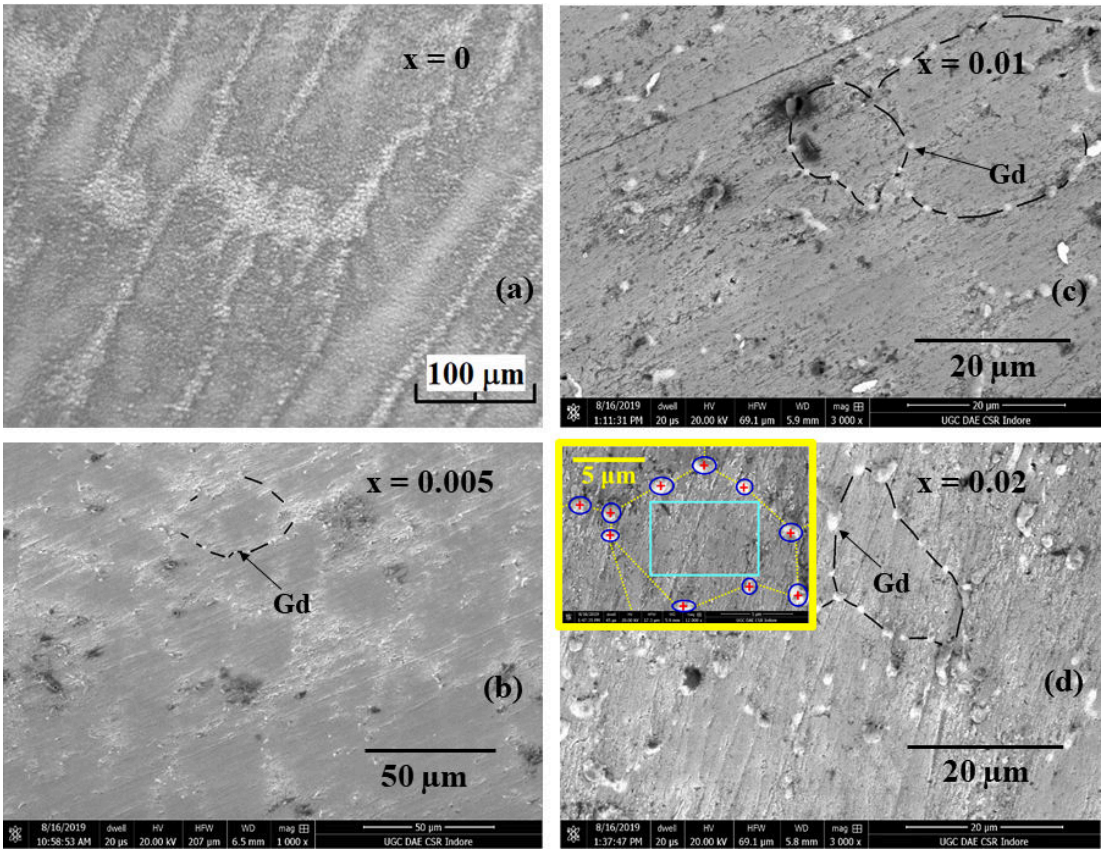

FIGURE 4.2: (a) - (d) Metallography images of the $V_{0.60-x}Ti_{0.40}Gd_x$ alloys. Inset to (d) Scanning electron microscopy images of the $V_{0.58}Ti_{0.40}Gd_{0.02}$ alloy. Gd precipitates along the grain boundaries (marked by the black dotted lines) with a size of about 1-5 μm (marked '+'). No trace of Gd is observed inside the grains.

4.1.2 Temperature dependence of resistivity of the $V_{0.60-x}Ti_{0.40}Gd_x$ alloys

Figure 4.3 (a) shows the $\rho(T)$ curves for the $V_{0.60-x}Ti_{0.40}Gd_x$ alloys in the temperature range 2 - 300 K in the absence of any applied magnetic field. The residual resistivity (ρ_0) of x = 0.005 alloy is slightly higher than that of the x = 0 alloy. The ρ_0 decreases with further increasing x. Although ρ_0 decreases for the alloys with $x \geq 0.01$, the $\rho(T)$ of the $V_{0.60}Ti_{0.40}$ alloy above 200 K is lower than that of the $x > 0$ alloys. Figure 4.3 (b) shows that the reduction of ρ_0 of the present alloys is larger than the variation of ρ_0 of the V_yTi_{1-y} alloys, which indicates that the changes in ρ_0 are not due to the changes in the relative amounts of

V and Ti.

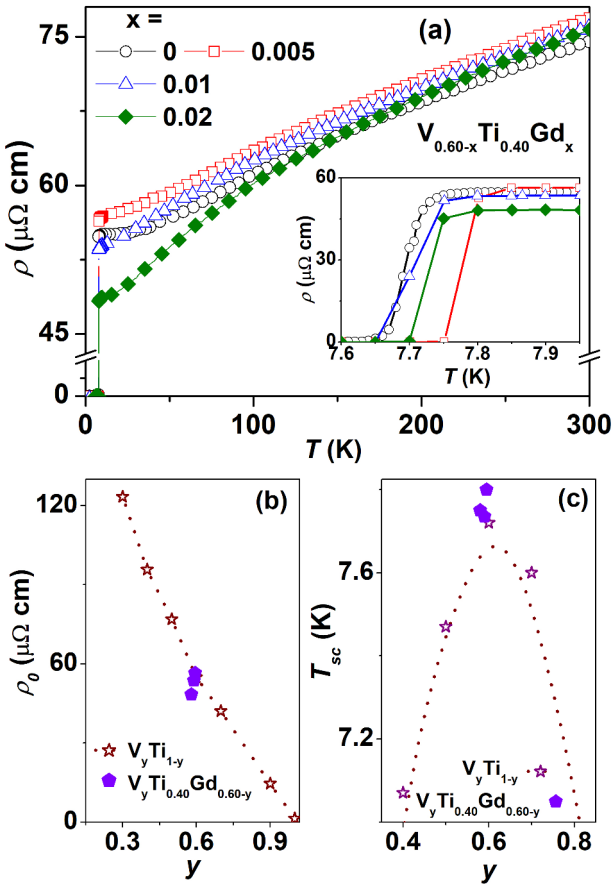

FIGURE 4.3: (a) $\rho(T)$ of $V_{0.60-x}Ti_{0.40}Gd_x$ alloys in the range 2 - 300 K. The $\rho(T)$ at $T < 100$ K decreases with increasing $x > 0.005$. (Inset) Expanded view of $\rho(T)$ around T_{sc} indicates that $T_{sc}(x > 0) > T_{sc}(x = 0)$. The ρ_0 and T_{sc} of the V_yTi_{1-y} and $V_{0.60-x}Ti_{0.40}Gd_x$ alloys as a function of V concentration are shown in (b) and (c) respectively. The comparison of ρ_0 of the V_yTi_{1-y} and $V_{0.60-x}Ti_{0.40}Gd_x$ alloys shows that the ρ_0 of the $V_{0.60-x}Ti_{0.40}Gd_x$ alloys are lower than that expected for the alloys containing similar amount of V. The T_{sc} of $V_{0.60}Ti_{0.40}$ is highest among the V_yTi_{1-y} alloys. Thus, the increase in the T_{sc} with the addition of Gd is not due to change in the V content.

The increased GB density should have resulted in the increase of ρ_0, which is contrary to what is observed experimentally. The variation of $\rho(T)$ around the T_{sc} of the $V_{0.60-x}Ti_{0.40}Gd_x$ alloys is shown in the inset to figure 4.3 (a). The T_{sc} of the $x = 0$ alloy is 7.69 K, which increases slightly with the addition of Gd. Figure 4.3 (c) shows that the T_{sc} of the $V_{0.60}Ti_{0.40}$ alloy is the highest among the V_yTi_{1-y} alloys. The $V_{0.60-x}Ti_{0.40}Gd_x$ alloys have T_{sc} higher

than that of the $x = 0$ alloy indicating that this variation is not due to the amount of V and Ti present in the samples. The ρ_0 and T_{sc} of these alloys are listed in table 4.1.

TABLE 4.1: Variation of ρ_0 and T_{sc} with Gd content in the $V_{0.60-x}Ti_{0.40}Gd_x$ alloys

x	ρ_0 $\mu\Omega$ cm	T_{sc} (K) (resistivity)	T_{sc} (K) (magnetization)
0	54.90±0.40	7.69±0.01	7.55 ±0.05
0.005	56.67±0.03	7.78±0.03	7.75±0.05
0.01	53.64±0.12	7.71±0.05	7.70±0.05
0.02	48.20±0.09	7.73±0.03	7.70±0.05

4.1.3 Temperature and field dependence of magnetization of the $V_{0.60-x}Ti_{0.40}Gd_x$ alloys

The $M(T)$ curves of the $V_{0.60-x}Ti_{0.40}Gd_x$ alloys are shown in figures 4.4 (a) - (d) in the temperature range 2 - 8 K measured in the presence of 10 mT magnetic field. The $M(T)$ of these alloys are measured in ZFC, FCC and FCW measurement protocols. The details of the measurement procedures have been discussed in chapter 2. A large decrease in $M(T)$ at 7.55 K for the $x = 0$ alloy indicates the normal to superconducting phase transition in this alloy. The T_{sc}s obtained from the $M(T)$ measurements are in line with our $\rho(T)$ results. Large difference in $M(T)$ between ZFC and FCC/FCW cycles indicates the presence of strong flux pinning in these alloys. The insets to figures 4.4 (b) - (d) show the $M(T)$ in the temperature range 250 - 300 K. All the alloys containing Gd show features similar to that of a paramagnetic to ferromagnetic transition at 295 K, which corresponds to that of bulk Gd [137].

Figure 4.5 shows the isothermal field dependence ($M(H)$) of the $V_{0.60-x}Ti_{0.40}Gd_x$ alloys at 2 K and 4 K for $x =$ (a) 0, (b) 0.005, (c) 0.01 and (d) 0.02. The $M(H)$ curves at temperatures below T_{sc} of these alloys exhibit irreversible magnetization. For the $x = 0$ alloy,

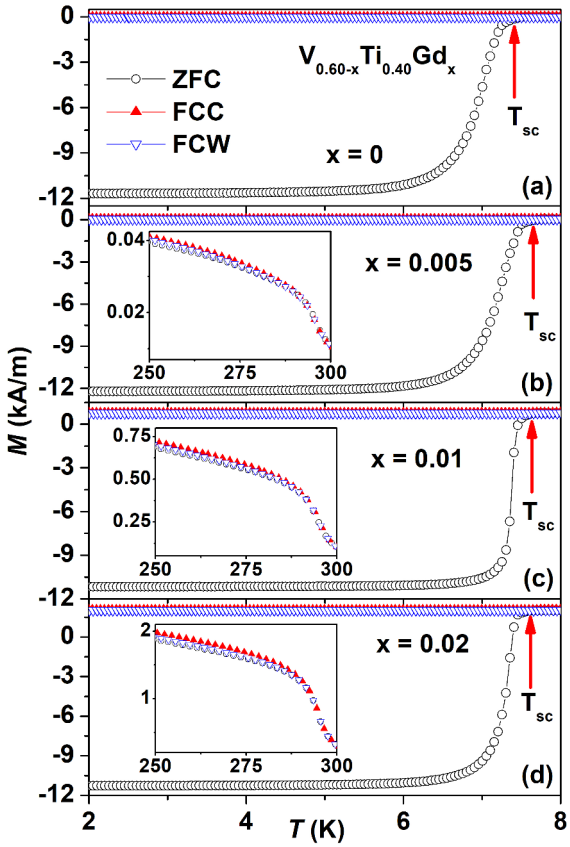

FIGURE 4.4: Temperature dependence of magnetization of the $V_{0.60-x}Ti_{0.40}Gd_x$ alloys.

the field hysteresis (ΔM) at 2 K reduces sharply with increasing magnetic field. The ΔM for a given magnetic field increases with the addition of Gd. For the alloy with 1 at.% Gd, the ΔM is maximum and a substantial hysteresis is observed even in 7 T applied field. The asymmetry in the isothermal $M(H)$ curves also increases with the increasing Gd content. Similar type of asymmetry was observed in (Ce,Gd)Ru_2 pseudo-binary alloys, where such asymmetry is observed to be increasing with the increasing Gd content [138]. However, to check if the asymmetry in the $M(H)$ curves below T_{sc} is due to the magnetic moments of Gd, we subtracted the $M(H)$ at temperatures just above the T_{sc} from the $M(H)$ below T_{sc} of the alloys containing Gd. Since the $V_{1-x}Ti_x$ alloys are paramagnetic above T_{sc}, the saturation in the $M(H)$ must be due to Gd. No asymmetry in the $M(H)$ was observed after the subtraction. This shows that the asymmetry in the $M(H)$ of the $V_{0.60-x}Ti_{0.40}Gd_x$ alloys

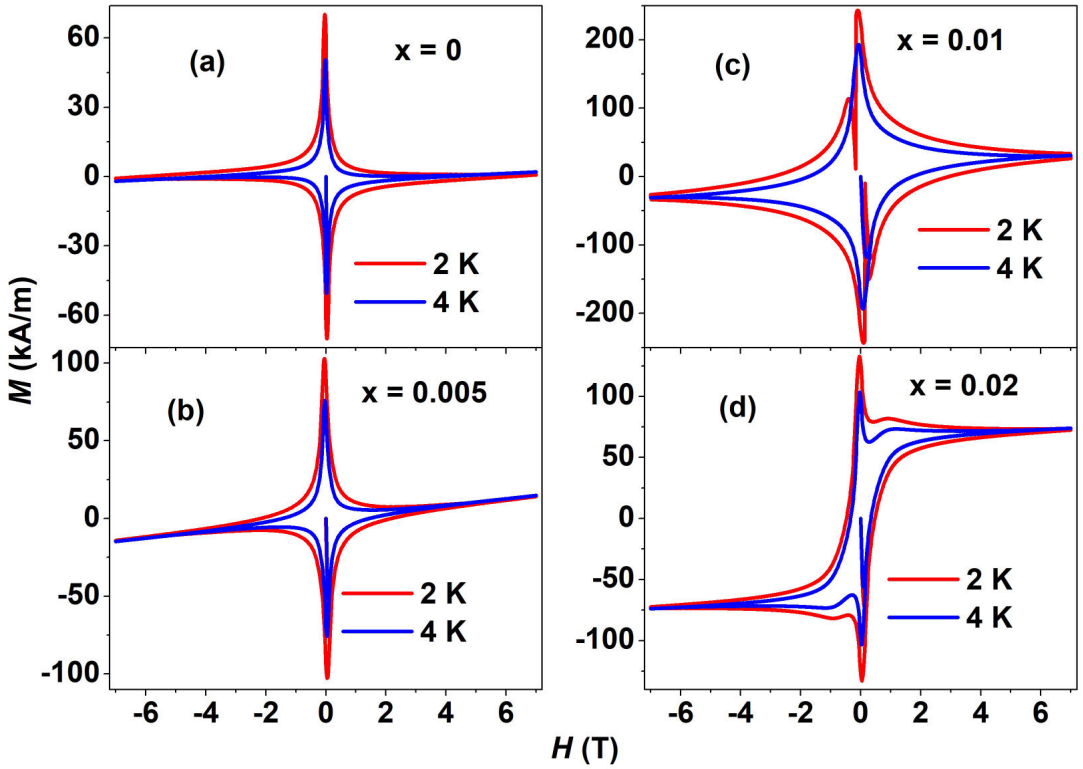

FIGURE 4.5: Field dependence of magnetization of the $V_{0.60-x}Ti_{0.40}Gd_x$ alloys.

is indeed due to the superposition of the hysteresis in $M(H)$ due to flux-line pinning in the type-II superconducting state and the ferromagnetism of Gd.

4.1.4 Magnetic field dependence of critical current density and pinning force density of the $V_{0.60-x}Ti_{0.40}Gd_x$ alloys

The J_c of a material can be estimated from the isothermal $M(H)$ curves of a superconductor using Bean's critical state model [29, 30]. According to this model, the J_c of a rectangular sample can be estimated as [52, 127],

$$J_c = \frac{2\Delta M}{\left[a\left(1-\frac{a}{3b}\right)\right]}, \tag{4.1}$$

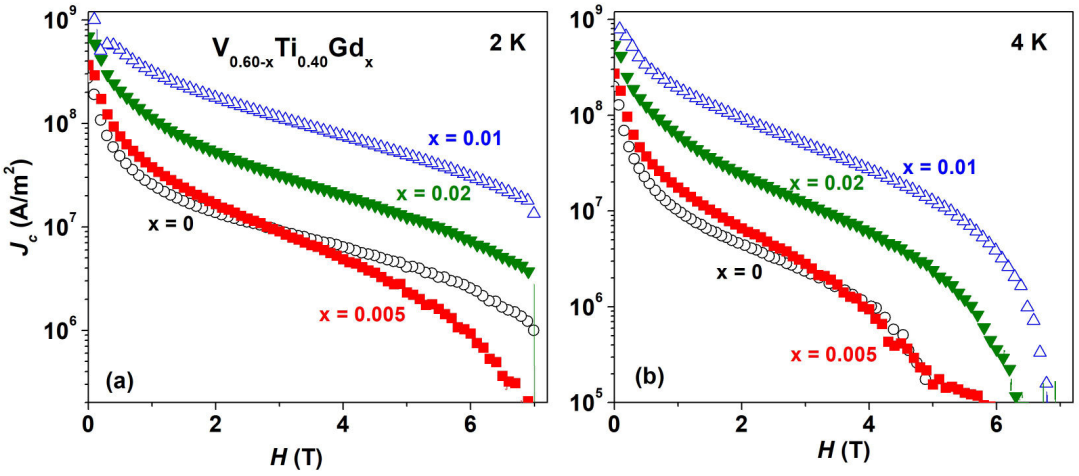

FIGURE 4.6: Field dependence of the critical current density of the $V_{0.60-x}Ti_{0.40}Gd_x$ alloys.

here, a and b are the dimensions of the sample perpendicular to H with $a < b$. The $J_c(H)$ of these alloys estimated using equation 4.1 are shown in figure 4.6 at (a) 2 K and (b) 4 K respectively. The J_c for a given applied H increases with the addition of Gd in the $V_{0.60}Ti_{0.40}$ alloy. The enhancement of J_c is maximum for the alloy with 1 at. % Gd, where the J_c is more than an order of magnitude higher than the parent alloy throughout the applied field range. After this enhancement, the J_c of the $V_{0.60-x}Ti_{0.40}Gd_x$ alloys are only about an order of magnitude lower than the modern Nb-Ti superconductors [37]. For the $x = 0.02$ alloys the $J_c(H)$ reduce slightly in comparison with the $x = 0.01$ alloy.

To have an idea about how the J_c of these alloys change with the average grain size, we show in figure 4.7 the J_c at 4 K (measured in the presence of an 1 T magnetic field) as a function of the average grain size. The samples used for the measurements were of similar size e.g., approximately 2 mm in length and $\sim$ 1 mm$\times$1 mm in cross-section. The longer axis is kept along the field-direction during the measurements. Big-size samples are not measured in the magnetometers we use. However, we have seen that different pieces of samples of slightly different size of the same alloy composition give the same J_c vs. H curves at identical temperatures. The J_c increases with the reduction in grain size upto the alloy with $x = 0.01$. However, the J_c of the $x = 0.02$ alloys decreases slightly even with

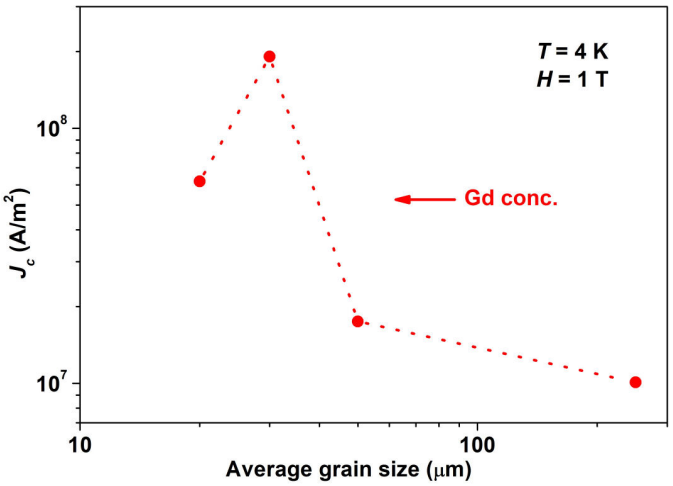

FIGURE 4.7: Critical current density of the $V_{0.60-x}Ti_{0.40}Gd_x$ alloys as a function of the average grain size at 4 K measured in the presence of an 1 T magnetic field.

the decrease in the grain size. This is possibly due to the presence of stronger ferromagnetic order (details are discussed in chapter 5) in the alloy with 2 at.% Gd.

Our analysis of the pinning force density of the $V_{1-x}Ti_x$ alloys reveal that the major pinning centres in these alloys are the grain boundaries [6]. However, the J_c estimated from the magnetization measurements are expected to have contributions from both local and global current densities [139]. For a better understanding of the nature of the pinning we need to analyse both the magnetic and transport J_c of these alloys [140]. While our magnetization measurements are mostly done in cryogen free set-up, the measurement of transport J_c in our laboratory needs a large supply liquid He and of these measurements are yet to be done. However, in view of available literature, we expect the transport J_c to be higher than the magnetization J_c [141, 142].

Figure 4.8 (a) shows the field dependence of the pinning force density ($F_P(H)$) of the $V_{0.60-x}Ti_{0.40}Gd_x$ alloys at 4 K. We see that the F_P is also enhanced by more than an order of magnitude for the alloy with 1 at. % Gd in comparison with the $V_{0.60}Ti_{0.40}$ alloy. As the superconducting magnets work at boiling He temperatures, we have presented here our results at 4 K. The $F_P(H)$ behaviour of a superconductor can be understood using the Dew

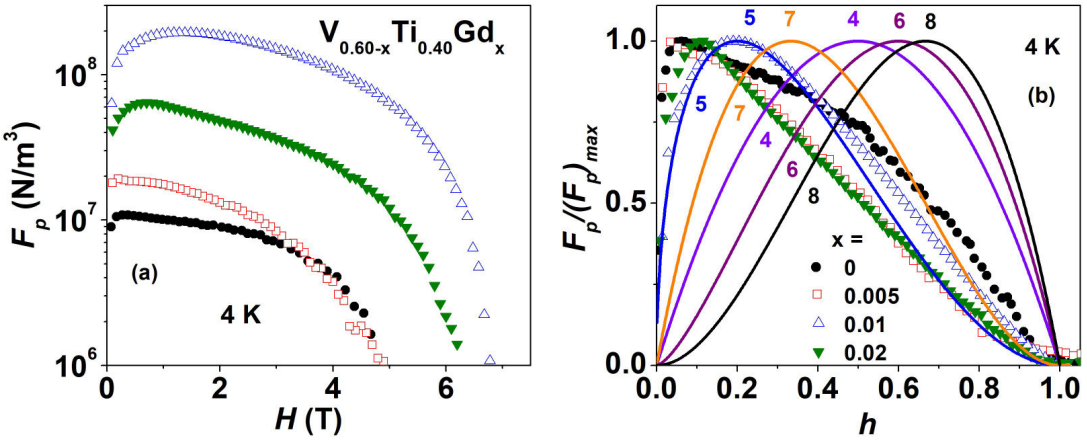

FIGURE 4.8: (a) Field dependence of the pinning force density of the $V_{0.60-x}Ti_{0.40}Gd_x$ alloys. (b) Normalized pinning force density as a function of the reduced field ($h = H/H_{irr}$).

Hughes' model of flux pinning [31] (details given in chapter 1). According to this theory, the normalized pinning force density ($f_P = F_P/(F_P)_{max}$) follows the relation [31], $f_P = h^p(1-h)^q$, here $h = H/H_{c2}$ and the specific type of the pinning mechanism present in the system determines the value of the coefficients p and q. For the $V_{0.60-x}Ti_{0.40}Gd_x$ alloys, the irreversibility field (H_{irr}) is lower than the H_{c2}. In such a case, the h is defined as, $h = H/H_{irr}$. As discussed in chapter 1, the $f_P(h)$ curves for a given pinning mechanism exhibit a single peak structure. Therefore, the multiple shoulder structure of the curves in figure 4.8 (a) indicates the presence of more than one flux line pinning mechanisms in these alloys. Figure 4.8 (b) shows the plot of experimental f_P as a function of h along with the relevant theoretical lines from Dew Hughes' model. The details of the different types of pinning mechanisms and normalized pinning force density corresponding to these curves are discussed in chapter 1. The lines 5, 6 and 8 in figure 4.8 (b) are respectively due to the pinning of the flux lines at the grain boundaries, dislocations and point defects. From figure 4.8 (b), we observe that the dislocations and point defects play a significant role in pinning the flux lines in the parent $V_{0.60}Ti_{0.40}$ alloy. This, however changes with the addition of Gd and flux line pinning at the grain boundaries increases. For the $x = 0.01$ alloy, the position of the peak suggest that the grain boundaries are major pinning centres. As multiple

pinning mechanisms are present in these alloys, it is difficult to obtain a reliable fit to the experimental data using Dew Hughes' theory. Therefore, we have used Kramer plots to understand the pinning mechanisms present in these alloys. According to Kramer's theory, the $J_c^{1/q}H^{(1-p)/q}$ vs. H plots approximate to straight lines for different type of pinning mechanisms [143]. Here, p and q are the coefficients corresponding to a specific type of pinning mechanism similar to the Dew Hughes' model. For normal surface pinning ($p = 0.5$ and $q = 2$), the $J_c^{0.5}H^{0.25}$ vs. H plot is known as the Kramer plot [144].

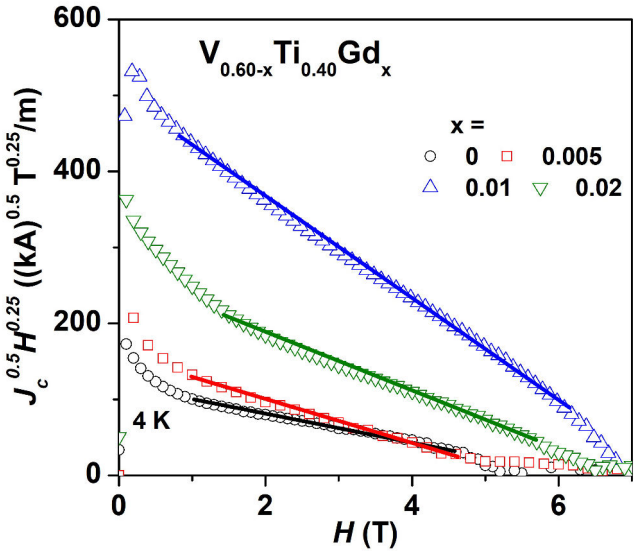

FIGURE 4.9: (a) Kramer plots for the $V_{0.60-x}Ti_{0.40}Gd_x$ alloys at 4 K.

Figure 4.9 shows the Kramer plots for the $V_{0.60-x}Ti_{0.40}Gd_x$ alloys at 4 K. The empty symbols are the experimental data points and the straight lines indicate the field regime over which the linearity is observed. For the $x = 0$ alloy, the linearity is observed over the field range 1 - 4.6 T. However, for the alloy with 1 at. % Gd, the linearity is observed in the field range 0.8 T to 6.2 T. This increase of the linear region with the addition of Gd indicates that the field regime over which the pinning mechanism is dominated by the GBs increases with Gd addition. This is also consistent with our metallography results, where the reduction in the grain size was observed with the addition of Gd. The larger size Gd clusters and the

stronger ferromagnetic order probably affect the flux line distributions in the x = 0.02 alloy and hence the pinning force density is reduced.

4.2 Summary

We have studied the ρ, M and J_c of the $V_{0.60-x}Ti_{0.40}Gd_x$ alloys. Our results show that the addition of Gd in the $V_{0.60}Ti_{0.40}$ alloy effectively reduces the grain size of these alloys, which leads to the enhancement of J_c due to increased pinning at the GBs. The J_c and F_P are the maximum for the alloy with 1 at. % Gd. At 4 K, the J_c of the $x = 0.01$ alloy is more than 20 times higher up to H_{irr} in comparison with the $V_{0.60}Ti_{0.40}$ alloy. We also observe that even in the presence of ferromagnetic order introduced in the system by the magnetic moments of Gd, there is a slight enhancement of the T_{sc}.

Chapter 5

Coexisting ferromagnetism and superconductivity in Gd added $V_{0.60}Ti_{0.40}$ alloys

As seen in the last chapter, the addition of 1 at. % Gd in the $V_{0.60}Ti_{0.40}$ alloy enhances the J_c by more than 20 times up to the H_{irr} [145]. Apart from the enhancement of J_c, the alloys containing Gd also exhibit:

(i) a ferromagnetic transition at T_{mc} = 295 K, and

(ii) slight enhancement of the T_{sc}.

In this chapter, we look into the origin of the above experimental findings.

The T_{sc} of many binary alloys such as $La_{1-x}Gd_x$ [146, 147], $Pb_{1-x}Gd_x$ [147, 148, 149] etc., and pseudo-binaries such as $Ce_{1-x}Gd_xRu_2$ [147, 150] and $La_{1-x}Gd_xAl_2$ [147, 151] etc., decreases with increasing x because of pair breaking due to exchange interaction between the Gd $4f$ moments and the conduction electrons [147]. The magnetic order in these systems appear in the alloys where the T_{sc} has been substantially decreased, or after the complete suppression of superconductivity [146, 150]. Therefore, it is somewhat surprising that the superconducting properties get enhanced in the presence of ferromagnetism in the Gd containing $V_{0.60}Ti_{0.40}$ alloys.

5.1 Results and Discussion

5.1.1 Temperature dependence of magnetization of the $V_{0.60-x}Ti_{0.40}Gd_x$ alloys

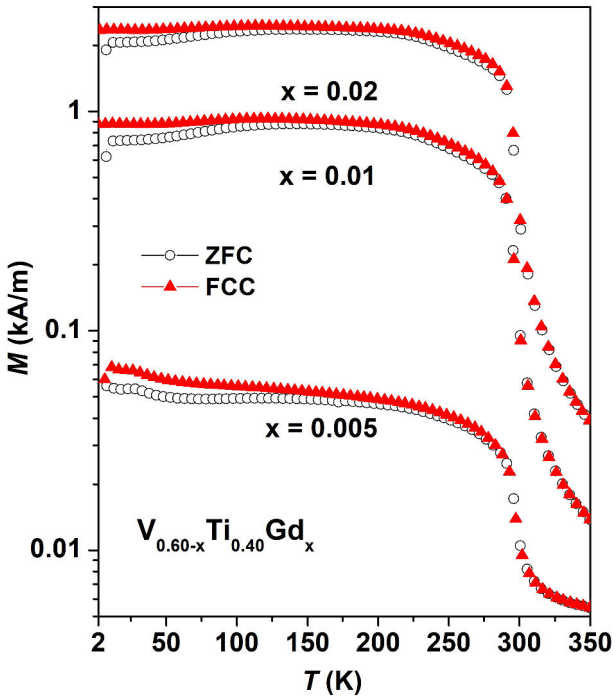

FIGURE 5.1: The $M(T)$ of the $V_{0.60-x}Ti_{0.40}Gd_x$ ($x > 0$) alloys measured in H = 10 mT in the temperature range 8 - 350 K. All the samples show the indication of a paramagnetic to ferromagnetic phase transition at T_{mc} = 295 K, which is the T_{mc} of elemental Gd.

Figure 5.1 shows the $M(T)$ of the $V_{0.60-x}Ti_{0.40}Gd_x$ ($x > 0$) alloys in the presence of 10 mT magnetic field in the T range 8 - 350 K, measured in the ZFC and FCC protocols. As stated in the previous chapter, the indication of the paramagnetic to ferromagnetic transition at T_{mc} = 295 K corresponds to that of elemental Gd [145, 152].

Figure 5.2 shows the (a) normal state $M(H)$ and (b) Arrott plots (M^2 vs. H/M plots) [153] at 10 K for the $x > 0$ alloys. Though there is a slight change of curvature in the low fields for the x = 0.005 alloy, the $M(H)$ increases almost linearly. For the x = 0.01 and 0.02 alloys at 10 K, the technical saturation is observed above $\sim$ 1 T.

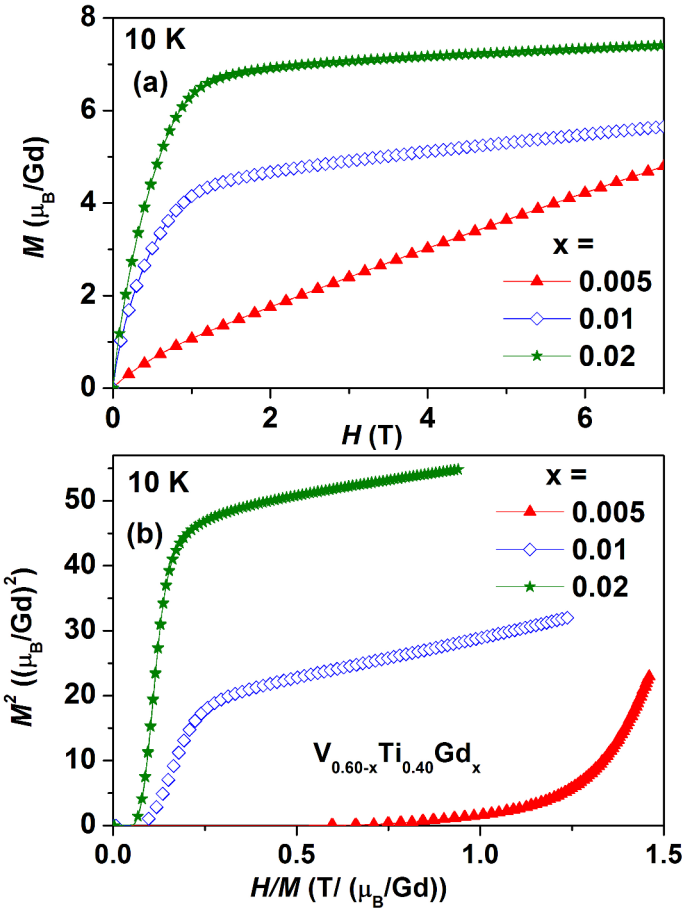

FIGURE 5.2: (a) The $M(H)$ of the $V_{0.60-x}Ti_{0.40}Gd_x$ ($x > 0$) alloys measured at 10 K. Magnetization saturates above $\sim$ 1 T for $x \geq 0.01$. (b) The Arrott plot for the $x > 0$ alloys at 10 K.

Although all the alloys containing Gd show an inflection point similar to a paramagnetic to ferromagnetic transition at 295 K, no spontaneous magnetization is observed for the $x = 0.005$ alloy. The spontaneous magnetization (M_s) is estimated from the Arrott plots for the $x = 0.01$ and 0.02 alloys at 10 K. The M_s is about 4.05 μ_B/Gd atom and 6.67 μ_B/Gd atom for the $x = 0.01$ and 0.02 alloys respectively. Previously, Hankiewicz *et al.* has shown that micron-sized Gd clusters can lead to long-range ferromagnetism in a system [154]. In a similar manner, the micron-sized Gd clusters present in the alloys containing Gd lead to ferromagnetic order in the $V_{0.60-x}Ti_{0.40}Gd_x$ alloys, where the magnetic moments of the Gd-clusters present along the grain boundaries (GBs) polarize the electrons along and around

the GBs.

We have observed that the $\rho(T)$ of the $V_{0.60}Ti_{0.40}$ alloy above 200 K is lower than that of the $x > 0$ alloys. Therefore, the reduction of $\rho(T)$ of the $x > 0.005$ alloys at low temperatures with respect to that of $x = 0$ alloy may not be due to ferromagnetism. Previously, Matin *et al.* have shown that the enhancement of T_{sc} in the V_yTi_{1-y} alloys in comparison with that of V is due to the reduction in the itinerant ferromagnetic spin fluctuations (IFSF) [95, 155]. Moreover, the fluctuation conductivity in the $V_{0.40}Ti_{0.60}$ alloy at $T < 3T_{sc}$ indicated a local variation of the FSF coupling constant (λ_{sf}) due to random disorder [155]. The addition of Gd suppresses the FSF in the uranium based systems such as UAl_2 and UAl_3 by the exchange interaction of localized Gd $4f$ moments with the conduction electrons [156, 157, 158]. In similar lines, the addition of Gd in the $V_{0.60}Ti_{0.40}$ alloy might also result in the suppression of IFSF. This conjecture is also supported by the fact that the $T_{sc}(x > 0) > T_{sc}(x = 0)$. The suppression of IFSF can be verified from the temperature dependence of thermal conductivity ($\kappa(T)$) behaviour, as the IFSF does not limit the heat conduction by the electrons and phonons [131]. The changes in $\kappa(T)$ are mainly due to the scattering by the defects generated in the $V_{0.40}Ti_{0.60}$ alloy with the addition of Gd.

5.1.2 Thermal conductivity of the $V_{0.60-x}Ti_{0.40}Gd_x$ alloys

Figures 5.3 (a) - (d) show the $\kappa(T)$ curves for the $V_{0.60-x}Ti_{0.40}Gd_x$ alloys. The open symbols correspond to the $\kappa(T)$ in the absence of applied magnetic field in the temperature range 2 - 50 K, whereas the solid symbols correspond to $\kappa(T)$ in the presence of 8 T magnetic field in the temperature range 2 - 15 K. For a given temperature, the κ reduces slightly with increasing Gd content in the $V_{0.60}Ti_{0.40}$ alloys up to $x = 0.01$, and then increases for the $x = 0.02$ alloy.

Normal state thermal conductivity of the $V_{0.60-x}Ti_{0.40}Gd_x$ alloys

Figures 5.4 (a) - (d) show the normal state thermal conductivity (κ_n) of the $V_{0.60-x}Ti_{0.40}Gd_x$ alloys in the temperature range 4.5-50 K. In the absence of any applied magnetic field, these

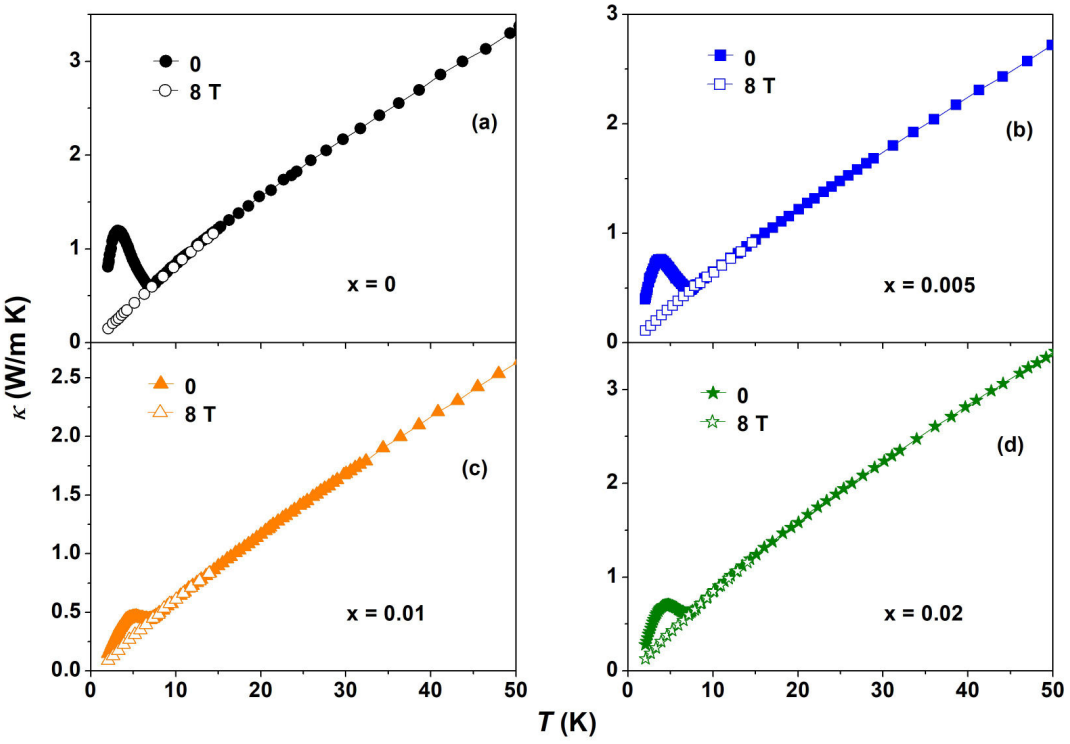

FIGURE 5.3: (a) - (d) Temperature dependence of thermal conductivity ($\kappa(T)$) of the $V_{0.60-x}Ti_{0.40}Gd_x$ alloys in zero and 8 T magnetic fields.

alloys become superconducting between 7.69 K to 7.78 K (see table 4.11 of chapter 4). Since these alloys are superconducting below $\sim$ 4.5 K even in the presence of 8 T magnetic field, we have obtained κ_n in the temperature range 4.5 K to 8 K by applying an 8 T magnetic field. The normal state electronic and phononic thermal conductivties are limited by various scattering mechanisms as mentioned in section 1.5 of chapter 1 (equations 1.12 and 1.21). We have separated out the electronic and phononic contribution of κ_n following a similar procedure described in chapter 3. Our metallography studies (details are given chapter 4) reveal that the grain size reduces by more than an order of magnitude with the addition of Gd and becomes $\sim$ 20 μm for the $x = 0.02$ alloy, which is still larger than the average phonon mean free path (l_{ph}) in these alloys (< 100 nm [131]). The metallography images also indicate that the dislocation density in these alloys is very low. Thus, to fit the κ_n, we have only considered the scattering of electrons from defects and phonons, and the scattering of phonons from

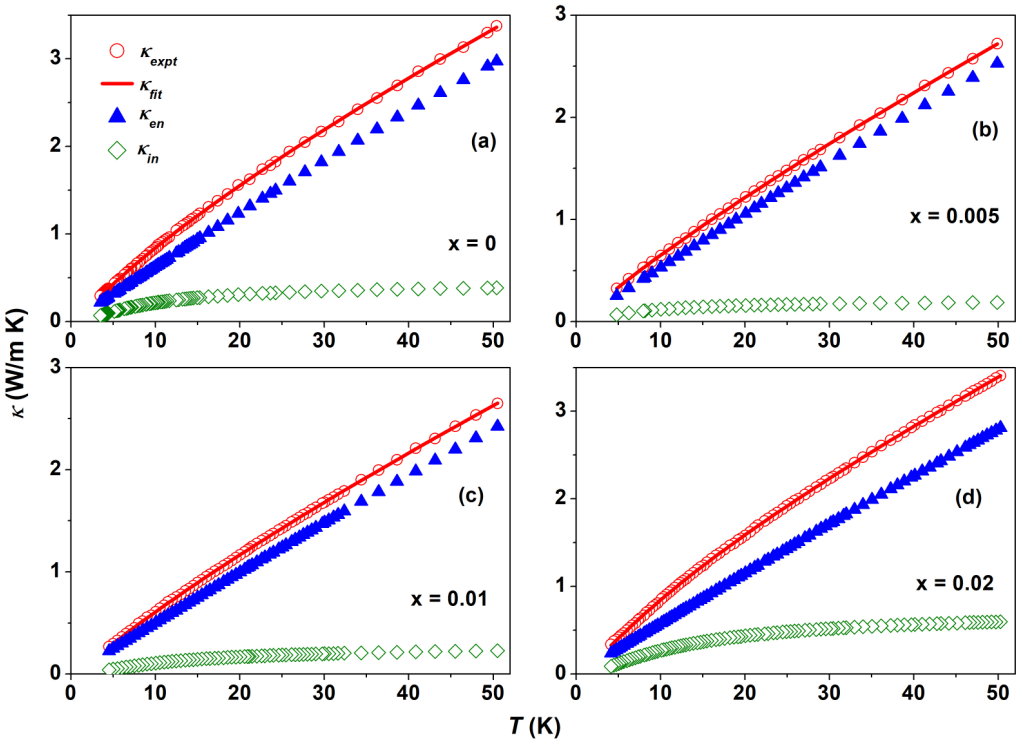

FIGURE 5.4: Normal state thermal conductivity ($\kappa_n(T)$) of the $V_{0.60-x}Ti_{0.40}Gd_x$ alloys in the temperature range 5 - 50 K. The open red circles are the experimental data points and the red lines are the fit to the $\kappa_n(T)$.

electrons and point defects. The red circles in the figure 5.4 represents the experimental data and the red lines are fit to them. A least square method based on the Levenberg-Marquardt algorithm was used to fit the experimental data. The convergence criterion for the reduced chi-aquare was set to 10^{-4} (details are described in chapter 3). The fitting parameters are listed in table 5.1. The blue solid triangles and the open diamond symbols in olive colour are the electronic (κ_{en}) and phononic contribution (κ_{ln}) to the κ_n estimated using the parameters obtained by fitting equations 1.12 and 1.21. We see that, similar to the $V_{1-x}Ti_x$ alloys, the electrons carry majority of the heat in the normal state of these alloys. The static disorders are the major scatterrer of electrons that limit the electronic heat conduction. Although the disorder increases with increasing Gd content in the $V_{0.60}Ti_{0.40}$ alloys [145], the coefficient A_n (which depicts the strength of electron-disorder scattering) decreases slightly

for the $x = 0.02$ alloy. This indicates that the electron mean free path (l_e) increases in spite of the increased disorder. This observation is in line with our resistivity results (discussed in chapter 4), where a reduction in the residual resistivity (ρ_0) was observed for the alloys with $x \geq 0.01$. The point defects scatter the high frequency phonons effectively, leaving the low frequency phonons to be scattered by electrons. The E_n/M and P_n/M increases initially and then decreases with increasing x. This indicates that with the addition of Gd in $V_{0.60}Ti_{0.40}$, the scattering of phonons from electrons and point defects increases for the $x = 0.005$ alloy and then decreases with further addition of Gd.

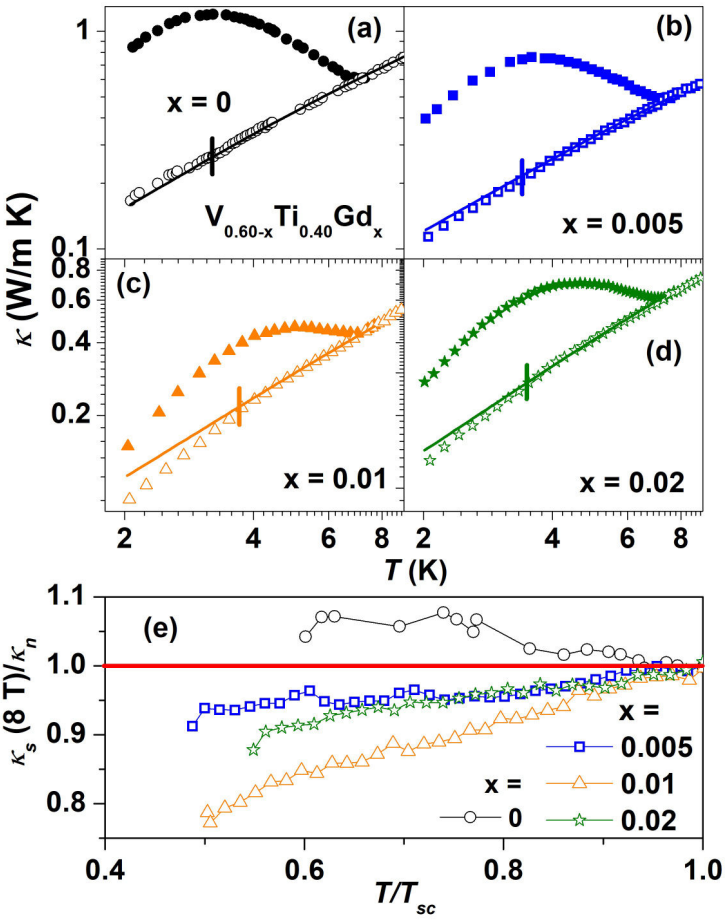

FIGURE 5.5: (a)-(d) Temperature dependence of thermal conductivity ($\kappa(T)$) of the $V_{0.60-x}Ti_{0.40}Gd_x$ alloys in zero (filled symbols) and 8 T (open symbols) magnetic field in the temperature range 2 - 9 K. (e) The ratio of $\kappa_s(H = 8\ T)$ to κ_n as a function of T/T_{sc}. In comparison with κ_n, the κ_s increases below T_{sc} for the $x = 0$ alloy, whereas it decreases for the alloys with $x > 0$.

Figures 5.5 (a) - (d) show the $\kappa(T)$ of $V_{0.60-x}Ti_{0.40}Gd_x$ alloys in the temperature range 2-9 K for $H = 0$ (solid symbols) and $H = 8$ T (open symbols). The solid lines in figures 5.5 (a) - (d) correspond to κ_n. We have estimated the κ_n for the temperature range 2 - 4.5 K with the help of the fitting parameters obtained using equations 1.11, 1.12 and 1.21. The plots are shown using a log-log scale for better visibility. The T_{sc} is taken as the temperature at which $\kappa(T)$ start to deviate from $\kappa_n(T)$. Similar to the $V_{1-x}Ti_x$ alloys [131], the $\kappa_s(T)$ starts to rise with the reduction of T below T_{sc} for $H = 0$, which indicates that the phonons carry majority of the heat in the superconducting state. In the presence of an 8 T magnetic field, the $\kappa(T)$ start to deviate from the κ_n around 4 K (marked by '|' lines) in figures 5.5 (a) - (d). The difference between the $\kappa_n(T)$ and $\kappa_s(T)$ being very small, we show in figure 5.5 (e), the ratios of κ_s ($H = 8$ T) to the κ_n as a function of reduced temperature $T/T_{sc}(H = 8$ T). We see that for the $V_{0.60}Ti_{0.40}$ alloy, the ratio κ_s ($H = 8$ T)/κ_n start to rise (above 1) with decreasing temperature, which shows that phonons are the major carriers of heat in this alloy in 8 T magnetic field. For the $x > 0$ alloys, κ_s ($H = 8$ T)/ κ_n decreases (below 1) with decreasing temperature below $T_{sc}(H = 8$ T), which shows that the electrons carry majority of the heat in 8 T. Therefore, we see that there is a crossover from phonon dominant heat conduction in low fields to electron dominant heat conduction in high fields for the alloys containing Gd. To understand this crossover, it is important to know how κ_e and κ_l change with the addition of Gd in the $V_{0.60}Ti_{0.40}$ alloy.

Effect of the addition of Gd in the electronic and phonon thermal conductivity

To understand the effect of the addition of Gd, we have estimated the κ_{es} and κ_{ls} using the Bardeen-Rickayzen-Tewordt theory [63, 68, 69] of thermal conductivity of superconductors (details are discussed in chapter 1). The κ_{es} of these alloys are estimated as, $\kappa_{es} = \kappa_{es,i}^{-1} + \kappa_{es,l}^{-1}$. Here, $\kappa_{es,i}$ and $\kappa_{es,l}$ are respectively the electronic thermal conductivity in the superconducting state limited by the scattering of electrons from disorder and phonons. The κ_{ls} is obtained

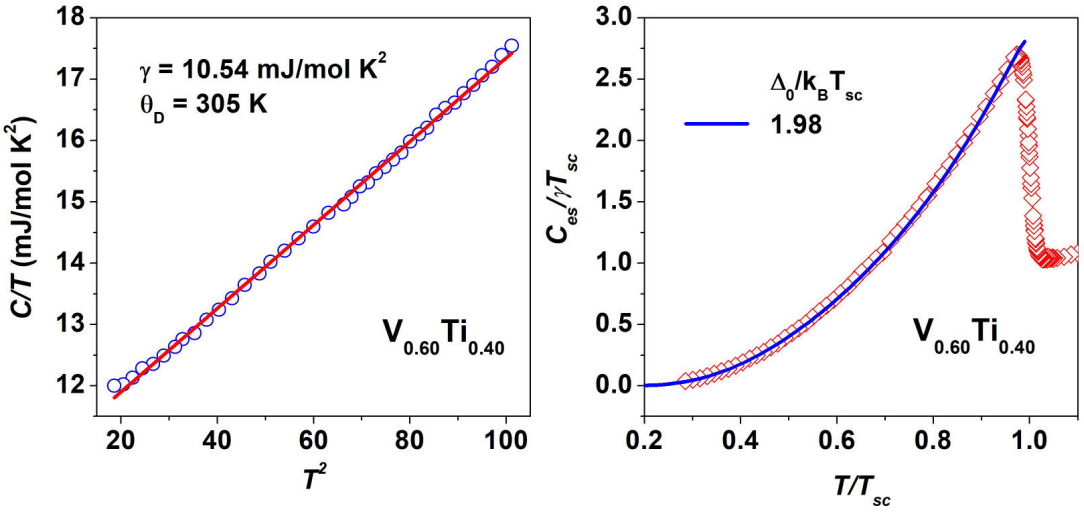

FIGURE 5.6: (a) Linear fit to C/T vs. T^2 of the normal state heat capacity data of the $V_{0.60}To_{0.40}$ alloy. (b) Fit to the $C_{es}/\gamma T_{sc}$ of the $V_{0.60}To_{0.40}$ alloy for $\Delta_0 = 1.98$ using equation 3.3.

by subtracting the κ_{es} from κ_s. The θ_D and the superconducting energy gap Δ_0 used to obtain the κ_{es} were obtained from the $C(T)$ data for these alloys. Since Gd is immiscible in the $V_{0.60}Ti_{0.40}$ alloy and precipitates only along the GBs, we have used the Δ_0 of the $V_{0.60}Ti_{0.40}$ alloy for all the samples. Figure 5.6 (a) shows the fit to the normal state heat capacity of the $V_{0.60}Ti_{0.40}$ alloy using the formula $C_n = \gamma T + \beta T^3$ and figure 5.6 (b) shows the fit to the $C_{es}/\gamma T_{sc}$ using equation 3.3. The θ_D = 305 K and $\Delta_0/k_B T_{sc}$ = 1.98 are obtained from the fitting and are used to estimate the κ_{es}. The $\kappa_{ls}(T)$ is estimated by subtracting $\kappa_{es}(T)$ from $\kappa_s(T)$ (see equation 1.22).

Figure 5.7 shows the ratios (a) $\kappa_{ez}(x)/\kappa_{ez}(0)$, (b) $\kappa_{lz}(x)/\kappa_{lz}(0)$ as a function of temperature in the normal and superconducting ($H = 0$) states. As disorder increases with the addition of Gd, the ratio $\kappa_{en}(x)/\kappa_{en}(0)$ decreases up to $x = 0.01$. However, for the $x = 0.02$ alloy, $\kappa_{en}(x)/\kappa_{en}(0)$ reaches almost unity for the $x = 0$ alloy. As the κ_{es} for all the alloys are estimated using the same $\Delta_0/k_B T_{sc}$, the ratio $\kappa_{es}(x)/\kappa_{es}(0)$ follows the changes in $\kappa_{en}(x)/\kappa_{en}(0)$. Similar to $\kappa_{en}(x)/\kappa_{en}(0)$, the ratio $\kappa_{ln}(x)/\kappa_{ln}(0)$ decreases with increasing x up to $x = 0.01$ and becomes almost 1 for the $x = 0.02$ alloy. This reduction in the ratios of $\kappa_{en}(x)/\kappa_{en}(0)$ and $\kappa_{ln}(x)/\kappa_{ln}(0)$ up to the $x = 0.01$ alloy and subsequent increase

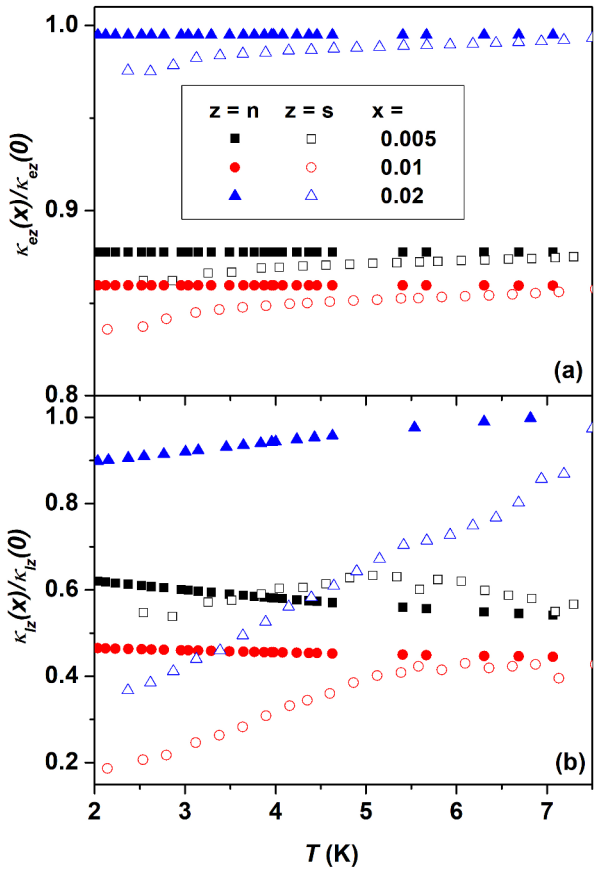

FIGURE 5.7: Ratios of (a) $\kappa_e(x)/\kappa_e(0)$, (b) $\kappa_l(x)/\kappa_l(0)$ as a function of temperature. With decreasing temperature, both κ_e and κ_l get reduced for the alloys containing Gd. The κ_e reduces 15% at most, whereas the κ_l reduces up to 80% for the $x = 0.01$ alloy in comparison with the $V_{0.60}Ti_{0.40}$ alloy.

for the alloy with $x = 0.02$ show that the thermal conductivity of these alloys are governed by electron-phonon interaction. The change in $\kappa_{ls}(x)/\kappa_{ls}(0)$ between T_{sc} and $T = 2$ K increases with increasing x. This is due to the fact that the static defects, which are the effective scatterers of phonons in the superconducting state, increase with the increasing Gd content. In comparison with the $V_{0.60}Ti_{0.40}$ alloy, κ_{ln} (κ_{ls}) reduces by 50 (80)% around 2 K for the $x = 0.01$ alloy, whereas the κ_e reduces only by about 15% for the same alloy around 2 K.

TABLE 5.1: Parameters obtained from the fitting of $\kappa_n(T)$ and $\kappa_{ls}(T)$. The variation in the values of the parameters satisfying the convergence criterion was within 2%.

Normal state			
x	A_n (m K^2 W^{-1})	E_n/M (m K^3 W^{-1})	P_n/M (m W^{-1})
0	15.9584	907.1563	0.1457
0.005	18.8599	1126.9	0.4028
0.01	19.9622	2607.4	0.1771
0.02	17.3044	1106	0.0628
Superconducting state			
H (T)	E_s/M (m K^3 W^{-1})	L_s/M (m K^3 W^{-1})	P_s/M (m W^{-1})
$x = 0$			
0	1607.5	31.5824	0.0041
2	1166.5	45.6484	0.074
4	900.4585	56.0613	0.1764
6	642.20	59.6212	0.3635
$x = 0.02$			
0	1892.6	95.8641	0.0084
2	1160.5	116.9342	0.0912
4	967.6129	128.525	0.1862
6	783.9803	129.3814	0.3965

Temperature dependence of thermal conductivity in the presence of different magnetic fields

The κ_{ls} of the $V_{0.60-x}Ti_{0.40}Gd_x$ alloys is greatly affected by the disorder introduced by the addition of Gd in the $V_{0.60}Ti_{0.40}$ alloy. Therefore, we have measured the $\kappa_s(T)$ of the parent alloy and the alloy containing the maximum amount of Gd in the presence of different magnetic fields. The $\kappa_s(T, H \neq 0)$ of the $x = 0$ and $x = 0.02$ alloys are analysed using the effective gap model (EGM) [159, 160]. According to the EGM, the effect of magnetic field on $\kappa_s(T)$ can be incorporated as a field dependent effective superconducting energy gap at different temperatures ($\Delta(T, H)$). The $\Delta(T, H)$ is given by, $\Delta(T, H) = \Delta(T)(1 - \frac{B}{H_{c2}(T)})^{1/2}$. Here, H_{c2} is the upper critical field and $B \simeq H$ for $H \gg H_{c1}$. Using the temperature dependence of heat capacity measured in the presence of various magnetic fields, we have estimated the T dependence of H_{c2}. Figures 5.8 (a) - (d) show the $C(T)$ curves for the $V_{0.60-x}Ti_{0.40}Gd_x$

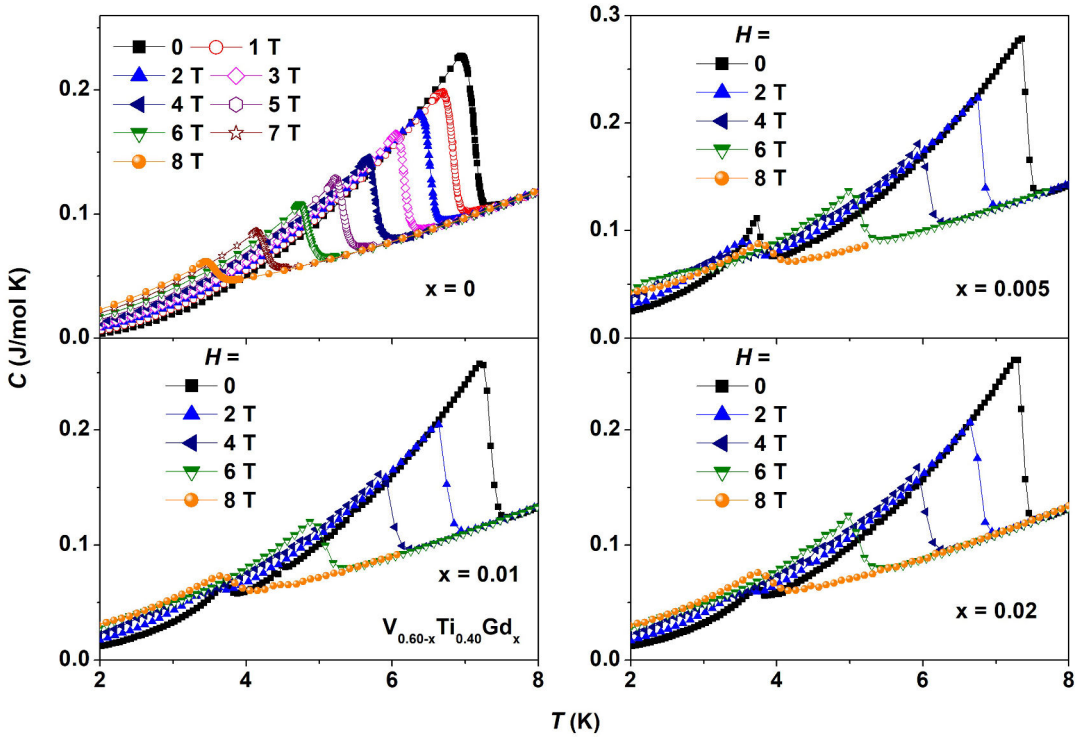

FIGURE 5.8: Temperature dependence of the heat capacity of the $V_{0.60-x}Ti_{0.40}Gd_x$ alloys in the presence of different magnetic fields.

alloys in the presence of different magnetic fields. The T_{sc} in the presence of different magnetic fields is taken as the temperature at which the corresponding $\frac{dC(T)}{dT}$ shows a minimum. Figure 5.9 shows the plot of H_{c2} of these alloys as a function of T. The symbols correspond to the experimentally obtained H_{c2} and the lines are fit to the experimental data. The $H_{c2}(T)$ is found to follow the standard relation $H_{c2}(T) = H_{c2}(0)(1-(T/T_{sc})^2)$ [24]. The $H_{c2}(0)$ for the $x = 0$ alloy is 11 T, which increases slightly with the addition of Gd. The H_{c2} for the $x > 0$ alloys is about 11.5 T. Using the $H_{c2}(T)$ for these alloys, we have separated the $\kappa_{es}(T)$ and $\kappa_{ls}(T)$ for different H. The $\kappa_{es}(T)$ and $\kappa_{ls}(T)$ of the $x = 0$ and $x = 0.02$ alloys in the presence of various magnetic fields are shown in figures 5.10 (a) and (b) respectively. The $\kappa_{en}(0.02) \simeq \kappa_{en}(0)$ over the whole temperature range. Thus, the values of $\kappa_{es}(T)$ is almost same for both the $x = 0$ and $x = 0.02$ alloys, even in the presence of magnetic fields. However, κ_{ls} of the $x = 0.02$ alloy is significantly lower than that of

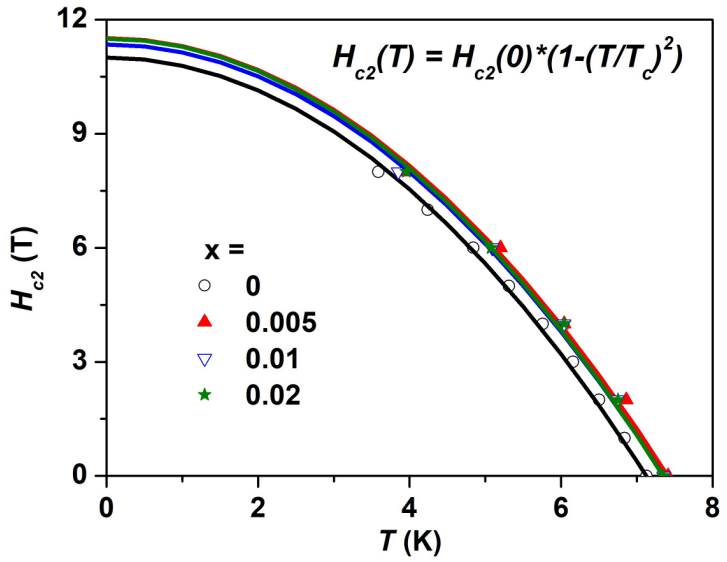

FIGURE 5.9: Temperature dependence of the upper critical field of the $V_{0.60-x}Ti_{0.40}Gd_x$ alloys.

$x = 0$ alloy. The solid lines are fit to the κ_{ls} using equation 1.28, where we have used the $\Delta(T,H)$ according to the EGM [159, 160]. We have followed a similar least square fitting procedure as discussed before to fit the experimental data. Table 5.1 contains the thermal resistivity coefficients corresponding to various scattering mechanisms obtained from the above curve-fitting. The coefficient of the phonon thermal resistivity originating due to the scattering of phonons from electrons has a higher value in the superconducting state (E_s/M) than that in the normal state (E_n/M). The value of the coefficient of the phonon thermal resistivity limited by the scattering of phonons from electrons, is much lower in the superconducting state (P_s/M) than that in the normal state (P_n/M). The loss of normal electron density (n_e) below $T_{sc}(H = 0)$ leads to the increase of the phonon mean free path l_l of the low frequency phonons, which reduces the scattering of phonons from the point defects. Thus, the scattering of phonons from electrons govern the heat conduction below T_{sc}. With decreasing T below T_{sc}, the scattering of phonons from electrons reduces due to the reduction in n_e. As a result, the l_l increases and below a certain temperature ($\sim T_{sc}/2$), the l_l becomes comparable to the inter-dislocation distances and then the dislocations become the dominant scatterers of phonons. Below T_{sc}, as n_e increases with increasing magnetic fields

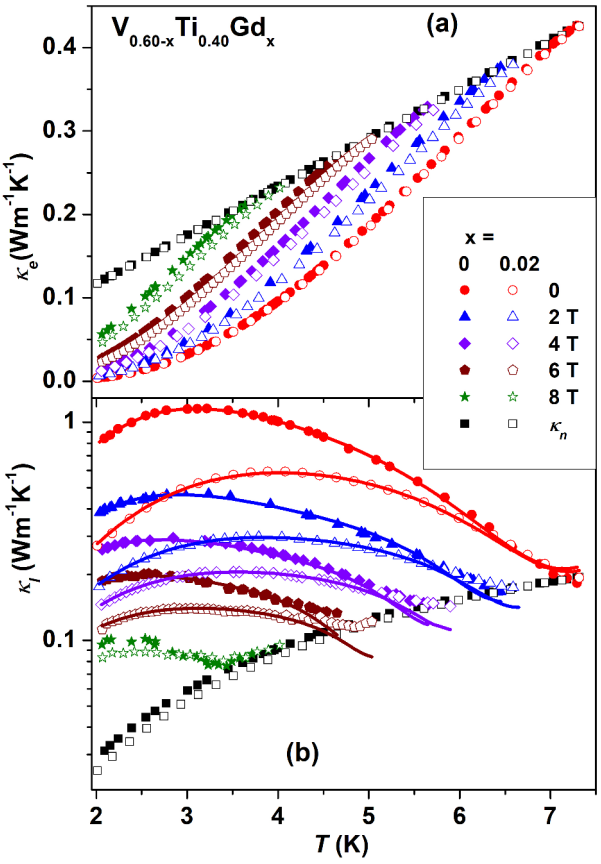

FIGURE 5.10: Comparison of (a) $\kappa_{es}(T)$ and (b) $\kappa_{ls}(T)$ of the $x = 0$ and $x = 0.02$ alloys in different magnetic fields. The $\kappa_{es}(T)$ of both the alloys in each field are almost the same but the $\kappa_{ls}(T)$ of the $x = 0.02$ alloy is significantly lower than that of $x = 0$. The symbols are experimental data points and the lines are fit to the $\kappa_{ls}(T)$ obtained using equation 1.28.

the scattering of phonons from electrons also increases. Therefore, $l_l(T, H \neq 0)$ is less than $l_l(T, H = 0)$ and the point defects and dislocations scatter the phonons more effectively with increasing H. Hence, both P_s/M and L_s/M increases with increasing H. On the other hand, with increasing H, the electrons become less effective scatterers of phonons and hence E_s/M decreases with increasing magnetic field. The coefficients of scattering of phonons from electrons (E_s/M) and point defects (P_s/M) for each H are almost same for both the $x = 0$ and $x = 0.02$ alloys. But the coefficient of scattering of phonons from dislocations (L_s/M) is about 2 - 3 times higher for the $x = 0.02$ alloy in comparison with the $x = 0$ alloy for each H. This shows that the suppression of the κ_{ls} in the alloys containing Gd is

mainly due to the scattering of phonons from dislocations.

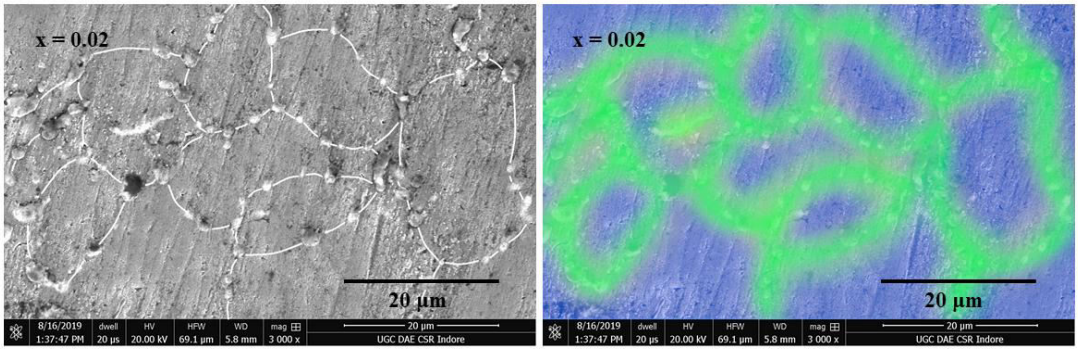

FIGURE 5.11: (a) Metallography image of the $V_{0.68}Ti_{0.40}Gd_{0.02}$ alloy. (b) Reconstructed schematic depicting regions of superconductivity (blue) and regions of conduction electron polarization leading to ferromagnetism (green).

The understanding that evolves from the experimental results are summarized in figure 5.11. In this figure, the panel (a) shows a large area SEM image of the $x = 0.02$ alloy. We see that the Gd precipitates uniformly along the GBs throughout the region. The magnetic moments of the Gd polarize the conduction electrons along and around the GBs, schematically represented by the green regions in figure 5.11 (b). The conduction electrons deep inside the grains (blue regions in figure 5.11 (b)) only feel the average internal field generated by magnetic ordering below T_{mc}. Thus, the IFSF are suppressed partially inside the grains resulting in the enhancement of the T_{sc} in the Gd containing alloys. The increase in the disorder by the addition of Gd reduces the mean free path (l_e) of conduction electrons, whereas the conduction electron polarization along the GBs due to Gd magnetic moments increases l_e. Therefore, the effective l_e decreases initially with the increase in x and then increases for large values of x. This results in the reduction of $\rho(T)$ of the $x > 0.005$ alloys below 100 K and an enhancement of κ for the $x = 0.02$ alloy. As the l_e does not change much with the addition of Gd, the κ_e reduces only 15 % in the Gd-containing alloys in comparison with the $V_{0.60}Ti_{0.40}$ alloy. On the other hand, the l_l reduces with increasing x due to increased scattering of phonons from disorder. This leads to the suppression of κ_l up to 80 %. When

magnetic field is applied, κ_{ls} reduces further and results in the $\kappa_s(T)$ of the $x > 0$ alloys to be dominated by electrons for 8 T magnetic field.

5.2 Summary

We have studied the M and κ of the $V_{0.60-x}Ti_{0.40}Gd_x$ ($x = 0, 0.005, 0.01, 0.02$) alloys as functions of T and H. The rare earth Gd precipitates in clusters along the GBs and causes grain refinement and enhancement of dislocation densities in comparison with those of the parent alloy. The magnetic moments of Gd also causes polarization of the conduction electrons along and around the GBs. The conduction electron polarization results in the following features:

(a) A ferromagnetic transition at T_{mc} = 295 K.

(b) Partial suppression of spin fluctuations inside the grains leading to slight enhancement of T_{sc}.

(c) Increase of l_e leading to reduction of $\rho(T)$ below 100 K for the $x > 0.005$ alloys and an enhancement of $\kappa(T)$ of the $x > 0.01$ alloys.

(d) A crossover from phonon dominant heat conduction for H = 0 to electron dominant heat conduction for 8 T magnetic field in the superconducting state of the alloys containing Gd.

Chapter 6

Structural and magnetic properties of the as cast $V_{1-x}Zr_x$ alloy superconductors

Unlike the V-Ti alloys studied in the previous chapters, the C15 Laves phase ZrV_2 based superconductors are brittle [10, 11] and alloying is a widely used technique to enhance the mechanical properties of a material. The mechanical properties are also reported to improve when the constituent elements are taken in off-stoichiometric proportions [80]. Therefore, instead of the ZrV_2 compound, we study the $V_{1-x}Zr_x$ alloys with x = 0.05, 0.10, 0.20, 0.29, 0.33 and 0.40. The equilibrium phase diagram of the $V_{1-x}Zr_x$ alloys is shown in figure 6.1. The phase diagram has been reconstructed using the data available in literature [161, 162, 163, 164]. The solubility of Zr in V is only $\sim$ 2% at room temperature and $\sim$ 5% at 1300 ^{o}C. The equilibrium phase diagram of the $V_{1-x}Zr_x$ alloys shows three isotherms. A peritectic isotherm is observed at 1300 ^{o}C for $0.05 \leq x \leq 0.47$. During the peritectic reaction, the solid body centred cubic (*bcc*) β-V reacts with the liquid and forms another solid face centred cubic (*fcc*) γ'-ZrV_2 (space group *Fd-3m:1*) phase. The eutectic isotherm is observed for $0.33 \leq x \leq 0.835$. During the eutectic reaction, the liquid transforms into two solid body centred cubic (*bcc*) β-Zr and face centred cubic (*fcc*) γ-ZrV_2 (space group *Fd-3m:1*) phases. A eutectoid isotherm is also observed at 777 ^{o}C, where the β-Zr transforms into hexagonal close-packed (*hcp*) α-Zr phase. Thus the off-stoichiometric $V_{1-x}Zr_x$ alloys form with multiple structural phases, which might enhance the J_c as well. In this chapter, we

provide a detailed discussion on the structural, superconducting and flux pinning properties of the as-cast $V_{1-x}Zr_x$ alloys.

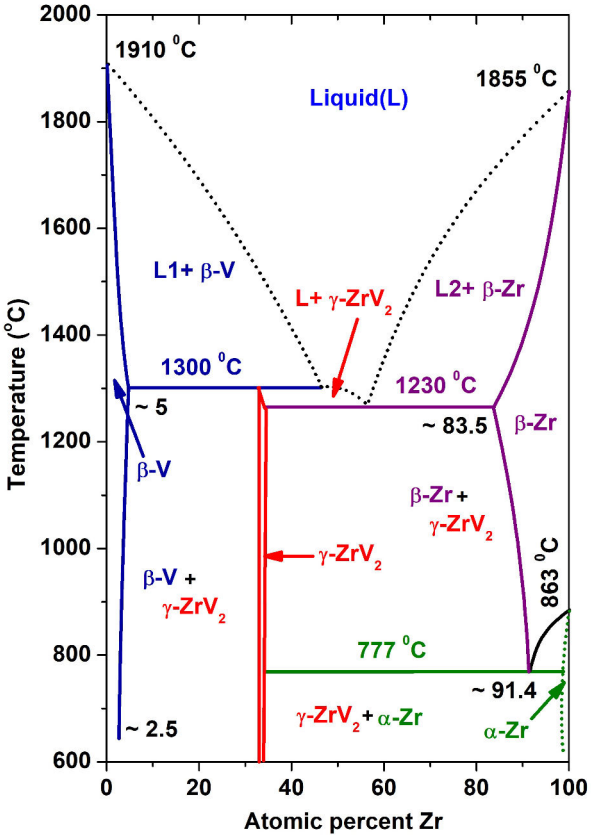

FIGURE 6.1: Equilibrium phase diagram of the $V_{1-x}Zr_x$ alloys.

6.1 Results and Discussion

6.1.1 Sample characterization

The as-prepared samples were characterized with the help of XRD and metallography studies. Figure 6.2 show the room temperature XRD pattern of the $V_{0.60}Zr_{0.40}$ alloy in the 2θ range 30 - 90^o. The XRD patterns corresponding to the ZrV_2 and α-Zr phases are also shown. We have used the Powder Cell software [165, 166] to simulate the XRD patterns of ZrV_2 and α-Zr phases. These alloys also show reflections corresponding to β-V, α-Zr and

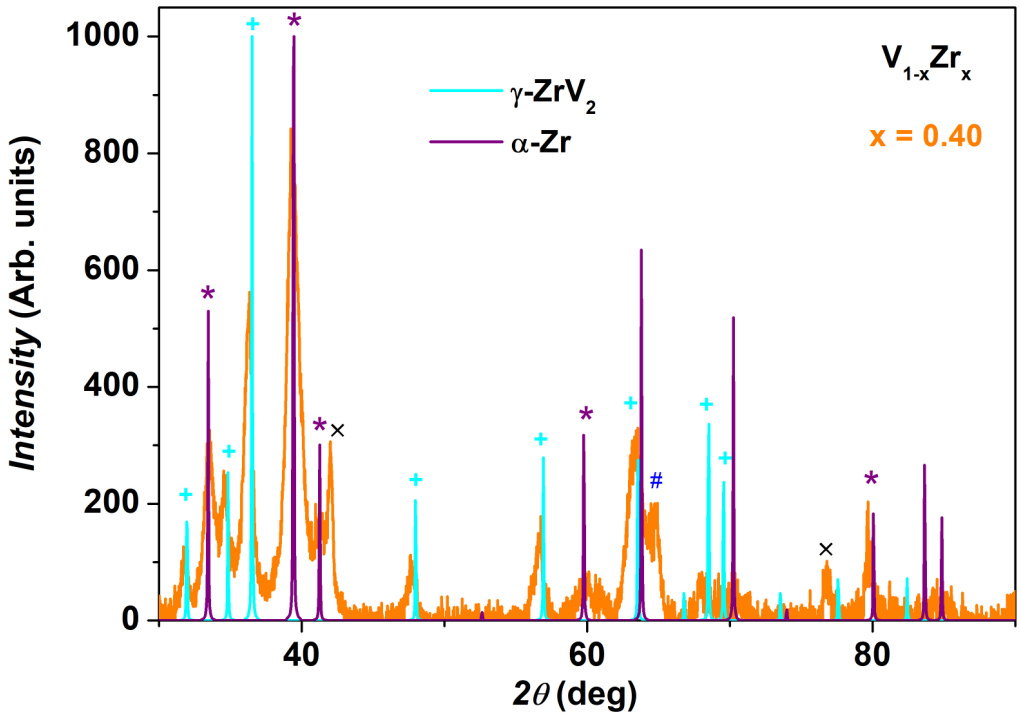

FIGURE 6.2: X-ray diffraction patterns of the $V_{0.60}Zr_{0.40}$ alloy at room temperature. Reflections from the β-V, α-Zr and γ-ZrV_2 phases are observed. The peak marked by '#' is from the β-Zr phase.

γ-ZrV_2 phases in their XRD patterns. The peaks corresponding to the β-V, γ-ZrV_2 and α-Zr phases are marked by '$\times$', '$+$' and '*' respectively. An additional reflection from the β-Zr phase (marked by '#') is also observed.

Figure 6.3 shows the room temperature XRD patterns of the $V_{1-x}Zr_x$ alloys in the 2θ range 30 - 90^o. Reflections from the β-V, α-Zr and γ-ZrV_2 phases are observed in all the samples containing Zr. The peaks corresponding to the β-V, γ-ZrV_2 and α-Zr phases are marked for the alloys containing Zr. However, we could not perform a Reitveld refinement of the XRD data, as the measurements were performed on a bulk sample. These samples being soft and malleable, it is rather difficult to get powders out of them. The presence of reflections from the α-Zr phase in all the present V-rich alloys suggests that these alloys undergo both peritectic and eutectic type reactions during cooling from the molten state.

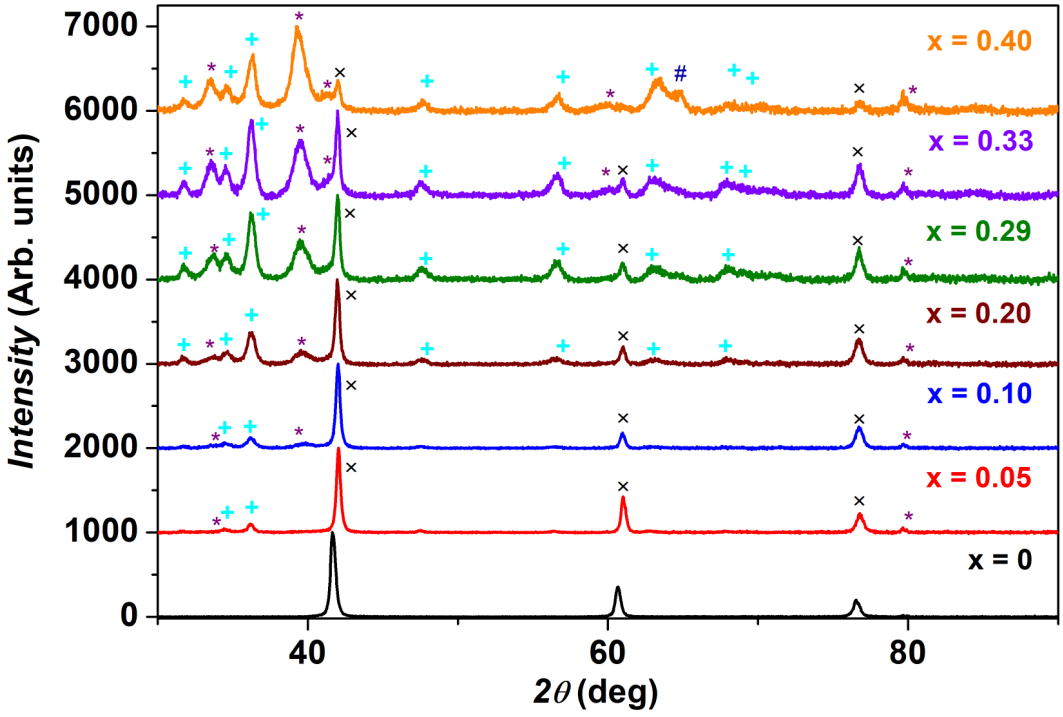

FIGURE 6.3: X-ray diffraction patterns of the $V_{1-x}Zr_x$ alloys at room temperature. All the alloys containing Zr show reflections from β-V, α-Zr and γ-ZrV_2 phases.

However, the $V_{1-x}Zr_x$ alloys undergo a eutectic reaction while cooling only for the compositions having Zr-content more than 33 at. % [161]. Thus, the presence of α-Zr in the V-rich alloys is unexpected. The β-Zr phase is known to form when these alloys undergo a eutectoid transformation at 777 ^{o}C [161]. Thus, the presence of the β-Zr phase in the x = 0.40 alloy indicates that this alloy has undergone eutectoid transformation.

Figures 6.4 and 6.5 show the scanning electron micrographs of the $V_{1-x}Zr_x$ alloys. Three distinct type of microstructures are observed in these alloys marked by '1', '2' and '3' in figures 6.4 (c) and 6.5 (c). The region marked by '1' has a Zr content less than 3%. We identify this phase as β-V, which solidifies first at 1910 ^{o}C while cooling from the molten state. With increasing Zr concentration in V, the grain size of this phase reduces. This β-V type of microstructure is observed up to x = 0.33. As the solubility of Zr in V is only $\sim$ 5% even at 1300 ^{o}C, the excess Zr is expelled out with the lowering of T. This results in the

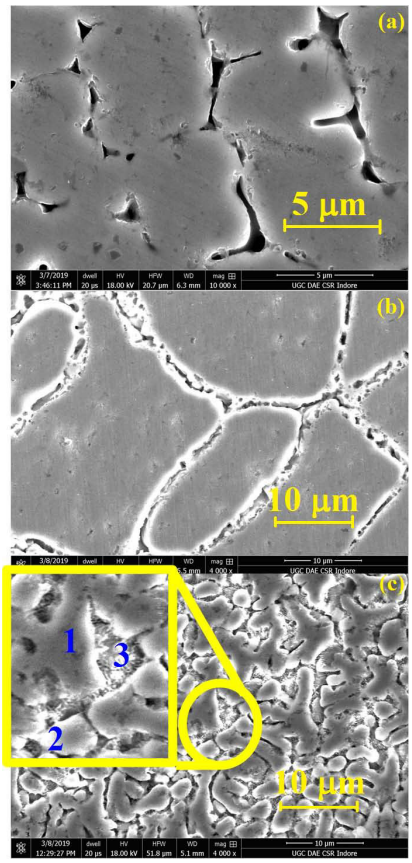

FIGURE 6.4: Scanning electron microscopy images of polished and etched as-cast $V_{1-x}Zr_x$ alloys for x = (a) 0.05 (b) 0.10 (c) 0.20. Three types of microstructures are observed. The plain regions (marked $'1'$) have β-V structure. The edges of the plain regions (marked $'2'$) have C15 ZrV_2 (γ') phase which is formed due to the peritectic reaction at 1300 ^{o}C. The lamellar structure (marked $'3'$) observed between the plain regions are due to the eutectic reaction at 1230 ^{0}C which has the mixture of α-Zr and γ-ZrV_2 phases.

formation of a Zr enriched liquid around the solid β-V phase. The boundary regions of the β-V phase marked by '2' (inset to figure 6.4 (c)) have an amount of Zr up to 50 at.%. The peritectic reaction at 1300 ^{o}C [161, 167] between the solid β-V phase and the Zr enriched liquid gives rise to the precipitation of the γ'-ZrV_2 phase. The formation of γ'-ZrV_2 phase further increases the Zr concentration in the liquid. This happens due to the very little time available for this reaction to get completed during the rapid cooling after the arc is switched off. As the Zr content in the liquid goes beyond 33 at.%, the liquid undergoes a eutectic-type reaction when the sample temperature decreases below 1230 ^{o}C. The eutectic type reaction

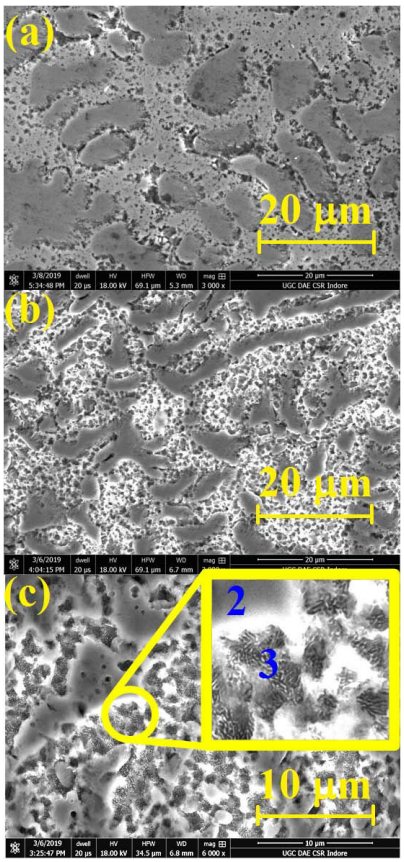

FIGURE 6.5: Scanning electron microscopy images of polished and etched as-cast $V_{1-x}Zr_x$ alloys for x = (a) 0.29, (b) 0.33 and (c) 0.40. The microstructures of the x = 0.29 and 0.33 alloys are similar to that of $x \leq 0.2$. In the x = 0.40 alloy, the region labelled as $'2'$ has the γ'-ZrV_2 phase and the region $'3'$ has the mixture of α-Zr and γ-ZrV_2 phases.

leads to the formation of the β-Zr and γ-ZrV_2 phases. This γ-ZrV_2 phase has a slightly different composition than γ'-ZrV_2. With further reduction in T, the β-Zr phase transforms into α-Zr when the T decreases below 777 ^{o}C. A lamellar microstructure is observed in the regions that undergo eutectic reaction (marked as $'3'$) and has a rich Zr content up to 75 at.%. For the x = 0.05, 0.10 and 0.20 alloys, the overall microstructure appears to be peritectic type, but for the alloys with higher Zr concentration the hypo-eutectic type [167] features become more prominent. The regions of the sample etched out by the etchant used to reveal the microstructure appear as voids in figures 6.4 (a) and (b). The γ-ZrV_2 being more reactive with HF, gets preferentially etched out [161]. The etched out regions contain eutectic type

microstructure. For the $x = 0.40$ alloy, the microstructure is slightly different from those of the other alloys. Although the XRD pattern of the $V_{0.60}Zr_{0.40}$ alloy indicates the presence of the β-V phase in a small amount, the metallography images (see Fig. 6.4 (c)) do not show any signature of the same. The region marked by '2' has a Zr content between 25 to 50 at.% which is in γ'-ZrV_2, whereas the region marked by '3' contain about 75 at.% of Zr as a mixture of γ-ZrV_2 and α-Zr phases. The overall micro structure of the $x = 0.40$ alloy is also hypo-eutectic type [167] Therefore, the features of non-equilibrium phase formation of the $V_{1-x}Zr_x$ alloys presented here is considerably different from the equilibrium phase diagram available in the literature [161, 168]. Microstructure similar to that revealed in our study has only been reported for the alloys with $x \geq 0.43$ [164].

6.1.2 Temperature dependence of resistivity of the $V_{1-x}Zr_x$ alloys

Figure 6.6 shows the $\rho(T)$ curves for the $V_{1-x}Zr_x$ alloys in the range 2-300 K measured in the absence of applied magnetic field. With increasing x, the amount of different phases increases in the $V_{1-x}Zr_x$ alloys and this increases the scattering of electrons from the defects. This in turn increases the residual resistivity ρ_0 of these alloys with increasing Zr-content in V. Figures 6.6 (b) and (c) show the expanded view of $\rho(T)$ of the $V_{1-x}Zr_x$ alloys close to the superconducting transition temperature (T_{sc}). The T_{sc} of V is 5.2 K and increases slightly for the $x = 0.05$ alloy and becomes 5.6 K. A moderate drop in $\rho(T)$ is also observed in the T range 8.5 K to 5.6 K for the $x = 0.05$ alloy, which is due to the presence of a small amount of ZrV_2 phase. The alloys with $x \geq 0.10$ become superconducting just below 8.5 K. This shows that between $x = 0.05$ and $x = 0.10$, the percolation threshold for the ZrV_2 phase is reached in the $V_{1-x}Zr_x$ alloys. Table 6.1 lists the values of the T_{sc} of these alloys.

6.1.3 Temperature dependence of magnetization of the $V_{1-x}Zr_x$ alloys

The $M(T)$ of the $V_{1-x}Zr_x$ (x = 0.05, 0.2, 0.33) alloys in the T range 2 - 9 K is shown in figures 6.7 (a) - (c). For all the alloys with $x > 0.05$, the $M(T)$ curves exhibit a two-step

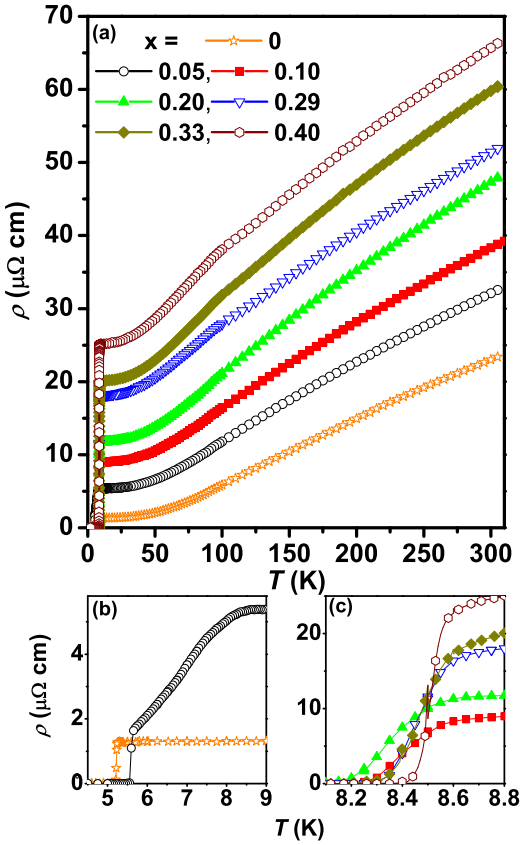

FIGURE 6.6: (a) Temperature dependence of electrical resistivity of the $V_{1-x}Zr_x$ alloys. Addition of Zr in V increases the residual resistivity due to the formation of secondary phases. (b, c) Expanded views of the temperature dependence of resistivity of the $V_{1-x}Zr_x$ alloys near the superconducting transition. For all the alloys with $x > 0.05$, the transition from the normal to superconducting state takes place below ~8.5 K indicating that these alloys have crossed the percolation threshold for the ZrV_2 phase.

transition process as the T is reduced below 9 K. These steps correspond to the magnetic flux expulsion at the onset of superconductivity in the ZrV_2 (T_{sc} = 8.5 K) and β-V (T_{sc} = 5.2 K) phases. From the M value during the ZFC cycle (measured in the presence of a magnetic field less than H_{c1}), we can estimate the superconducting volume fraction of the ZrV_2 and β-V phases. The superconducting volume fraction ($S_f(ZrV_2)$) of the ZrV_2 phase with respect to the β-V phase has been estimated as M(5.7 K)/M(2 K) and these values are presented in table 6.1. The S_f is less than 100 % for all the alloys, which shows that β-V is present in all the alloys up to x = 0.4. The insets to the figures 6.7 (a) - (c) show that the absolute value of

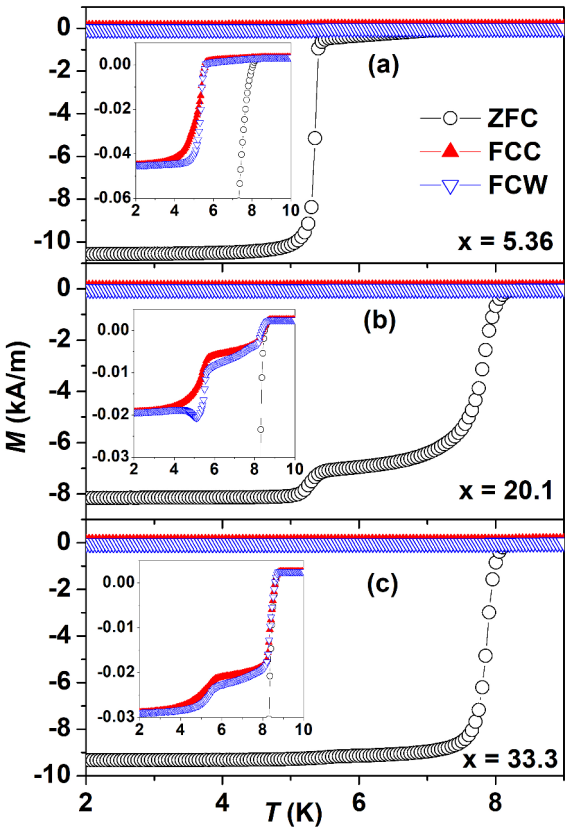

FIGURE 6.7: Temperature dependence of magnetization of the $V_{1-x}Zr_x$ (x = (a) 0.05, (b) 0.20 and (c) 0.33) alloys in the range 2-9 K measured in 10 mT magnetic field. All the samples above $x > 0.05$ exhibit a two-step transition when the temperature is decreased below 9 K. This is due to the superconductivity in the ZrV_2 (T_{sc} = 8.5 K) and β-V (T_{sc} = 5.2 K) phases. The insets show the expanded view of the FCC and FCW $M(T)$ curves.

magnetization in the FCC cycle is much smaller than that in the ZFC cycle. This indicates that the flux line pinning is strong in the $V_{1-x}Zr_x$ alloys.

6.1.4 Temperature dependence of resistivity and heat capacity of the $V_{1-x}Zr_x$ alloys in the presence of high magnetic fields

Figure 6.8 shows the $\rho(T)$ of the $x = 0.29$, 0.33 and 0.4 alloys measured in different magnetic field up to 16 T. Just below the $T_{sc}(H)$, the $\rho(T)$ drops to zero. The $T_{sc}(H)$ decreases with increasing H. However, with increasing Zr-content in V, the rate of decrease of $T_{sc}(H)$

TABLE 6.1: Residual resistivity, T_{sc} and the superconducting volume fraction S_f for various $V_{1-x}Zr_x$ alloys

x	ρ_0 ($\mu\Omega$ cm)	T_{sc} (K)	$S_f(ZrV_2)$ (%)
0	1.29 ± 0.06	5.22 ± 0.01	0
0.05	5.39 ± 0.11	5.60 ± 0.05	4.010 ± 0.002
0.10	8.99 ± 0.24	8.40 ± 0.05	88.79 ± 0.04
0.20	11.73 ± 0.17	8.30 ± 0.05	86.90 ± 0.05
0.29	18.11 ± 0.20	8.50 ± 0.05	95.96 ± 0.05
0.33	20.10 ± 0.08	8.50 ± 0.01	98.29 ± 0.07
0.40	25.10 ± 0.10	8.50 ± 0.01	98.78 ± 0.05

with respect to temperature decreases. For these alloys the superconducting transition is not complete even in the presence of 16 T magnetic field at 2 K. This shows that these alloys may be used for high field applications.

Figure 6.9 shows the $C(T)$ curves for the x = 0.29, 0.33 and 0.40 alloys plotted as C/T vs. T^2 in the temperature range 2 - 9 K in the presence of different magnetic fields. In the absence of applied magnetic field, the $C(T)$ of the x = 0.29, 0.33 and 0.40 alloys show three superconducting transitions [145]. The peak at about 5.2 K is due to the T_{sc} of the β-V phase. The large peak at about T^2 = 60 K^2 corresponds to the T_{sc} of the γ-ZrV_2 phase, whereas the change in curvature around T^2 = 70 K^2 corresponds to the T_{sc} of the γ'-ZrV_2 phase. The β-V phase become normal in the presence of high magnetic field and only two transitions corresponding to the γ'-ZrV_2 and γ-ZrV_2 phases are thus observed. The heat capacity measurements, however, confirm the bulk nature of superconductivity in these alloys. The $T_{sc}(H)$ values estimated from $C(T)$ are in agreement with that estimated from $\rho(T)$.

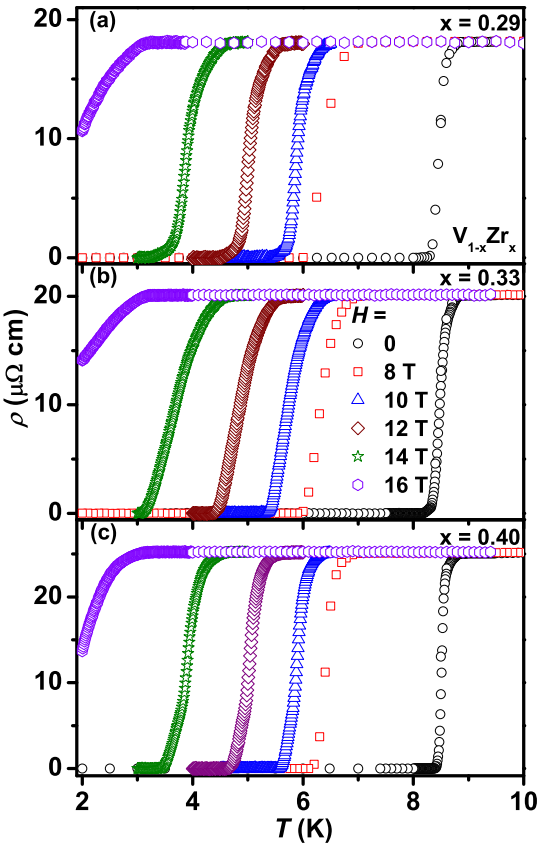

FIGURE 6.8: Temperature dependence of resistivity of the $V_{1-x}Zr_x$ alloys in the presence of different magnetic fields up to 16 T for (a) $x = 0.29$ (b) $x = 0.33$ and (c) $x = 0.40$. These alloys show well defined zero resistivity state below 4 K in the presence of 14 T magnetic field.

6.1.5 Field dependence of magnetization of the $V_{1-x}Zr_x$ alloys

The isothermal $M(H)$ of the $V_{0.60}Zr_{0.40}$ alloy up to 16 T is shown in figure 6.10. The hysteresis in $M(H)$ between the increasing and decreasing magnetic fields closes at H_{irr}. The H_{irr} is about 15 T at 2 K. The upper critical field (H_{c2}) of a superconductor is defined as the magnetic field at which a distinct deviation is observed from the magnetic field dependence of the normal state magnetization. This procedure has been effectively used to estimate the H_{c2} in the superconductors such as borocarbides [169, 170] and skutterudites [171]. The temperature dependence of H_{c2} and H_{irr} of the $V_{0.60}Zr_{0.40}$ alloy is shown in figure 6.10 (b). The error in the estimation of H_{c2} is less than 2 %. For all the alloys with $x > 0.05$, the

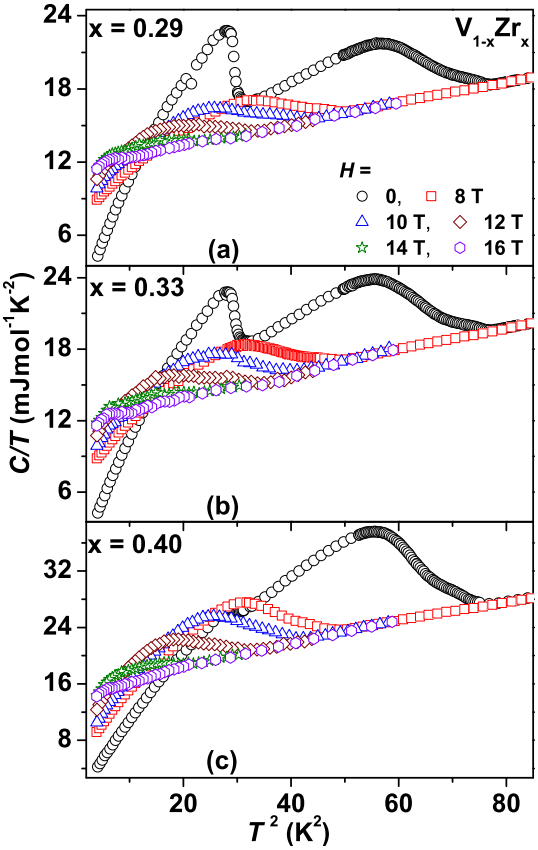

FIGURE 6.9: The heat capacity of the $V_{1-x}Zr_x$ alloys (x = 0.29, 0.33 and 0.40) plotted as C/T v/s T^2 in the temperature range 2-9 K in different applied magnetic fields up to 16 T. In zero field, three superconducting transitions are observed. In high magnetic fields, only two of these transitions are observed.

H_{c2} is of similar magnitude. The symbols correspond to the experimental data points. The estimated H_{c2} at 4.2 K is similar to the H_{c2} values reported from the $\rho(T)$ measurements [172]. The $H_{c2}(T)$ estimated from the temperature dependence of resistivity (△) and heat capacity (⋆) measurements are also plotted in figure 6.10 (b) for comparison. The $H-T$ line corresponding to the transition from superconducting state to normal state estimated from $M(H)$ is slightly lower as compared to that from $\rho(T)$ and $C(T)$. This is possibly due to the broadness of the transition width in $\rho(T)$ and $C(T)$, resulting from very close T_{sc} values corresponding to the γ'-ZrV_2 and γ-ZrV_2 phases. The lines are fit to the experimental data points using the Werthamer, Helfand and Hohenberg (WHH) model [173]. The dashed

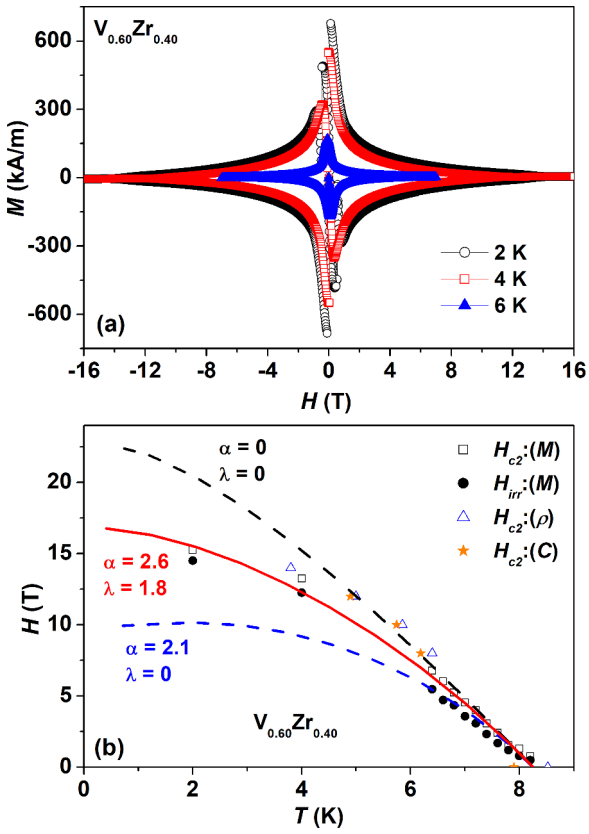

FIGURE 6.10: (a) Magnetic field dependence of magnetization of the $V_{0.60}Zr_{0.40}$ alloy at 2, 4 and 6 K. (b) The temperature dependence of H_{c2} and H_{irr} of the $V_{0.60}Zr_{0.40}$ alloy. The symbols represent the experimental data and the lines are the fits obtained using the WHH formalism. The H_{c2}(T = 0) is about 17.5 T.

line (black) represents the estimated $H_{c2}(T)$ without considering the paramagnetic effects and spin-orbit coupling. This line lie above the experimental data points at low T, which suggests that the paramagnetic effects are important in these alloys. The $H_{c2}(T)$ estimated by considering the paramagnetic effects alone ($\alpha = 2.1$) is shown by the blue dashed line. This line lies below the experimental data at low T, which indicates the presence of spin orbit coupling ($\lambda \neq 0$) in this alloy. The red solid line is the best fitted curve obtained considering the paramagnetic effects and spin orbit coupling with $\alpha = 2.1$ and $\lambda = 1.8$. The $H_{c2}(0)$ of the $x = 0.40$ alloy is 17.5 T. This indicates that this alloy is useful for high magnetic field applications.

6.1.6 Critical current density of the $V_{1-x}Zr_x$ alloys

Figure 6.11 shows the field dependence of J_c at (a) 4 K and (b) 2 K. For the alloys with $x < 0.29$, the J_c is estimated up to a magnetic field of 7 T, whereas for the alloys with $x \geq 0.29$ the J_c is estimated up to 16 T. The J_c increases with increasing Zr-content in V and is highest for the alloy with $x = 0.4$ for a given magnetic field. The $J_c(0)$ of the $x = 0.29$, 0.33 and 0.4 alloys are higher than 1000 A/mm^2 and decreases with increasing magnetic field. The $J_c(H)$ of the modern Nb-Ti wires (dashed line) [34, 35, 36, 37, 174] Nb_3Sn wires (dotted line) [37, 39, 40] along with (Hf,Zr)/V/Ta multifilamentary wire (curve 1: solid star) [175] and V-1at.% Hf/Zr-40 at.% Hf annealed 950 ^{0}C for 200 hr (curve 2: open star) [176] at 4.2 K are also shown in figure 6.11 for comparison. These J_c values reported from literature are estimated using transport measurements, whereas the J_c of the $V_{1-x}Zr_x$ alloys are estimated using the magnetization measurement. Thus, the comparison is needed to be considered with caution, although, the J_c estimated from the transport measurements are usually higher than that estimated from the magnetization measurements [141, 142]. It can be noted that the $J_c(H)$ (at $T = 4$ K and $H < 11$ T) of the $V_{0.60}Zr_{0.40}$ alloy is only about 5 times smaller than that of modern Nb-Ti wires. However, the $J_c(H)$ (at $T = 4$ K and $H < 11$ T) of the $V_{0.60}Zr_{0.40}$ alloy is comparable with the (Hf,Zr)/V/Ta multifilamentary wires prepared using RHQ technique (closed star) [175]. Moreover, even in fields above 11 T, the J_c in the $V_{0.60}Zr_{0.40}$ alloy are significant. These results indicate that the $V_{1-x}Zr_x$ alloys are promising candidates alternate to the Nb-based commercial superconductors for high magnetic field applications.

6.1.7 Flux pinning density of the $V_{1-x}Zr_x$ alloys

We have estimated the $F_P(H)$ for the $x = 0.29$, 0.33 and 0.4 alloys to understand the role of microstructure on the high $J_c(H)$ of these alloys. Figure 6.12 shows the normalized pinning force density $F_P/F_{P,m}$ as a function of reduced field $h = (H/H_{irr})$ at (a) $T = 4$ K and (b) $T = 2$ K respectively. Here, $F_{P,m}$ is the maximum F_P at a given temperature. For a given

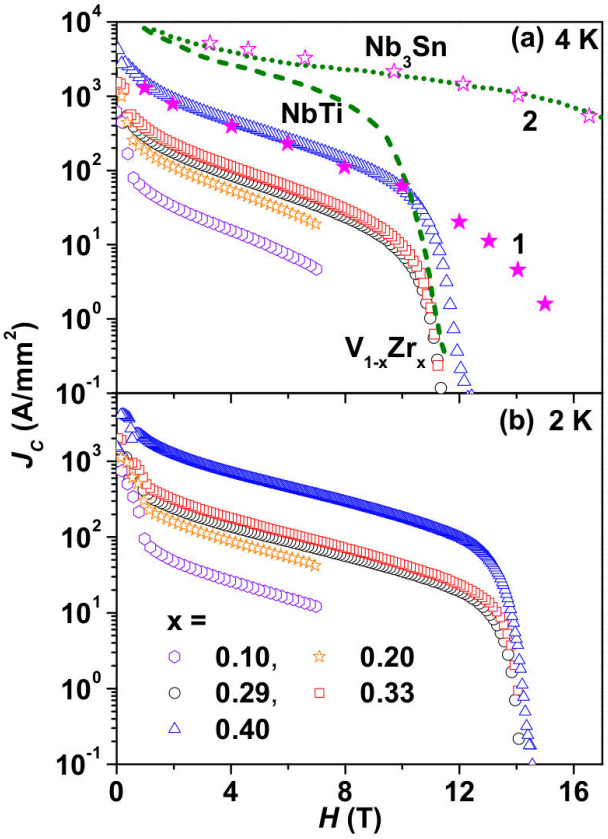

FIGURE 6.11: Magnetic field dependence of critical current density of the $V_{1-x}Zr_x$ alloys with x = 0.10, 0.20, 0.29, 0.33 and 0.40 at (a) 4 K and (b) 2 K. For comparison, we have plotted in (a) the J_c(H) of modern Nb-Ti wires (dashed line), Nb_3Sn wires (dotted line), (Hf,Zr)/V/Ta multifilamentary wire (curve 1: solid star) and V-1at.% Hf/Zr-40 at.% Hf annealed 950 ^{0}C for 200 hr (curve 2: open star) at 4.2 K.

temperature, the values of $F_P/F_{P,m}(h)$ is almost same for all the alloys. This indicates that similar type of pinning mechanisms are present in all these alloys. For both 4 K and 2 K, the $F_P/F_{P,m}$ is maximum around $h_m \sim 0.25$ and decreases slowly with increasing h. At 2 K, some of the alloys show a peak like structure at very low h. The $F_P(H)$ (at 2 K) of the $V_{1-x}Zr_x$ alloys with x = 0.29, 0.33 and 0.40 are shown as an inset to figure 6.12 (b). The F_P is maximum for the $V_{0.60}Zr_{0.40}$ alloy, which is about 3×10^9 Nm^{-3} for $H = 4.5$ T. The increase of F_P with increasing Zr content indicates the increase in the flux line pinning centres. The experimental maximum in the $F_P/F_{P,m}$ do not match with any of the fundamental forms prescribed by the Dew-Hughes model [31] for flux line pinning. A hump like feature

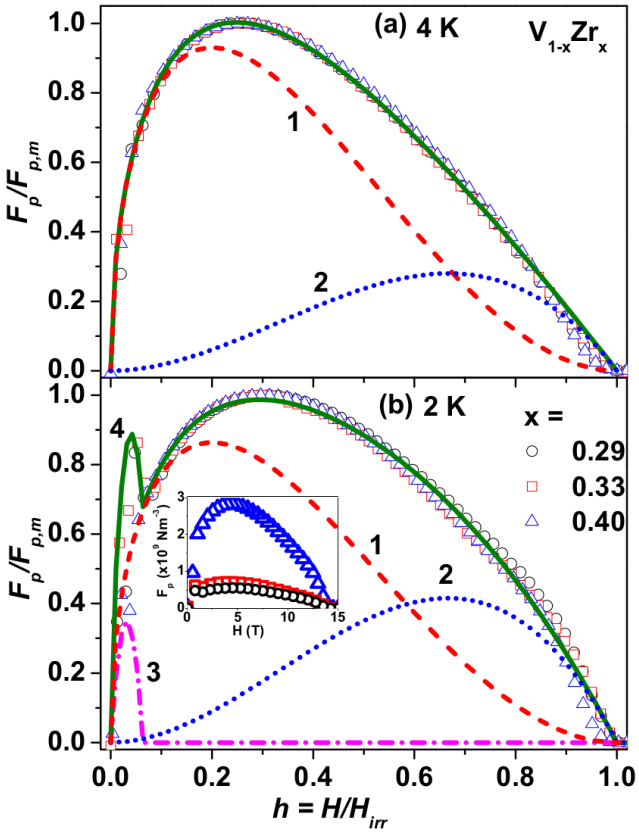

FIGURE 6.12: Normalized pinning force density of the $V_{1-x}Zr_x$ alloys as a function of h at (a) 4 K and (b) 2 K. It is observed that grain boundaries (curve 1) and point defects (curve 2) pin the flux lines in low and high magnetic fields respectively. (Inset) Magnetic field dependence of pinning force density at 2 K indicates that the pinning strength of the $x = 0.4$ alloy is more than 5 times higher than the other alloys.

is also observed at about $h = 0.8$. Thus, we infer the presence of more than one pinning mechanism in these alloys. In such a case, we can add the individual pinning force density for different pinning mechanism considering them to be independent of one another. This condition holds when different pinning mechanisms dominate at different magnetic fields [177, 178]. In such a case, F_P is given by,

$$F_P = F_{P1} + F_{P2} + F_{P3} + ... \tag{6.1}$$

Large amount of eutectic type microstructure is observed in the metallography images of these alloys with $x \geq 0.2$ (insets of figure 6.4 (c) and figure 6.5 (c)). Therefore, the GB density in these alloys are very high and we consider the GBs to be one of the major pinning centres for the flux lines in these alloys. This is also consistent with the fact that the maxima in $F_P/F_{P,m}$ is observed at $h = 0.25$. However, the $F_P/F_{P,m}$ does not drop for $h > h_m$ as expected for normal flux line pinning at the GBs and shows a change of slope at about $h \sim 0.8$. This indicates that the dominant pinning mechanism in high magnetic fields is different from that in low magnetic fields. The $\Delta\kappa_{GL}$ pinning from the point defects result in a maximum at $h = 0.67$. Thus, the flux line pinning in the high fields might be due to the point defects. Thus, equation 6.1 becomes,

$$F_P / F_{P,m} = Ah^{0.5}(1-h)^2 + Bh^2(1-h), \tag{6.2}$$

where A and B are the weight factors for the strength of pinning of flux lines respectively from the GBs and point defects. We observe that to account for the pinning properties over the complete H range, both the pinning mechanisms need to be considered. The major part of the experimental $F_P/F_{P,m}$ vs. h curve for these alloys can be reasonably fitted using equation 6.2. The ratio $A/B > 1$ indicates that the pinning at the GBs are much stronger than the $\Delta\kappa_{GL}$ pinning at the point defects, which is supported by our metallography images. The formation of the γ-ZrV_2 and β-Zr phases from the eutectic reaction below 1230 ^{o}C lead to smaller grains, thus increasing the number of GBs. However, we could not find any signature of the β-Zr phase in the EDS measurements, though the XRD patterns indicate their presence. This indicates that the β-Zr phase has precipitated with dimensions in nm scale, which is of the order of the coherence length. These β-Zr precipitates can work as point pinning centres. The area under the curves 1 and 2 in figure 6.12 are contribution to the normalized flux line pinning density from pinning at the grain boundaries and point defects respectively. With increasing T, the area under curve 1 increases and the area under curve 2 decreases. This shows that with increasing T, the flux line pinning at the GBs become more significant,

whereas that at the point defects become weak. The low field peak in $F_P/F_{P,m}(H)$ at T = 2 K cannot be explained using Dew-Hughes' theory unless a different $H_{irr} = 1.2$ T is taken to estimate h. The β-V phase has H_{c2} of about 1.2 T at 2 K. Therefore, we argue that this low field peak is from the pinning of flux lines in the β-V phase that has a T_{sc} = 5.2 K. This is also supported by the fact that this low field peak is almost absent in the $F_P/F_{P,m}(h)$ vs. h plot at 4 K. The flux line pinning due to the β-V phase follow the $\Delta\kappa_{GL}$ type volume pinning formula that has the functional form $F_{P3} = Ch(1-h)$.

6.2 Summary

We have studied the structural, electrical and magnetic properties of the arc melted as-cast $V_{1-x}Zr_x$ alloy superconductors. From the comparison of our metallography results with the existing equilibrium phase diagram, we conclude that when the molten $V_{1-x}Zr_x$ alloys are cooled rapidly,

(i) the V rich region solidifies below $\sim$ 1600 ^{o}C. This leads to the expulsion of excess Zr from the solid β-V phase and a Zr rich liquid forms along the GBs.

(ii) When the temperature is reduced below 1300 ^{o}C, the surface of β-V reacts with the Zr rich liquid (L1) to form a layer of γ' phase (peritectic reaction). The formation of γ phase further enriches the Zr content in the remaining liquid (L2).

(iii) Upon cooling below 1230 ^{o}C, the L2 liquid phase separate into γ and β-Zr phases (eutectic type reaction).

(iv) Below 777 ^{o}C, the β-Zr phase transforms into the α-Zr phase. However, depending on the cooling rate, there can be precipitation of untransformed β-Zr phase as well.

Our studies also show that the percolation threshold for bulk superconductivity due to the ZrV_2 phase in the $V_{1-x}Zr_x$ alloys is less than 10 at. % of Zr in V. The J_c of the $V_{1-x}Zr_x$ alloys with $x > 0.29$ is in the range of the modern Nb-Ti wires. The analysis of the microstructure and normalized flux line pinning force density suggest that the GBs generated due to the

eutectic type reaction pin the flux lines in the low magnetic fields and the point defects such as the β-precipitates pin the flux lines in the high magnetic fields. We found that the GBs are the strongest pinning centres and therefore, by driving the alloy to undergo a eutectic type reaction, we can increase the capacity of the material to carry large dissipationless current in this alloy system. Thus, the choice of the composition and the heat treatment that leads to the eutectic type reaction is important in improving the $J_c(H)$ in these alloys.

Chapter 7

Two channel heat conduction in the superconducting state of the as-cast $V_{1-x}Zr_x$ alloy superconductors

In the previous chapter, we have shown that some of the as-cast $V_{1-x}Zr_x$ alloys have a J_c comparable to the modern Nb-Ti superconductors [179]. Our analysis shows that the grain boundaries formed when the system undergoes eutectic reaction during cooling from the molten state are the major flux line pinning centres giving rise to the high J_c in these alloys. The high J_c of the multi-component $V_{1-x}Zr_x$ alloys make them potential candidates for use in high current high magnetic field applications. As the κ is another important physical property from the point of view of practical application of a superconductor, in this chapter we study the $C(T)$ and $\kappa(T)$ of the $V_{1-x}Zr_x$ alloys in the normal and superconducting states.

7.1 Results and discussion

7.1.1 Heat capacity of the $V_{1-x}Zr_x$ alloys

The $C(T)$ of the $V_{1-x}Zr_x$ alloys in the temperature range 2 - 10 K in the absence of applied magnetic field is shown in figure 7.1. We have shifted the $C(T)$ curves of different alloys vertically for better visibility. The $C(T)$ curve of the $x = 0$ alloy shows a distinct jump at

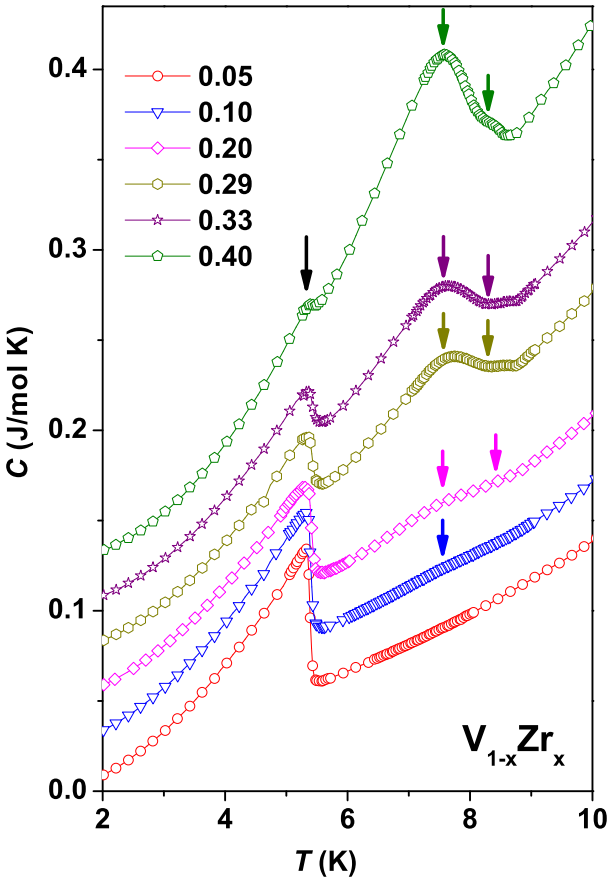

FIGURE 7.1: Temperature dependence of the heat capacity of the $V_{1-x}Zr_x$ alloys in zero field. The curves have been shifted vertically for better visibility. The superconducting transitions for different alloys are marked by arrows.

about 5.2 K, indicating the T_{sc} of V (T_{sc1}). The $C(T)$ curve for the $x = 0.05$ alloy shows a slight change of curvature just below 8.2 K apart from the jump at 5.2 K. For all the alloys with $x \geq 0.1$, three distinct features are observed (marked by arrows) in the $C(T)$ curves. A change of slope with a small hump is observed at about 8.5 K with a clear jump just below 8 K. The T_{sc} of the γ-ZrV_2 phase is in between 8 to 9 K [180, 181]. The small change in $C(T)$ at about 8.5 K indicates that this jump is from the onset of superconductivity in the $\gamma^{'}$-ZrV_2 phase. As the $\gamma^{'}$-ZrV_2 phase form around the GBs of the β-V phase, the volume fraction of this phase is small, which leads to the observation of the small hump. The prominent feature at about 8 K (which is prominent in the x = 0.29, 0.33 and 0.40 alloys), is due to the T_{sc} of

the major phase γ-ZrV_2 (T_{sc2}).

7.1.2 Thermal conductivity of the $V_{1-x}Zr_x$ alloys

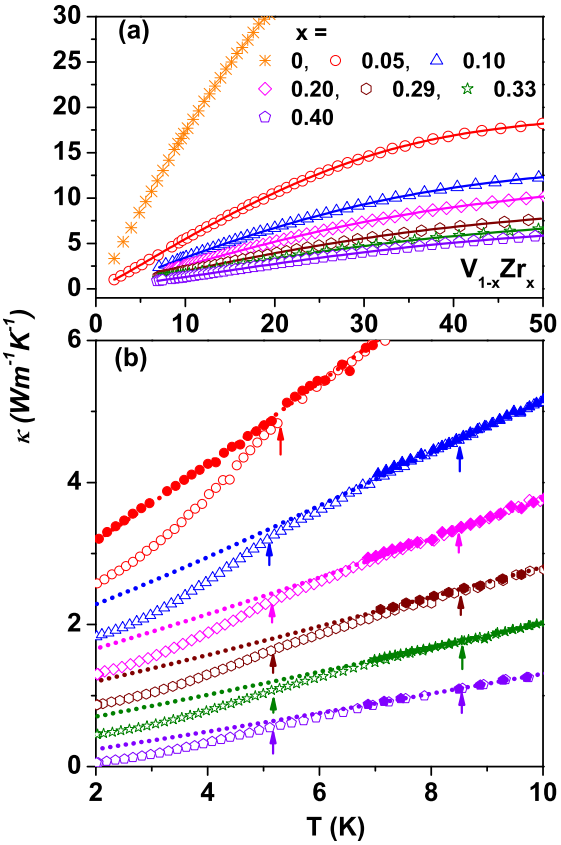

FIGURE 7.2: (a) Temperature dependence of thermal conductivity ($\kappa(T)$) of the $V_{1-x}Zr_x$ alloys in the normal state for the temperature range 6 - 50 K. The $\kappa(T)$ decreases with increasing Zr content. The open symbols are the experimental data and the solid lines are the fit to the same. (b) The $\kappa(T)$ of the $V_{1-x}Zr_x$ alloys below 10 K measured in zero (open symbols) and 8 T (closed symbols) magnetic fields. The dotted lines represent the normal state κ extrapolated in the range $T_{sc}(H = 8\ \text{T})$ to 2 K using the best fit parameters. The curves are shifted vertically and the superconducting transition temperatures are located with the help of arrows.

The (normal state) $\kappa_n(T)$ of the $V_{1-x}Zr_x$ alloys is shown in figure 7.2 (a). The $\kappa_n(T)$ for these alloys below T_{sc} = 8.5 K is obtained by applying an 8 T magnetic field. The alloys with $x \geq 0.10$ are superconducting below 6 K in the presence of an 8 T magnetic field [179]. Thus, by applying 8 T magnetic field the κ_n for the alloys with $x \geq 0.10$ could be obtained

only down to 6 K. At 10 K, the κ_n of V is about 15.4 W/m K, which reduces with increasing Zr content in V. The symbols correspond to the experimentally measured $\kappa(T)$ of these alloys. The $\kappa_n(T)$ of all the alloys show linear behaviour below 20 K. The metallography images shown in the figure 7.3 reveal the presence of a very large number of GBs in these alloys. Detailed metallography results are presented in chapter 6.

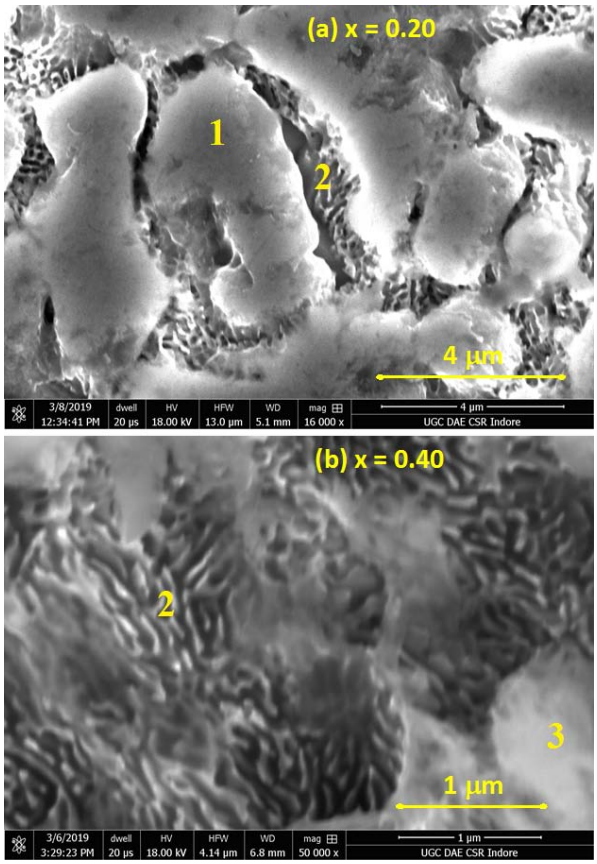

FIGURE 7.3: SEM micrographs of the $V_{1-x}Zr_x$ alloys for x = (a) 0.2 and (b) 0.4 alloys. The regions similar to that marked by "1" in (a) are the β-V phase and the regions similar to that marked by "3" in (b) are in γ'-ZrV_2 phase. Regions similar to the lamellar structure marked by "2" in both (a) and (b) contain γ'-ZrV_2 and α-Zr phases.

The $\kappa_n(T)$ is given as, $\kappa_n(T) = \kappa_{en}(T) + \kappa_{ln}(T)$, where $\kappa_{en}(T)$ and $\kappa_{ln}(T)$ are limited by different scattering mechanisms as discussed in chapter 1 (section 1.5). The analysis of F_P of these alloys also reveal that the GBs and point defects influence these properties strongly in the present alloys [179]. Therefore, we have considered the scattering of phonons from

electrons and dislocations to be insignificant in restricting the heat conduction by phonons, and we have taken the corresponding coefficients to be zero. On the other hand, in the presence of multiple structural phases, θ_D cannot be estimated reliably from the $C(T)$ curves. Hence, we have used the θ_D as a fitting parameter. As mentioned in the previous section, the $\kappa_n(T)$ of the $V_{1-x}Zr_x$ alloys show linear behaviour below 20 K. This indicates that similar to the $V_{1-x}Ti_x$ alloys, the scattering of electrons from the static defects limit the heat conduction below 20 K. Therefore, we have obtained the initial guess value of A_n with the help of WF law. We further obtained the initial guess values of B_n, N_n/M and P_n/M following trial and error method described in chapter 3. For θ_D, we used the θ_D of V as a initial parameter to fit the κ_n of the alloys containing Zr. The errors in the integration were optimized below 10^{-5} by varying the step sizes and the limits of the integration. Then, a least square error minimizing routine based on the Levenberg-Marquardt algorithm was used to fit the experimental data. The convergence criterion for the reduced chi-square was set to 10^{-4}. After obtaining the initial set of parameters from the fitting, the convergence was further checked by changing the initial guess values. Using equations 1.12, 1.13, 1.15 and 1.21 we have fitted the $\kappa_n(T)$ in the temperature range 6 - 50 K considering the scattering of electrons from defects and phonons as well as the scattering of phonons from GBs and point defects. The solid lines are fit to the $\kappa_n(T)$. The parameters obtained from fitting are listed in table 7.1. Electrons carry majority of the heat in the normal state and below 10 K, the phonons are ineffective in limiting the electronic heat flow (since $A_n \gg B_n$). Figure 7.2 (b) shows the $\kappa(T)$ of the $V_{1-x}Zr_x$ alloys in the T range 2 to 10 K. The empty symbols represent to the $\kappa(T)$ in the absence of applied magnetic field, and the filled symbols are those in the presence of 8 T magnetic field. The data for different alloys are shifted vertically for better visibility. The dotted lines correspond to the normal state thermal conductivity extrapolated using the fitting parameters presented in table 7.1. The T_{sc} is taken as the temperature where the $\kappa(T)$ start to deviate from $\kappa_n(T)$. The $\kappa(T, H = 0)$ curves start to decrease as the temperature is reduced below T_{sc3} = 8.5 K (corresponding to the γ'-ZrV_2 phase). This shows

that the electrons carry the majority of the heat in these alloys. The transitions at 8.2 K and 8.5 K are not visible as the change in $\kappa(T)$ is very small across T_{sc}.

TABLE 7.1: Parameters obtained from the fitting of $\kappa_n(T)$ and $\kappa_s(T)$. The variation in the values of the parameters satisfying the convergence criterion was within 2%.

x	A_n (m K^2 W^{-1})	B_n (m K^{-1} W^{-1})	θ_D (K)	N_n/M (m K^4 W^{-1})	P_n/M (m W^{-1})	c
0.05	2.09	5.99×10^{-6}	421	8.53×10^{3}	0.017	0.95
0.10	3.52	7.24×10^{-6}	430	1.15×10^{4}	0.017	0.9
0.20	4.39	8.14×10^{-6}	397	4.54×10^{4}	0.013	0.9
0.29	5.84	9.19×10^{-6}	415	3.99×10^{4}	0.024	0.85
0.33	6.87	11.32×10^{-6}	397	9.07×10^{4}	0.018	0.8
0.40	8.27	10.66×10^{-6}	428	1.88×10^{5}	0.011	0.8

$A_n \rightarrow$ electron-defect scattering coefficient; $B_n \rightarrow$ electron-phonon scattering coefficient; $\theta_D \rightarrow$ Debye temperature; $N_n/M \rightarrow$ phonon-grain boundary scattering coefficient; $P_n/M \rightarrow$ phonon-point defect scattering coefficient; $c \rightarrow$ weight factor for thermal resistivity of ZrV_2 phase.

We have used the Bardeen-Rickayzen-Tewordt (BRT) theory [63, 68, 69] to analyse the superconducting state thermal conductivity $\kappa_s(T)$ of these alloys. As the scattering of phonons from electrons does not affect the phononic heat conduction, this part remains the same in both the normal and superconducting states i.e. $\kappa_{ln} = \kappa_{ls}$. Therefore, $\kappa_s(T)$ is determined by the electronic thermal conductivity in the superconducting state (κ_{es}). The $\kappa_{es}(T)$ is estimated by subtracting the $\kappa_{ls}(T)$ form $\kappa_s(T)$ (see equation 1.22). Since the contribution of scattering of electrons from phonons to the electronic thermal resistivity is much lower in comparison with the scattering of electrons from the static defects, the κ_{es} is dictated by the superconducting state electronic thermal conductivity limited by electron-disorder scattering ($\kappa_{ei,s}(T)$). The procedure to estimate the $\kappa_{ei,s}(T)$ according to BRT theory has been described in detail in subsection 1.6 of chapter 1. Figure 7.4 shows the analysis of $\kappa_{es}(T)$

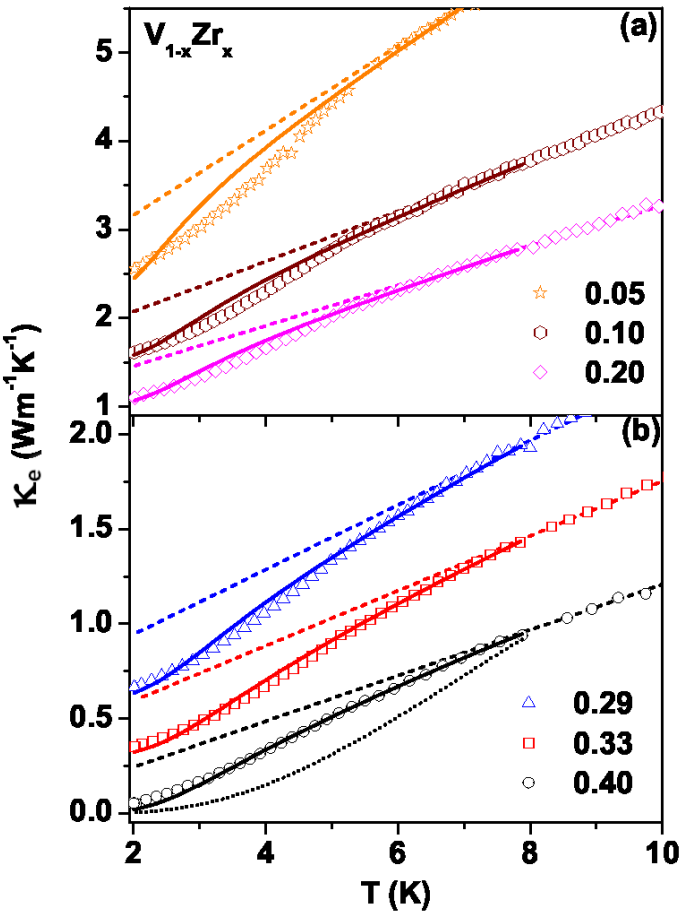

FIGURE 7.4: Analysis of the $\kappa_{es}(T)$ of the $V_{1-x}Zr_x$ alloys. The open symbols are the experimental data and the dashed line correspond to the normal state thermal conductivity. The dotted line in (b) is the $\kappa_{ei,s}$ obtained from BCS theory for the $x = 0.4$ alloy. The solid lines are the fit to experimental data obtained using a parallel conduction model.

of the $V_{1-x}Zr_x$ alloys. The open symbols are the experimental κ_{es} and the dashed lines are the κ_{en} estimated using the normal state fitting parameters. The $\kappa_{es}(T)$ of all the samples start to deviate from $\kappa_{en}(T)$ at 8.5 K, corresponding to the T_{sc3} of the $\gamma^{'}$-ZrV_2 phase. As the change in $\kappa(T)$ is very small just below T_{sc}, for the analysis of κ_{es} we assume that the T_{sc} of both $\gamma^{'}$-ZrV_2 and γ-ZrV_2 are same and equal to 8.5 K. With increasing x, the deviation of $\kappa_{es}(T)$ from $\kappa_{en}(T)$ below 8.5 K increases. The $\kappa_{ei,s}$ for the x = 0.40 alloy obtained using the BRT theory is shown by the dotted line in 7.4 (b). We have estimated the $\frac{\Delta_0}{k_B T_c}$ of the ZrV_2 phase using the heat capacity data of an annealed ZrV_2 sample, which has only γ and

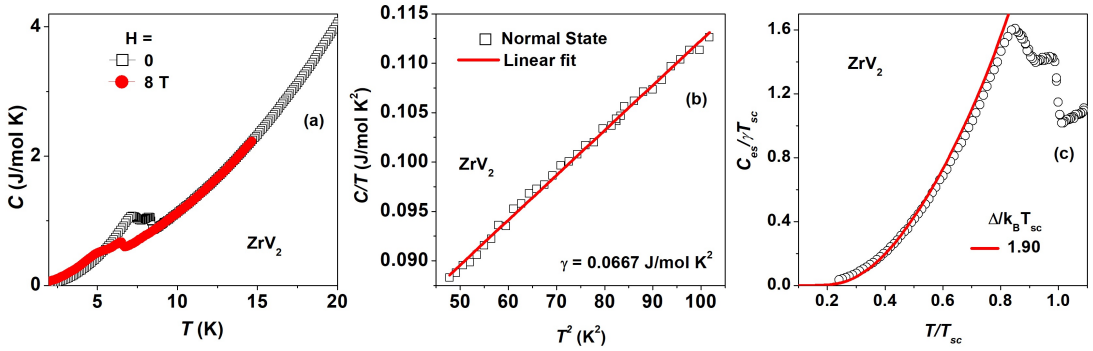

FIGURE 7.5: (a) Temperature dependence of heat capacity of ZrV_2. (b) Linear fit to the normal state heat capacity below 10 K. (c) Temperature dependence of the $C_{es}/\gamma T_{sc}$ as a function of the reduced temperature T/T_{sc}. The red line is fit to $C_{es}/\gamma T_{sc}$ for $\Delta/k_B T_{sc} = 1.90$.

$\gamma^{'}$ phases. The $C(T)$ of the annealed ZrV_2 sample is shown in figure 7.5 (a). Fit to the C_n/T $(= \gamma + \beta T^2)$ and $C_{es}/\gamma T_{sc}$ are shown in figure 7.5 (b) and (c) respectively. The value of $\frac{\Delta_0}{k_B T_c} = 1.90$ has been obtained for the annealed ZrV_2. We have used the $\frac{\Delta_0}{k_B T_c} = 1.90$ to estimate the $\kappa_{ei,s}$. For the $x = 0.40$ alloy, the $\kappa_{ei,s}$ obtained from the BRT theory is observed to be lower than the experimental value. This is true for other alloys as well. This suggests the presence of an additional heat conduction channel in these alloys. The α-Zr, β-V and β-Zr phases are not superconducting in the temperature range about 5 – 8.5 K. These phases account for this normal channel of heat conduction. The temperature dependence of $\kappa_{ei,s}$ in such a case can be expressed as,

$$\kappa_{es}^{-1} = (1-c)\kappa_{ei,s}^{-1} + c\kappa_{ei,n}^{-1}, \tag{7.1}$$

Therefore,

$$\kappa_{es} = \frac{\kappa_{ei,n} R_{ei}}{cR_{ei} + (1-c)}. \tag{7.2}$$

Here R_{ei} is the ratio κ_{es}/κ_{en} limited by the scattering of electrons from static defects (details are discussed in chapter 1) and c is the weight factor for the thermal resistivity in the normal state of the ZrV_2 phase. The solid lines in figure 7.4 are the fit to the experimental data using equation 7.1. The values of c obtained from the curve-fitting are listed in table 7.1.

The value of decrease from $c = 0.95$ for the $x = 0.05$ alloy to $c = 0.80$ for the $x = 0.40$ alloy. For temperatures close to T_{sc3}, majority of the electrons remain in the normal state, thus $\kappa_{es} \approx \kappa_{ei,n}$. Therefore, $cR_{ei} \gg (1-c)$ for $T \approx T_{sc} \approx T_{sc3}$. On the other hand, for temperatures $T \ll T_c = T_{c3}$, majority of the electrons condense to the ground state, which makes $\kappa_{es} \approx \kappa_{ei,s}$. Thus for $T \ll T_c = T_{c3}$, we get $cR_{ei} \ll (1-c)$ (as $R_{ei} \approx 0$). A significant deviation of the fitted curve from the experimental data below 5 K for the $x = 0.05$ and 0.10 alloys is observed. This is because of the fact that the volume fraction of the β-V phase is quite large (see figure 6.4 of subsection 6.1.1 for details) in these alloys, which makes the majority of heat in the superconducting state to be carried by the β-V phase. For the alloys with $x \geq 0.20$, the volume fraction of β-V phase is quite small (for details see figure 6.5 of subsection 6.1.1) and the fit using the parallel channel model is quite good over the measured temperature range.

7.2 Summary

We have studied the $C(T)$ and $\kappa(T)$ in the normal and superconducting states of the $V_{1-x}Zr_x$ alloys. Three distinct jumps in the $C(T)$ indicate the presence of three superconducting phases with transition temperatures $T_{sc1} = 5.2$ K for β-V, $T_{sc2} \sim 8.2$ K for γ-ZrV_2 and $T_{sc3} \sim 8.5$ K for γ'-ZrV_2 respectively. The $\kappa(T)$ of these alloys reduces with increasing Zr content in V. Electrons carry majority of the heat in the normal state of these alloys. The scattering of electrons from defects significantly limit the electronic heat conduction. In the superconducting state, the coexistence of multiple phases results in two parallel channels for the heat conduction. Our analysis also shows that more than 80% of heat in these alloys are carried by the normal channel. As a result, the thermal conductivity of the superconducting state is more than what is expected theoretically for a BCS-superconductor.

List of Symbols

g_n	Gibbs free energy in the normal state
g_s	Gibbs free energy in the superconducting state
ξ	Coherrence length
λ_L	Penetration depth
κ_{GL}	Ginzburg Landau parameter
T	Temperature
H	Magetic field (In te thesis we are using Tesla as the unit for H)
M	Magnetization
M_s	Spontaneous magnetization
J_c	Critical current density
F_P	Pinning force density
κ	Thermal conductivity
κ_e	Electronic thermal conductivity
κ_{en}	Electronic thermal conductivity in the normal state
κ_l	Phonon thermal conductivity
κ_{ln}	Phonon thermal conductivity in the normal state
κ_{es}	Electronic thermal conductivity in the superconducting state
κ_{ls}	Phonon thermal conductivity in the superconducting state
k_B	Boltzmann constant
θ_D	Debye temperature
C_n	Normal state heat capacity
C_{en}	Electronic heat capacity in the normal state

C_{ln}	Phononic heat capacity in the normal state
l_e	Electronic mean free path
l_l	Phononic mean free path
C_s	Superconducting state heat capacity
C_{es}	Electronic heat capacity in the superconducting state
C_{ls}	Phononic heat capacity in the superconducting state
T_{sc}	Superconducting transition temperature
ρ_0	Residual resistivity
a	Lattice constant
a_0	Bohr radius
d_a	Least inter atomic distance
Δ_0	Superconducting energy gap at zero temperature
γ	Sommerfeld coefficient of heat capacity
β	Coefficient of phononic heat capacity
ω	angular frequency

Bibliography

[1] http://www.nndc.bnl.gov/nudat2/.

[2] G. Audi, O. Bersillon, J. Blachot, and A.H. Wapstra, Nucl. Phys. A **729**, 3 (2003).

[3] T. G. Berlincourt and R. R. Hake, Phys. Rev. **131**, 140 (1963).

[4] E. W. Collings, "Applied Superconductivity, Metallurgy and Physics of Titanium Alliys," vol. 1, New York:Plenum Press (1986).

[5] M. Tai, K. Inoue, A. Kikuchi, T. Takeuchi, T. Kiyoshi, and Y. Hishinuma, IEEE Trans. Appl. Supercond. **17**, 2542 (2007).

[6] Md. Matin, L. S. Sharath Chandra, M. K. Chattopadhyay, R. K. Meena, Rakesh Kaul, M. N. Singh, A. K. Sinha, and S. B. Roy, J.Appl. Phys. **113**, 163903 (2013).

[7] Md. Matin, L. S. Sharath Chandra, M. K. Chattopadhyay, R. K. Meena, Rakesh Kaul, M. N. Singh, A. K. Sinha, and S. B. Roy, Physica C **512**, 32 (2015).

[8] K. Inoue, and K. Tachikawa, Appl. Phys. Lett. **29**, 386 (1976).

[9] K. Tachikawa, Cryogenics **19**, 307 (1979).

[10] M. Tenhover, IEEE Trans. Mag. **17**, 1021 (1981) and references therein.

[11] K. Inoue, H. Wada, T. Kuroda, and K. Tachikawa, Appl. Phys. Lett. **38**, 939 (1981) and references therein.

[12] T. P. Beales, J. Jutson, L. Le Lay, and M. Michele, J. Mater. Chem. **7**, 653 (1997).

[13] A. Imaduddin, H. Hendrik, S. Dwi Yudanto, H. Nugraha, P. Sebleku, and A. W. Pramono, J. Phys. Conf. Ser. **1091**, 012004 (2018).

[14] Y. Akyüz, A. Biçer, and M. Gürü, Mater. Des. **28**, 2500 (2007).

[15] Y. Ma et al., Phys. C Supercond. its Appl. **469**, 651 (2009).

[16] H. Huang et al., Supercond. Sci. Technol. **31**, 015017 (2018).

[17] L. R. Motowidlo, P. J. Lee, C. Tarantini, S. Balachandran, A. K. Ghosh, and D. C. Larbalestier, Supercond. Sci. Technol. **31**, 014002 (2018).

[18] J. L. H. Lindenhovius, E. M. Hornsveld, A. Den Ouden, W. A. J. Wessel, and H. H. J. Ten Kate, IEEE Trans. Appl. Supercond. **10**, 975 (2000).

[19] T. M. Tritt, ”Thermal Conductivity: Theory, Properties and Applications,” Kluwer Academic / Plenum Publishers, New York (2004).

[20] D. Van Delft and P. Kes, “The discovery of superconductivity,” Phys. Today **63**, 38 (2010).

[21] C. Kittel, ”Introduction to Solid State Physics,” 7th ed. Wiley-India (2009).

[22] W. Meissner and R. Ochsenfeld, “Ein neuer Effekt bei Eintritt der Supraleitfähigkeit,” Naturwissenschaften **21**, 787 (1933).

[23] F. London and H. London, Proc. R. Soc. London. Ser. A. Math. Phys. Sci. **149**, 71 (1935).

[24] V. V. Schmidt, ”The Physics of Superconductors,” Springer, Verlag Berlin Heidelberg (1997).

[25] M. Tinkham, ”Introduction to Superconductivity,” McGrar-Hill, New York (1996).

[26] V. L. Ginzburg and L. D. Landau, “On the Theory of Superconductivity,” Zh. Eksp. Teor. Fiz. **20**, 1064 (1950).

[27] A. C. Rose-Innes and E. H. Rhoderick, ”Introduction to Superconductivity,” Pergamon, Oxford, England (1994).

[28] T. Matsushita, ”Flux Pinning in Superconductors,” Springer-Verlag, Berlin Heidelberg (2007).

[29] C. P. Bean and J. D. Livingston, Phys. Rev. Lett. **12**, 14 (1964).

[30] C. P. Bean, Rev. Mod. Phys. **36**, 31 (1964).

[31] D. Dew-Hughes, Philos. Mag. **30**, 293 (1974).

[32] J. W. Ekin, Supercond. Sci. Technol. **23**, 083001 (2010).

[33] G. Enderlein, A. Handstein, F. Lange, and P. Verges, Cryogenics **13**, 426 (1973).

[34] O. V. Chernyj, G. F. Tikhinskij, G. E. Storozhilov, M. B. Lazareva, L. A. Kornienko, N. F. Andrlevskaya, V. V. Slezov, V. V. Sagalovich, Ya D. Starodubov, and S. I. Savchenko, Supercond. Sci. Technol. **4**, 318 (1991).

[35] T. Boutboul, S. Le Naour, D. Leroy, L. Oberli, and V. Previtali, IEEE Trans. Appl. Supercond. **16**, 1184 (2006).

[36] K. Miyashita, H. Sato, M. Arika, and R. Takahashi, Ele. Eng. Jpn **156**, 24 (2006).

[37] H. Lin, C. Yao, H. Zhang, X. Zhang, Q. Zhang, C. Dong, D. Wang, and Y. Ma, Sci. Rep. **5**, 11506 (2015).

[38] T. Mousavi, Z. Hong, A. Morrison, A. London, P. S. Grant, C. Grovenor and S. C. Speller, Supercond. Sci. Technol. **30**, 094001 (2017).

[39] K. Inoue, T. Kuroda, and K. Tachikawa, J. Nucl. Mat. **133** & **134**, 815 (1985).

[40] R. Flükiger, D. Uglietti, C. Senatore, and F. Buta, Cryogenics **48**, 293 (2008).

[41] B. Bordini, D. Richter, P. Alknes, A. Ballarino, L. Bottura, and L. Oberli, IEEE Trans. Appl. Supercond. **23**, 7100806 (2013).

[42] Y. Hishinuma, A. Kikuchi, Y. Iijima, Y. Yoshida, T. Takeuchi, A. Nishimura and K. Inoue, Supercond. Sci. Technol. **17**, 1031 (2004).

[43] C. Segal, C. Tarantini, Z. H. Sung, P. J. Lee, B. Sailer, M. Thoener, K. Schlenga, A. Ballarino, L. Bottura, B. Bordini, C. Scheuerlein, and D. C. Larbalestier, Supercond. Sci. Technol. **29**, 085003 (2016).

[44] B. Seeber, M. Decroux, and Fischer, Physica B Phys. Condens. Matter **155**, 129 (1989).

[45] S. Foner, IEEE Trans. Appl. Supercond. **5**, 121 (1995).

[46] G. R. Stewart, Physica C Supercond. its Appl. **514**, 28 (2015).

[47] T. Takeuchi, N. Banno, T. Fukuzaki, and H. Wada, Supercond. Sci. Technol. **13**, L11 (2000).

[48] Y. Yamada et al., Adv. Cryog. Eng. **40**, 907 (1994).

[49] N. Banno, D. Uglietti, B. Seeber, T. Takeuchi, and R. Flükiger, Supercond. Sci. Technol. **18**, S338 (2005).

[50] W. J. Lin et al., Mater. Lett. **198**, 176 (2017).

[51] N. Cheggour et al., J. Appl. Phys. **81**, 6277 (1997).

[52] D. N. Zheng, H. D. Ramsbottom, and D. P. Hampshire, Phys. Rev. B **52**, 931 (1995).

[53] C. Buzea and T. Yamashita, Supercond. Sci. Technol. **14**, R115 (2001).

[54] Y. Ma, A. Xu, X. Li, X. Zhang, S. Awaji, and K. Watanabe, Jpn. J. Appl. Phys. **45**, L493 (2006).

[55] G. Z. Li, Y. Yang, M. A. Susner, M. D. Sumption, and E. W. Collings, Supercond. Sci. Technol. **25**, 025001 (2012).

[56] C. Cui et al., Supercond. Sci. Technol. **2**, 59 (1989).

[57] J. Kumar, D. Sharma, P. K. Ahluwalia, and V. P. S. Awana, Mater. Chem. Phys. **139**, 681 (2013).

[58] Q. Li, K. Brodersen, H. A. Hjuler, and T. Freltoft, Physica C **217**, 360 (1993).

[59] J. Wu et al., Supercond. Sci. Technol. **32**, 125004 (2019).

[60] J. B. Vetrano, G. L. Guthrie, H. E. Kissinger, J. L. Brimhall, and B. Mastel, J. Appl. Phys. **39**, 2524 (1968).

[61] G. K. White, Proc. Phys. Soc. A **66**, 844 (1953).

[62] N. W. Ashcroft and N. D. Mermin, "Solid State Physics," Harcourt College Publishers, Orlando (1976).

[63] J. Bardeen, G. Rickayzen, and L. Tewordt, Phys. Rev. **113**, 982 (1959).

[64] J. Bardeen, L. N. Cooper, and J. R. Schrieffer, Phys. Rev. **108**, 1175 (1957).

[65] L. Tewordt, and T. Wölkhaushen, Solid State Commun. **70**, 839 (1989).

[66] L. Tewordt and T. Wolkhaushen, Solid State Commun. **75**, 515 1990.

[67] A. Carrington, and F. Manzano, Physica C **385**, 205 (2003).

[68] L. Tewordt, Phys. Rev. **127**, 371 (1961).

[69] L. Tewordt, Phys. Rev. **128**, 12 (1962).

[70] P. H. Kes, J. G. A. Rolfes, and D. de Klerk, J. Low Temp. Phys. **17**, 341 (1974).

[71] L. S. Sharath Chandra, M. K. Chattopadhyay, S. B. Roy, V. C. Saini, and G. R. Myneni, Supercond. Sci. Technol. **25**, 035010 (2012).

[72] W. D. Jung, F. A. Schmidt, and G. C. Danielson, Phys. Rev. B. **15**, 659 (1977) and references therein.

[73] C. L. Tsai, R. L. Fafaly, H. Weinstock, and F. A. Schmidt, Phys. Rev. B. **23**, 6430 (1981).

[74] N. Morton, B. W. James, G. H. Wostenholm, I. A. Taylor, and G. M. Taylor, Cryogenics **17**, 447 (1977) and references therein.

[75] E. I. Dyachkov, R. Herzog, I. S. khukhareva, and A. Nichitiu, Cryogenics **21**, 48 (1981).

[76] W. Li, H. Zhou, P. Lin, and S. Zhao, Mater. Charact. **60**, 1298 (2009).

[77] C.L. Wu, Y.G. Yan, Y.G. Chen, M.D. Tao, and X. Zheng, Int. J. Hydrogen Energy **33**, 93 (2008).

[78] Z. Zhang, G. Lin, S. Zhang, and J. Zhou, Mater. Sci. Eng. A **457**, 313 (2007).

[79] P. Dalvand, S. Raygan, G.A. López, M.B. Meléndez, and V.A. Chernenko, Mater. Sci. Eng. A **754**, 370 (2019).

[80] Y. Shao, M. Zhang, H. Luo, A. Yan, and J. Liu, Appl. Phys. Lett. **107**, 152403 (2015).

[81] B. D. Culity, ”Elements of X-Ray Diffraction,” Addision-Weasley, Reading, Massachusetts (1978).

[82] B. E. Warren, ”X-Ray Diffraction,” Dover publications, New York (1990).

[83] https://nanoimaging.umbc.edu/equipment/nova-nanosem-450-from-fei/.

[84] https://www.bruker.com/products/x-ray-diffraction-and-elemental-analysis/eds-wds-ebsd-sem-micro-xrf-and-sem-micro-ct/quantax-eds-for-sem/quantax-hardware/xflashr-6-30-detector.html.

[85] https://www.qdusa.com/products/mpms3.html.

[86] B. D. Cullity and C. D. Graham, "Introduction to magnetic materials," John Wiley & Sons, Hoboken, New Jersey (2009).

[87] Vibrating Sample Magnetometer (VSM) Option: User Manual, Quantum Design Inc. (2011), URL: https://www.mrl.ucsb.edu/sites/default/files/mrl_docs/instruments/VSM%20manual%20B0.pdf.

[88] Magnetic Property Measurement System, SQUID-VSM User Manual, Quantum Design USA (2009), URL: http://www.mrl.ucsb.edu/sites/default/files/mrl_docs/instruments/VSM%20manual%20B0.pdf.

[89] Heat Capacity Option User's Manual, Physical Properties Measurement System (PPMS, Quantum Design, USA) (2004), URL: http://www.mrl.ucsb.edu/sites/default/files/mrl_docs/instruments/hcapPPMS.pdf.

[90] Thermal Transport Option User's Manual, Physical Properties Measurement System (PPMS, Quantum Design, USA) (2002), URL: https://www.mrl.ucsb.edu/sites/default/files/mrl_docs/instruments/PPMSTTOmanualB0.pdf.

[91] PPMS Thermal-Transport Application Note, (PPMS, Quantum Design, USA), URL: https://qd-uki.co.uk/wp-content/uploads/2019/07/Thermal-Transport-Application-Note.pdf.

[92] O. Maldonado, Cryogenics **32:10**, 908 (1992).

[93] Ch. Leibovitch, A. Rabikin, and M.Talianker, Metallurgical Transactions A **12**, 1513 (1981).

[94] G. Aurelio, A. Fernấndez Guillermet, G. J. Cuello, and J. Campo, Metallurgical and Materials Transactions A **33**, 1307 (2002).

[95] Md. Matin, L. S. Sharath Chandra, Sudhir K. Pandey, M. K. Chattopadhyay, and S. B. Roy, Eur. Phys. J. B. **87**, 131 (2014).

[96] N. E. Hussey, K. Takenaka, and H. Takagi, Phil. Mag. **84**, 2847 (2004).

[97] M. Gurvitch, Phys. Rev. B **24**, 7404 (1981).

[98] A.F. Ioffe, *Proceedings of the International Conference on Electron Transport*, Ottawa (1956) (Can. J. Phys. **34**, 1393 (1956)).

[99] A. F. Ioffe, and A. R. Regal, Prog. Semicond. **4**, 237 (1960).

[100] Mark R. Graham, C. J. Adkins, Haim Behar, and Ralph Rosenbaum, J. Phys.: Condens Matter **10**, 809 (1998).

[101] N. F. Mott, "Metal-Insulator Transitions," Taylor and Francis, London (1990).

[102] S. R. Elliott, "Physics of Amorphous Materials," Longman Scientific and Technical, Harlow (1983).

[103] P. W. Anderson, Phys. Rev. **109**, 1492 (1958).

[104] E. Abrahmas, P. W. Anderson, D. C. Licciardello, and T. V. Ramakrishnan, Phys. Rev. Lett. **42**, 673 (1979).

[105] V. F. Gantmakher, JETP Lett. **94**, 626 (2011), V. F. Gantmakher, Pis'ma Zh. Eksp. Teor. Fiz **94**, 668 (2011), and references therein.

[106] V. F. Gantmakher, Low Temp. Phys. **39**, 2 (2013), V. F. Gantmakher, Fiz. Nizk. Temp. **39**, 5 (2013), and references therein.

[107] B. Sundqvist, Phys. Rev. Lett. **69**, 2975 (1992).

[108] J. J. Lin, C. Yu, and Y . D. Yao, Phys. Rev. B **48**, 4864 (1993).

[109] Z. Fisk, and G. Webb, Phys. Rev. Lett. **36**, 1084 (1976).

[110] H. Wiesmann, M. Gurvitch, H. Lutz, A. K. Ghosh, B. Schwartz, M. Strongin, P. B. Allen, and J. W. Halley, Phys. Rev. Lett. **38**, 782 (1977).

[111] R. Caton, and R. Viswanathan, Phys. Rev. B **25**, 179 (1982).

[112] M. Gurvitch, A. K. Ghosh, B. L. Gyorffy, H. Lutz, O. F. Kammerer, J. S. Rosner, and M. Strongin, Phys. Rev. Lett. **41**, 1616 (1978).

[113] J. H. Mooij, Phys. Status Solidi **17**, 521 (1973).

[114] K. Mori, N. Tamura, and Y. Saito, J. phys. Soc. Japan **50**, 1275 (1981).

[115] T. K. Nath, and A. K. Majumdar, Phys. Rev. B **53**, 12148 (1996).

[116] R.A. Richardson, S. D. Peacor, C. Uher, and F. Nori, J.Appl. Phys. **72**, 4788 (1992).

[117] W. S. Williams, Solid State Commun. **87**, 355 (1993).

[118] S. Cstellazzi, M. R. Cimberle, C. Ferdeghini, E. Giannini, G. Grasso, D. Marré, M. Putti, and A. Siri, Physica C **273**, 314 (1997).

[119] L. G. Radosevich, and W. S. Williams, Phys. Rev. **188**, 770 (1969).

[120] J. E. Graebner, B. Golding, R. J. Schutz, F. S. L. Hsu, and H. S. Chen, Phys. Rev. Lett. **39**, 1480 (1977).

[121] H. V. Löhneysen, M. Platte, W. Sander, H. J. Schink, G. V. Minnigerode, and R. Samwer, J. Phys. C: Colloq. **41**, 745 (1980).

[122] P. Esquinazi, and F. de la Cruz, Phys. Rev. B **27**, 3069 (1983).

[123] H. W. Gronert, D. M. Harlach, A. Schröder, R. van der berg, and H. V. Löhneysen, Z. Phys. B **63**, 173 (1986).

[124] H. V. Löhneysen, Mater. Sci. Eng. A **133**, 51 (1991).

[125] H. V. Löhneysen, D. M. Harlach, E. M. Wassermann, and K. Samwer, Solid State Commun. **39**, 591 (1981).

[126] B. Wuyts, V. V. Moshchalkov, and Y. Bruynseraede, Phys. Rev. B **53**, 9418 (1996).

[127] S. Sundar, L. S. Sharath Chandra, M. K. Chattopadhyay, and S. B. Roy, J. Phys. Condens. Matter. **27**, 045701 (2015).

[128] H. Padamsee, J. E. Neighbour, and C. A. Shiffman, J. Low Temp. Phys. **12**, 387 (1973).

[129] C. L. Huang, J-Y Lin, C. P. Sun, T. K. Lee, J. D. Kim, E. M. Choi, S. I. Lee, and H. D. Yang, Phys. Rev. B **73**, 012502 (2006).

[130] G. Seyfarth, J. P. Brison, G. Knebel, D. Aoki, G. Lapertot, and J. Flouquet Phys. Rev. Lett. **101**, 046401 (2008).

[131] Sabyasachi Paul. L. S. Sharath Chandra, and M. K. Chattopadhyay, J. Phys.: Condens. Matter **31**, 475801 (2019).

[132] R. Flükiger, C. Senatore, M. Cesaretti, F. Buta, D. Uglietti, and B. Seeber, Supercond. Sci. Technol. **21**, 054015 (2008).

[133] K. A. Gschneidner, Jr., "Structural and physical properties of alloys and intermetallic compounds," Progress in the science and technology of rare earths, vol. 1, Ed. L. Eyring, 222, Pergamon, New York (1964).

[134] A. M. Campbell, J. E. Evetts, and D. Dew-Hughes, Philos. Mag. **18**, 313 (1968).

[135] A. K. Sinha, A. Sagdeo, P. Gupta, A. Kumar, M. N. Sing, R. K. Gupta, S. R. Kane, and S. K. Deb, AIP Conf. Proc. **1349**, 503 (2011).

[136] S. Grazulis, D. Chateigner, R. T. Downs, A. T. Yokochi, M. Quiros, L. Lutterotti, E. Manakova, J. Butkus, P. Moeck, and A. Le Bail, J. Appl. Cryst. **42**, 726 (2009).

[137] S. Yu. Dan'kov, A. M. Tishin, V. K. Pecharsky, and K. A. Gschneidner, Jr., Phys. Rev. B **57**, 3478 (1998).

[138] R.M. Bozorth, D.D. Davis, and A.J. Williams, Phys. Rev. **119**, 1570 (1960).

[139] S. J. Singh, J Shimoyama, A. Yamamato, H. Ogino, and K. Kishio, Supercond. Sci. Technol. **26**, 065006 (2013) and references therein.

[140] A. Palenzona *et al.*, Supercond. Sci. Tech., **25**, 115018 (2012).

[141] D. Gajda, A. Zaleski, A. Morawski, and Md S. A. Hossain, Supercond. Sci. Technol. **30**, 085011 (2017).

[142] A. V. Pan, I. A. Golovchanskiy, and S. A. Fedoseev, Euro Phys. Lett. **103**, 17006 (2013).

[143] S.A. Keys, N. Koizumi, and D.P. Hampshire, Supercond. Sci. Technol. **15**, 991 (2002).

[144] S.A. Keys and D.P. Hampshire, Supercond. Sci. Technol. **16**, 1097 (2003).

[145] Sabyasachi Paul, SK. Ramjan, R. Venkatesh, L. S. Sharath Chandra, and M. K. Chattopadhyay, arxiv: 1912.04507 (2019).

[146] B. T. Matthias, H. Suhl, and E. Corenzwit, Phys. Rev. Lett. **1**, 92 (1958).

[147] C. T. Wolowiec, B. D. White, and M. B. Maple, Physica C: Supercond. **514**, 113 (2015) and the references therein.

[148] K. Schwidtal, Z. Phys. **158**, 563 (1960).

[149] M. A. Woolf, and F. Reif, Phys. Rev. **137A**, 557 (1965).

[150] B. T. Matthias, H. Suhl, and E. Corenzwit, Phys. Rev. Lett. **1**, 449 (1958).

[151] M. B. Maple, Phys. Lett. **26A**, 513 (1968).

[152] S. Yu. Dan'kov, A. M. Tishin, V. K. Pecharsky, and K. A. Gschneidner, Jr., Phys. Rev. B **57**, 3478 (1998).

[153] A. Arrott, and J. E. Noakes, Phys. Rev. Lett. **19**, 786 (1967).

[154] J. H. Hankiewicz, Z. Celinski, K. F. Stupic, N.R. Anderson, and R. E. Camley, Nat. Commun. **7**:12415 (2016).

[155] Md. Matin, L. S. Sharath Chandra, R. Meena, M. K. Chattopadhyay, A. K. Sinha, M. N. Singh, and S. B. Roy, Physica B **436**, 20 (2014).

[156] N. A. de Oliveira, A. A. Gomes, and A. Troper, Hyperfine Interact. **80**, 1067 (1993).

[157] P. Lucaci, E. Burzo, and I. Lupsa, J. Alloys Compd. **238**, L4 (1996).

[158] E. Burzo, and P. Lucaci, Solid State Commun. **79**, 1077 (1991).

[159] L. Dubeck, P. Lindenfeld, E. A. Lynton, and H. Rohrer, Phys. Rev. Lett. **10**, 98 (1963).

[160] L. Dubeck, P. Lindenfeld, E. A. Lynton, and H. Rohrer, Rev. Mod. Phys. **36**, 110 (1964).

[161] J. T. Williams, Retrospective Theses and Dissertations. Paper 13305 (*The vanadium-zirconium alloy system*, Iowa state collage) pp.1-73 (1954).

[162] X. -S. Zhao, G. -H. Yuan, M. -Y. Yao, Q. Yue, and J. -Y. Shen, Calphad **36**, 163 (2012) and the references therein.

[163] J. Strot, J. Pavlu, U. D. Wdowik, J. Bursik, M. Sob, and J. Vrestal, CALPHAD **44**, 62 (2014).

[164] J. Cui, C. Guo, L. Zou, C. Li, and Z. Du, Calphad **53**, 122 (2016) and the references therein.

[165] https://www.iucr.org/resources/other-directories/software/powder-cell

[166] W. Kraus, and G. Nolze, J. Appl. Cryst. **29**, 301 (1996).

[167] A. R. Bailey, ”Introductory Practical Metallography.” Metallurgical Services Laboratories Ltd., Surrey, England (1974).

[168] C. Servant, J. Phase Equilib. Diff. **26**, 39 (2005).

[169] S. B. Roy, Z. Hossain, A. K. Pradhan, C. Mazumdar, P. Chaddah, R. Nagarajan, C. Godart and L. C. Gupta, Physica C **228**, 319 (1994) and the references therein.

[170] S. B. Roy, Z. Hossain, A. K. Pradhan, P. Chaddah, R. Nagarajan, and L. C. Gupta, Physica C **256**, 90 (1996) and the references therein.

[171] L. S. Sharath Chandra, M. K. Chattopadhyay and S. B. Roy, Phil. Mag. **92**, 3866 (2012).

[172] K. Yasohama, and N. Usui, Jpn. J. Appl. Phys. **7**, 1128 (1968).

[173] N. R. Werthamer, E. Helfand and P. C. Hohenberg, Phys. Rev. **147**, 295 (1966).

[174] G. Enderlein, A. Handstein, F. Lange, and P. Verges, Cryogenics **13**, 426 (1973).

[175] Y. Hishinuma, A. Kikuchi, Y. Iijima, Y. Yoshida, T. Takeuchi, K. Inoue, and A. Nishimura, IEEE Trans. Appl. Supercond. **16**, 1196 (2006).

[176] K. Inoue, T. Kuroda, and K. Tachikawa, IEEE Trans. Mag. **15**, 635 (1979).

[177] P. J. Li, Z. H. Wang, A. M. Hu, Z. Bai, L. Qiu, and J Gao, Supercond. Sci. Technol. **19**, 825 (2006).

[178] L. Muzzi, G. De Marzi, C. F. Zignani, U. B. Vetrella, V. Corato, A. Rufoloni, and A. della Corte, IEEE Trans. Appl. Supercond. **21**, 3132 (2011).

[179] L. S. S. Chandra, Sabyasachi Paul, Ashish Khandelwal, Vinay Kaushik, Archna Sagdeo, R. Venktesh, Kranti Kumar, A. Banerjee, and M. K. Chattopadhyay, J. Appl. Phys. **126**, 183905 (2019).

[180] S. B. Roy, Phil. Mag. B **65**, 1435 (1992).

[181] Wataru Takahara, Hiroshi Maeda, and Fumiyoshi Minami, Adv. in Quantum Chemistry **42**, 275 (2003).

[182] Yu. F. Bychkov, R. Herzog, and I. S. khukhareva, Cryogenics **21**, 741 (1981).

[183] P. Zhang, J. Li, Q. Guo, Y. Zhu, K. Yan, R. Wang, K. Zhang, X. Liu, and Y. Feng, ”NbTi Superconducting wires and applications,” Titanium alloys for consumer applications, Ed. F. Froes, M. Qian and M. Niinomi, 279, Elsevier, Amsterdam (2019).

[184] W-Y. Kim, D. E. Luzzi, and D. P. Pope, Intermetallics **11**, 257 (2003).

[185] K. Inoue, and K. Tachikawa, IEEE Trans. Mag. **13**, 840 (1977).

Thesis Highlight

Name of the Student: Sabyasachi Paul

Name of the CI/OCC: Raja Ramanna Centre for Advanced Technology

Enrolment No.: PHYS03201504009

Thesis Title: Thermal conductivity and critical current density of Vanadium based alloy superconductors

Discipline: Physical Sciences **Sub-Area of Discipline:** Material Science

Date of viva voce: 28/06/2021

The demand of superconducting magnets for various applications are increasing everyday and with growing demand there is an urgent need to look for materials alternate to Nb-based superconductors. Two important properties one need to consider for practical applications of superconductors are the thermal conductivity κ and the critical current density J_c.

This thesis presents the studies on the κ and J_c of V-based alloys superconductors. The superconducting state thermal conductivity κ_s of the $V_{1-x}Ti_x$ alloys increases with decreasing temperature. This indicates that phonons carry majority of the heat in the superconducting state of these alloys, whereas electrons carry majority of the heat in the normal state. This contrasting behavior is related to the facts that the electronic mean free path is of the order of the interatomic distances in these alloys, and the grain size is very large. The addition of 1 at.% Gd in $V_{0.60}Ti_{0.40}$ alloy resulted in the enhancement of the J_c by more than 20 times at 4 K up to the irreversibility field H_{irr} due to the grain refinement resulting from the precipitation of the Gd along the grain boundaries. This method provides an easy way to enhance the J_c of a superconductor without requiring any complicated thermo-mechanical treatment. While the addition of Gd in $V_{0.60}Ti_{0.40}$ alloy suppressed the phonon thermal conductivity up to 80%, the electronic thermal conductivity reduces only up to 15%. This lead to crossover from phonon dominated heat conduction to electron dominated heat conduction in the superconducting state in 8 T magnetic field. Another important finding is that superconductivity in the Gd-added alloys persists even in the presence of the ferromagnetic ordering and in fact the superconducting transition temperature increases slightly in the alloys containing Gd. The very high J_c of the $V_{1-x}Zr_x$ alloys were observed to be de to the presence of huge number of grain boundaries generated during the eutectic reaction. Moreover, the presence of different metallurgical phases that remain normal down to 2 K led to the formation of normal channel of heat conduction in the $V_{1-x}Zr_x$ alloys when bulk of the sample remain superconducting. In summary, this thesis provides insights into both the scientific and technological aspects of the V-based alloy superconductors.

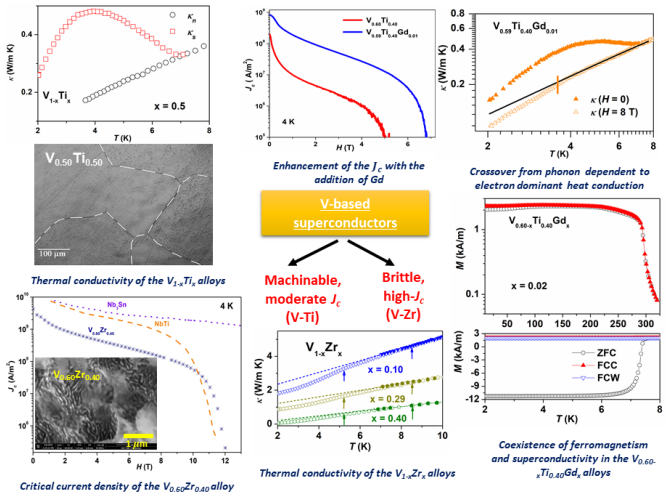

Figure 1. Important results arising from the thesis. Both the κ and J_c are heavily influenced by the defects present in the system.